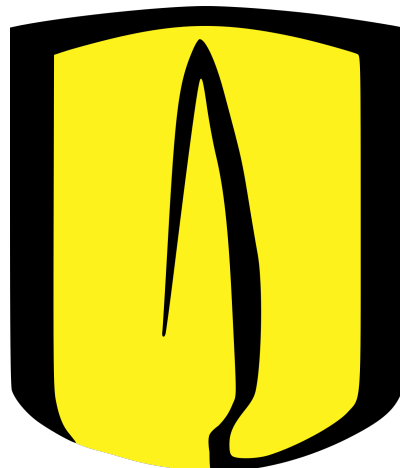


Spectroscopic differentiation of stars within the Red Clump

Author: Eric Fabrizio Fuentes Rico

Supervisor: Benjamin Oostra Vannoppen

*A dissertation submitted in partial fulfillment of the requirements for the degree of
Bachelor of Science in Physics*



Department of Physics
Faculty of Sciences
Universidad de los Andes

Bogotá D.C., Colombia
August 13, 2022

Abstract

Although Red Clump (RC) stars have been increasingly used as standard candles to measure stellar extinctions, distances, chemistry and kinematics both in and out of the Milky Way due to the small variation within their properties, this ever growing interest and appreciation in RC methods seems to not have been followed by the development of easier ways to quickly identify RC stars, for the RC and a part of the Red Giant Branch (RGB) are superimposed in the Hertzsprung-Russell (HR) diagram and the only way to differentiate them has so far been by resorting to complicated chemical and asteroseismological methods. After APOKASC —a project devoted to asteroseismology— revealed an offset between the surface gravities determined with spectroscopy and those determined with asteroseismology, the idea that there could exist a missing spectroscopic variable that allows to distinguish between RC and RGB stars by spectroscopic methods alone soon came out and recent studies have found that such variable could be related to the CN-cycle of stars, being the CN I absorption spectral lines stronger in RC stars than in similar RGB stars. In this dissertation, that line of work is resumed by measuring the equivalent width (EW) of 9 absorption spectral lines (4 Fe I, 1 Ti I and 4 CN I lines) within the wavelength range [7400 Å, 7500 Å] for a sample of 31 stars within the RC's neighborhood in the HR diagram. Although the sample of stars used was too small to really "prove" something, no counterexample to the hypothesis could be found; at least at first glance, the results seem to indicate that the limit $\frac{\overline{EW}_{Ti}}{\overline{EW}_{CN}} = 2.5$ is of great significance since all RGB stars but one fell above it and all RC stars fell below it, forming a remarkably small clump on the (Absolute visual magnitude, $\frac{\overline{EW}_{Ti}}{\overline{EW}_{CN}}$) plane. Furthermore, it was found that adding the $\frac{\overline{EW}_{Ti}}{\overline{EW}_{CN}}$ dimension to the classical 2D HR diagram results in a "3D HR space" that seems to be able to differentiate the 2 evolutionary stages (RC and RGB) as distinct 3D clumps and also suggests that some of the stars whose evolutionary status could not be found in literature are actually carbon stars traveling up the Asymptotic Giant Branch (AGB), for they also manifest as a distinct 3D clump. In any case, however, the fact that the strength of the lines of the CN I molecule seems to be able to differentiate RC and RGB stars reveals a puzzling difference between their photosphere's C-content that does not find any explanation within classical low-mass stellar evolution theory. This phenomenon could be caused by some still-to-be-explained non-canonical convection mechanism related to the helium flash, but far more evidence is required to assert this with strong conviction.

Dedication and acknowledgements

Before anything else, I would like to express my enormous gratitude to my advisor, Benjamin Oostra Vannoppen, for all his accurate recommendations and dedication during this last year of hard work, as well as for all the support and immense patience he had while I was at my worst during and after the COVID-19 pandemic. Without all his knowledge, guidance, challenges and contributions, this dissertation would have been an impossible feat.

Additionally, I would like to recognize my parents and my grandmother for all the assistance they gave me in order to make my stay at Bogotá and at the Universidad de los Andes possible and enjoyable, even when they did not understand some of the life decisions I made.

And last but not least, I would also like to thank Juan Salamanca, Diego Melo, Samir de la Cruz and Paula Vargas for their tireless friendship and company throughout these last four years, things without which I would have never made it this far in my academic and personal development.

"Not how the world is, but that it is, is the mystery."

—Ludwig Wittgenstein


 Contents

1	Introduction	1
2	Theoretical framework	4
2.1	Mapping the sky: the Hipparcos mission	4
2.2	Calculating the distance to a star: the stellar parallax	4
2.3	Measuring the energy radiated by a star	6
2.3.1	The apparent magnitude (m)	6
2.3.2	Flux, luminosity and the inverse square law	6
2.3.3	The absolute magnitude	6
2.4	The color and temperature of a star	7
2.4.1	The connection between color and temperature	7
2.4.2	The color index	9
2.5	Dissecting the light of a star: the spectral lines	9
2.5.1	The strength of a spectral line: the Equivalent Width (EW)	11
2.5.2	How spectral lines are broadened	12
2.5.3	A way to calculate abundances	13
2.6	Stellar classification: the different kinds of stars	13
2.7	Stellar evolution: the life cycle of a star	14
2.7.1	Main Sequence (MS) evolution	15
2.7.2	The Subgiant Branch (SGB)	18
2.7.3	The Red Giant Branch (RGB)	18
2.7.4	The Helium Core Flash	18
2.7.5	The Horizontal Branch (HB)	19
2.7.6	The Early Asymptotic Giant Branch (E-AGB)	20
2.7.7	The Thermal-Pulse Asymptotic Giant Branch (TP-AGB)	20
2.7.8	The Post-Asymptotic Giant Branch (Post-AGB)	21
2.7.9	Planetary nebulae	21
2.8	The Red Clump	21
2.8.1	Characteristics and origin of the RC	22
2.8.2	The RC in the HR diagram	24
2.8.3	Why the Red Clump?	24
2.9	Previous works on the subject	25
3	Observational data	27
3.1	Selecting RC stars from Hipparcos' catalogue	27
3.1.1	Choosing the star catalogue	27

3.1.2	First reduction of data: the negative parallax filter	27
3.1.3	Second reduction of data: the B-V color index filter	28
3.1.4	Third reduction of data: the average partition error filter	28
3.1.5	Forth reduction of data: the absolute visual magnitude filter	29
3.1.6	Limiting the wavelength range and looking for the spectra	30
3.2	Picking stars directly from UVES-POP	30
3.3	Visualizing PEPSI's stars	33
4	Normalizing the spectra	35
4.1	Plotting the original spectrum	35
4.2	Calculating the maximizing function	35
4.3	Averaging the maximized flux values	35
4.4	Obtaining the normalized spectrum	36
4.5	Getting the inversed normalized spectrum	37
5	Selection of spectral lines	39
5.1	Looking for the spectral lines in a model star's spectrum	39
5.2	Selected Ti I lines	39
5.3	Selected Fe I lines	40
5.4	Selected CN I lines	41
5.5	Visualization of the studied lines in the spectra	43
6	Measuring the strength of the spectral lines	45
6.1	Modeling the spectral lines	45
6.1.1	Computing the wavelength shift $\Delta\lambda$	46
6.1.2	Isolating the desired spectral line	46
6.1.3	Parabolic regression	47
6.1.4	Obtaining the isolated spectral line's gaussian profile	48
6.2	Calculating the EWs (direct method)	48
6.3	Calculating the EWs (visual method)	50
7	Results and discussion	54
7.1	The Equivalent Widths	54
7.2	Quotients of Equivalent Widths	54
7.3	Relation with other stellar parameters	63
7.3.1	Metallicity [Fe/H]	63
7.3.2	Surface gravity $\log(g)$	66
7.3.3	Mass	68
7.4	3D analysis	70
8	Conclusion	75

9 Future work	76
A How to calculate the uncertainties	82
A.1 The distance to the star (D)	82
A.2 The absolute visual magnitude (M_V)	82
A.3 The partition error	83
A.4 The Equivalent Width (EW)	83
A.5 The average EW (\bar{EW})	83
A.6 The quotients of EWs $\left(\frac{\bar{EW}_x}{\bar{EW}_y}\right)$	85
B About the stars used in this work	87
B.1 Classification and basic quantities	87
B.2 Additional quantities	88

List of Figures and Tables

1	Hertzsprung-Russell diagram with 22000 stars taken from Hipparcos' catalogue and 1000 stars taken from Gliese's catalogue. Taken from [6].	2
2	Stellar evolution of a star of $1M_{\odot}$. After leaving the Main Sequence (MS), the star passes to the subgiant branch (SGB) and then to the Red Giant Branch (RGB). Subsequently, it spends time in the Red Clump (RC) and in the Horizontal Branch (HB) and ends up in the Asymptotic Giant Branch (AGB), phase at which it begins to lose mass until it dies, leaving a white dwarf and a planetary nebula behind. Image taken from [8].	3
3	The Hipparcos satellite being tested under the Large Solar Simulator prior to the start of the mission in 1989. Image taken from [9].	5
4	Illustrative diagram for how the stellar parallax is calculated. The blue circle is the Earth, which orbits the Sun —the yellow circle— with an orbital radius of 1 astronomical unit (AU). Image taken from [10].	5
5	Blackbody spectrum (Planck function $B_{\lambda(T)}$). Image taken from [11].	8
6	Typical effective surface temperatures and color indexes for different classes of stars. Image taken from [13].	10
7	Diagram of a prism spectroscope. The light emitted from the vapor lamp is parallelized with a collimator and then passed through a prism in which it is refracted twice (once when entering and once when leaving). Since the angle with which light is refracted depends on its wavelength, this leads to a spectrum of thin lines of light, each observable at a different angle, which can be used to compute the wavelength. Image taken from [11].	11
8	Geometrical definition of the Equivalent Width (EW) of a spectral line. Image taken from [11].	12
9	Curve of growth for the K line of Ca II. As N_a increases, the functional dependence of the equivalent width (W) changes. Image taken from [11].	14
10	Main characteristics of the MK system's spectral types. Image taken from [11].	15
11	Digitized spectra of Main Sequence classes O5-K5 displayed in terms of relative flux as a function of wavelength. Figures taken and adapted from [11].	16
12	Dependence of spectral line strengths on temperature. Image taken from [11].	16

13	Evolutionary tracks for stars with different initial compositions. The more massive the star, the less time it takes it to complete its evolutionary track. Image taken from [13].	17
14	A schematic diagram of the evolution of a low-mass star of $1 M_{\odot}$ from its birth in the MS to the formation of a white dwarf. The dotted phase represents the rapid evolution following the helium core flash. Image taken from [11].	19
15	A schematic diagram of the evolution of an intermediate-mass star of $5 M_{\odot}$ from its birth in the MS to the formation of a white dwarf. Image taken from [11].	20
16	Some crucial parameters at the beginning of the core helium-burning (CHeB) lifetime as a function of mass and metallicity, for the entire mass interval relevant for the definition of the Red Clump. Panels show (a) the H-exhausted core mass M_{core} , (b) the total stellar luminosity, (c) the ratio between the luminosities of the H-burning shell and the He-burning core and (d) the total CHeB lifetimes, τ_{He} . Image taken from [14].	23
17	The Solar Neighborhood's RC revealed by Hipparcos in a few color-magnitude diagrams. Only stars with parallax errors $\frac{\sigma_{\pi}}{\pi}$ smaller than 10% are plotted. Image taken from [14].	24
18	Difference between the $\log(g)$ derived from APOGEE DR13 and the $\log(g)$ obtained by asteroseismology as a function of stellar mass. Image taken from [5].	25
19	Logarithmic relationship between the number of stars and their parallaxes. An apparent break of the relationship appears at $plx = 10$ m.a.s.	28
20	Average partition error for the distances associated with different parallax ranges. It can be appreciated how parallaxes of less than 10 m.a.s lead to very inaccurate results.	29
21	Unnormalized absorption spectrum of RC star Unukalhai.	30
22	Unnormalized absorption spectrum of RC star Kaus Borealis.	31
23	HR diagram showing the origin of the spectra of the studied stars.	31
24	Unnormalized absorption spectrum of RGB star Arcturus.	32
25	Unnormalized absorption spectrum of RGB star Aldebaran.	32
26	Star μ Leonis' spectrum as viewed from PEPSI's spectrum viewer. The viewer can be accessed online and gives the possibility of zooming in to see the spectral lines more clearly.	33
27	HR diagram showing the evolutionary state of the studied stars as found in literature.	34

28	Maximizing function for the unnormalized absorption spectrum of star Unukalhai.	36
29	Averaging function for the unnormalized absorption spectrum of star Unukalhai. The blue function corresponds to equation 4.2 with $b_{Noise} = 0$, while the magenta function is also equation 4.2 but with $b_{Noise} = -250$, which is the useful value because it filters the tops of the peaks, which are considered to be instrumental noise.	37
30	Normalized absorption spectrum of star Unukalhai.	38
31	Inversed normalized absorption spectrum of star Unukalhai.	38
32	Line depths of VALD-3's model absorption spectrum's lines within the wavelength range [7400 Å, 7425 Å].	40
33	Line depths of VALD-3's model absorption spectrum's lines within the wavelength range [7425 Å, 7450 Å].	40
34	Line depths of VALD-3's model absorption spectrum's lines within the wavelength range [7450 Å, 7475 Å].	41
35	Line depths of VALD-3's model absorption spectrum's lines within the wavelength range [7475 Å, 7500 Å].	41
36	List of studied Ti I lines. Data taken from [20].	41
37	List of studied Fe I lines. Data taken from [20].	42
38	List of studied CN I lines. Data taken from [20].	42
39	Illustration of how the CN I lines were selected, as seen in RC star Unukalhai's spectrum.	43
40	Illustration of how the CN I lines were selected, as seen in RGB star Arcturus' spectrum.	43
41	Total set of studied Fe I, Ti I and CN I lines plotted in RC star Unukalhai's spectrum.	44
42	Total set of studied Fe I, Ti I and CN I lines plotted in RGB star Arcturus spectrum.	44
43	Unukalhai's inversed absorption spectral line Fe I 7411,1544 Å after being relocated by performing the operation $\lambda_i - 7411 \text{ Å}$	47
44	Unukalhai's normalized absorption spectral line Fe I 7411,1544 Å after being relocated by performing the operation $\lambda_i - 7411 \text{ Å}$	48
45	Natural logarithm of Unukalhai's inversed normalized absorption flux for spectral line Fe I 7411,1544 Å. The red and blue dots represent discarded data that, unlike the 23 green dots, do not adjust to the parabolic profile that the spectral line is expected to have in the $(\lambda_i, \ln(I_i))$ space.	49

46	Gaussian regression for Unukalhai's line Fe I 7411,1544 Å (shown in cyan). As can be seen, the gaussian model of the spectral line is actually a good choice, since it matches many of the original flux data, which is shown in yellow.	49
47	EW of Unukalhai's inversed absorption spectral line Fe I 7411,1544 Å, which was calculated to be approximately equal to 0,178701 Å(or 178,701 mÅ). The red area is equal to the enclosed area by the line's gaussian profile.	51
48	Illustrative diagram for how to visually obtain the EW from $N_{(\lambda_0)}$, λ_{lower} and λ_{upper}, as explained in section 6.3.	52
49	Geometric definition of the full width at half maximum (FWHM). Image taken from [11].	53
50	Equivalent Widths of the 4 Fe I lines studied in all spectra. All the uncertainties were assumed to be $\pm 5\%$ for the reasons explained in appendix A.	55
51	Equivalent Width of the line Ti I 7440,5765 Å studied in all spectra. All the uncertainties were assumed to be $\pm 5\%$ for the reasons explained in appendix A.	56
52	Equivalent Widths of the 4 CN I lines studied in all spectra. All the uncertainties were assumed to be $\pm 5\%$ for the reasons explained in appendix A.	57
53	Average EW of 4 Fe I lines, 1 Ti I line and 4 CN I lines as a function of $B - V$ index, for RC, RGB and unknown stars.	58
54	Average EW of 4 Fe I lines, 1 Ti I line and 4 CN I lines as a function of the absolute visual magnitude M_V, for RC, RGB and unknown stars.	58
55	Quotient $\frac{\overline{EW}_{Ti}}{\overline{EW}_{CN}}$ as a function of $B - V$ index for RC, RGB, AGB and unknown stars.	59
56	Quotient $\frac{\overline{EW}_{Fe}}{\overline{EW}_{CN}}$ as a function of $B - V$ index for RC, RGB, AGB and unknown stars.	59
57	Quotient $\frac{\overline{EW}_{Ti}}{\overline{EW}_{CN}}$ as a function of the absolute visual magnitude M_V for RC, RGB, AGB and unknown stars.	60
58	Quotient $\frac{\overline{EW}_{Fe}}{\overline{EW}_{CN}}$ as a function of the absolute visual magnitude M_V for RC, RGB, AGB and unknown stars.	60
59	Quotient $\frac{\overline{EW}_{Fe}}{\overline{EW}_{Ti}}$ as a function of $B - V$ index for RC, RGB, AGB and unknown stars.	61
60	Quotients $\frac{\overline{EW}_{Ti}}{\overline{EW}_{CN}}$ and $\frac{\overline{EW}_{Fe}}{\overline{EW}_{CN}}$ plotted against each other for RC, RGB, AGB and unknown stars.	62

61	Quotients $\frac{\overline{EW}_{Fe}}{\overline{EW}_{CN}}$ and $\frac{\overline{EW}_{Fe}}{\overline{EW}_{Ti}}$ plotted against each other for RC, RGB, AGB and unknown stars.	64
62	Quotients $\frac{\overline{EW}_{Ti}}{\overline{EW}_{CN}}$ and $\frac{\overline{EW}_{Fe}}{\overline{EW}_{Ti}}$ plotted against each other for RC, RGB, AGB and unknown stars.	64
63	Quotient $\frac{\overline{EW}_{Ti}}{\overline{EW}_{CN}}$ as a function of metallicity [Fe/H] for RC, RGB, AGB and unknown stars.	65
64	Quotient $\frac{\overline{EW}_{Fe}}{\overline{EW}_{CN}}$ as a function of metallicity [Fe/H] for RC, RGB, AGB and unknown stars.	65
65	Quotient $\frac{\overline{EW}_{Ti}}{\overline{EW}_{CN}}$ as a function of surface gravity log(g) for RC, RGB, AGB and unknown stars.	66
66	Quotient $\frac{\overline{EW}_{Fe}}{\overline{EW}_{CN}}$ as a function of surface gravity log(g) for RC, RGB, AGB and unknown stars.	67
67	Quotient $\frac{\overline{EW}_{Ti}}{\overline{EW}_{CN}}$ as a function of the star's mass for RC, RGB, AGB and unknown stars.	69
68	Quotient $\frac{\overline{EW}_{Fe}}{\overline{EW}_{CN}}$ as a function of the star's mass for RC, RGB, AGB and unknown stars.	69
69	3D Hertzsprung-Russell space constructed by adding the $\frac{\overline{EW}_{Ti}}{\overline{EW}_{CN}}$ dimension to the classical 2D Hertzsprung-Russell diagram.	71
70	Rotation of the top view of the 3D Hertzsprung-Russell space of figure 69 from a point of view with a +45° angle with respect to the $(B - V, \frac{\overline{EW}_{Ti}}{\overline{EW}_{CN}})$ plane. The sequence of subfigures (from 1 to 8) follows the clockwise rotation of the space around the M_V axis (i.e., the rotation vector goes in the $-\hat{M}_V$ direction) with intervals of +45°.	72
71	Rotation of the lateral views of the 3D Hertzsprung-Russell space of figure 69 from a point of view parallel to the $(B - V, \frac{\overline{EW}_{Ti}}{\overline{EW}_{CN}})$ plane. The sequence of subfigures (from 1 to 8) follows the clockwise rotation of the space around the M_V axis (i.e., the rotation vector goes in the $-\hat{M}_V$ direction) with intervals of +45°.	73
72	Rotation of the bottom view of the 3D Hertzsprung-Russell space of figure 69 from a point of view with a -45° angle with respect to the $(B - V, \frac{\overline{EW}_{Ti}}{\overline{EW}_{CN}})$ plane. The sequence of subfigures (from 1 to 8) follows the clockwise rotation of the space around the M_V axis (i.e., the rotation vector goes in the $-\hat{M}_V$ direction) with intervals of +45°.	74
73	Boundary parabolas to estimate the EW's error. The cyan parabola is the best-fit regression with X points, while the orange one has X+8 points and the pink one X-8.	84
74	Boundary gaussian regressions used to find the EW's lower and upper limits. The pink parabola gives the upper limit, while the orange one gives the lower limit.	84

75	Example of the error found for Unukalhai's line Fe I 7411,1544 Å from figures 73 and 74.	85
76	Table with the $B - V$ color index, distance, absolute visual magnitude, wavelength shift, stellar class and evolutionary status of the studied stars. All the data were obtained from [21], [24], [25], [26], [27], [28], [29], [30] and [31].	87
77	Table with the mass, surface gravity and metallicity of the studied stars. All the data were obtained from [32], [33], [34], [35], [36], [37], [38], [39], [40], [41], [42], [43], [44], [45], [46], [47], [48], [49] and [50].	88

1. Introduction

Since the beginning of the 20th century, astronomers have used the Hertzsprung-Russell diagram (hereinafter "HR diagram" and presented in figure 1) to show the relation between the luminosity and the effective temperature of stars and, from it, to better understand the stellar evolution. When nebulae (giant molecular clouds composed mostly of hydrogen) gravitationally collapse into objects of enough mass (approximately greater than or equal to 0.1 solar masses, M_{\odot}), the object releases potential gravitational energy in the form of heat and thus increases its temperature above 10 million Kelvins, point at which it starts to produce helium in its core from the fusion of hydrogen through the proton-proton chain. These newborn stars then fall somewhere along the Main Sequence (hereinafter "MS") of the HR diagram, depending on their initial mass and chemical composition.

After having spent most of their lives in the MS (i.e., fusing hydrogen), stars with masses within the range $[0.4M_{\odot}, 12M_{\odot}]$ proceed to the region of the subgiants (the sub-giant branch, SGB) and then to the Red Giant Branch (hereinafter "RGB"), stage in which all the energy of the stars comes from the fusion of the hydrogen localized in the layers surrounding their inert helium nuclei. Subsequently, stars begin to fuse that nuclear helium and transition to the Red Clump region (hereinafter "RC") located towards the red end of the Horizontal Branch (hereinafter "HB"), where they keep fusing all the helium until acquiring an inert core of carbon and oxygen with surrounding shells of helium and hydrogen, where nuclear fusion continues; these stars then finally pass to the Asymptotic Giant Branch (hereinafter "AGB"), phase in which they periodically lose mass until they die, leaving behind a white dwarf and a planetary nebula that will give birth to new stars [1]. An illustrative diagram of this stellar evolution is shown in figure 2, for the case of a star of mass $1M_{\odot}$.

In general, RC stars are hotter than RGB stars of equal luminosity (or are more luminous than RGB stars of equal temperature, as can be seen in figure 2); however, there is a part of the HR diagram where both zones overlap, making it necessary to carry out detailed asteroseismological and/or chemical studies to be able to distinguish between the evolutionary state of the stars that reside in the said overlapping region, based on their surface gravities or chemical abundances [2] [3] [4]. Several studies —like [5]— have unsuccessfully tried to find in spectroscopic variables such as abundances or isotopic ratios a reliable and simple indicator that allows RC stars to be distinguished from those of the RGB, even reaching the conclusion that said spectroscopic difference could be non-existent. However, a recent study [7] seems to have found a hint that the

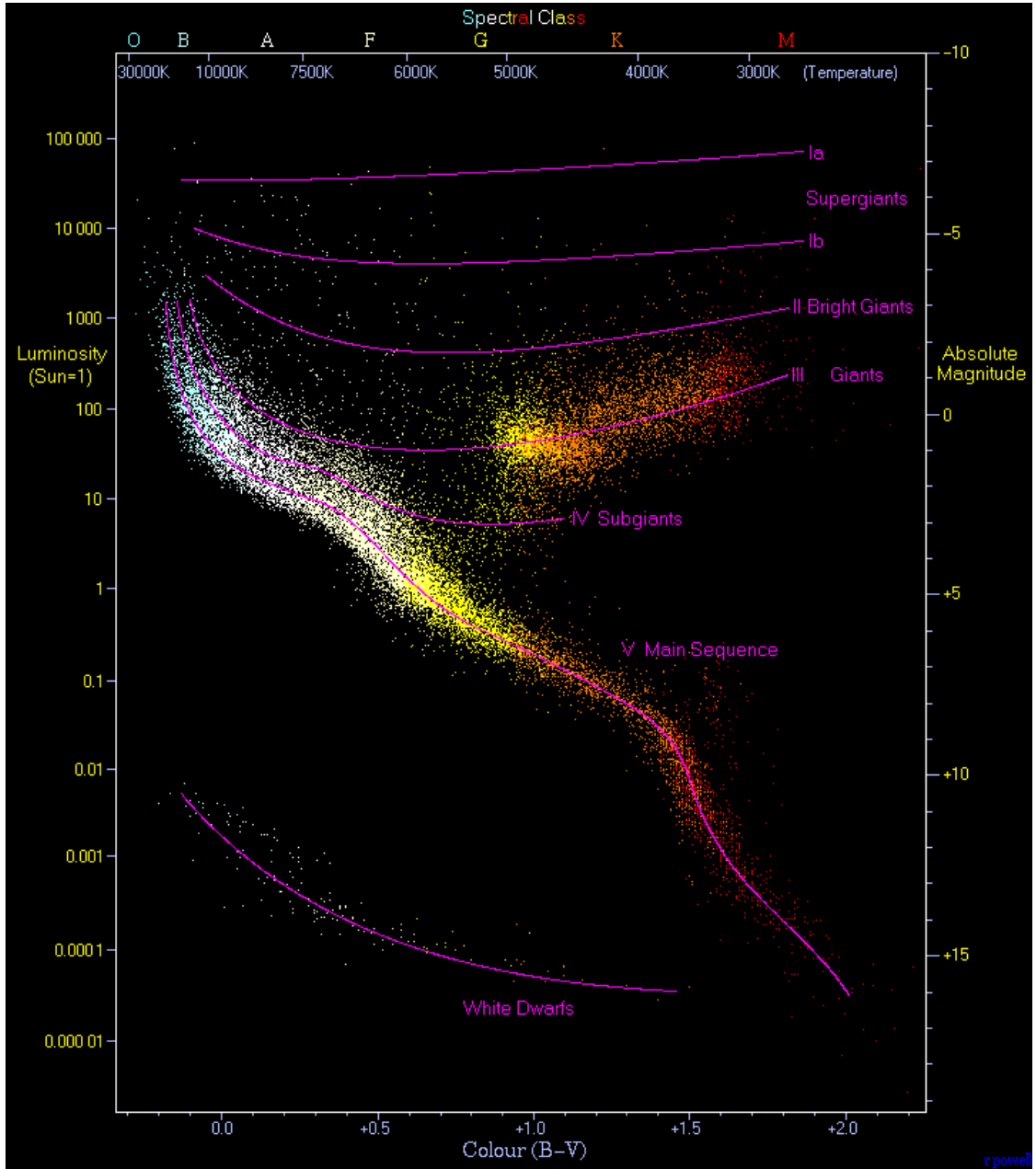


Figure 1: *Hertzsprung-Russell diagram with 22000 stars taken from Hipparcos' catalogue and 1000 stars taken from Gliese's catalogue. Taken from [6].*

spectral lines of the cyanide molecule (CN) might have a higher intensity in stars that fuse helium (the RC ones) than in similar stars that only fuse hydrogen (the RGB ones). If this were correct, the intensity of the CN lines would be the parameter that would allow RC stars to be distinguished from RGB stars by spectroscopic methods alone, something that has long been sought in astronomy. In this way, the purpose of this dissertation is to verify this hypothesis by exhaustively analysing the spectra of multiple stars belonging to the disk of the Milky Way, all of them in the intersection area between the RC and the RGB.

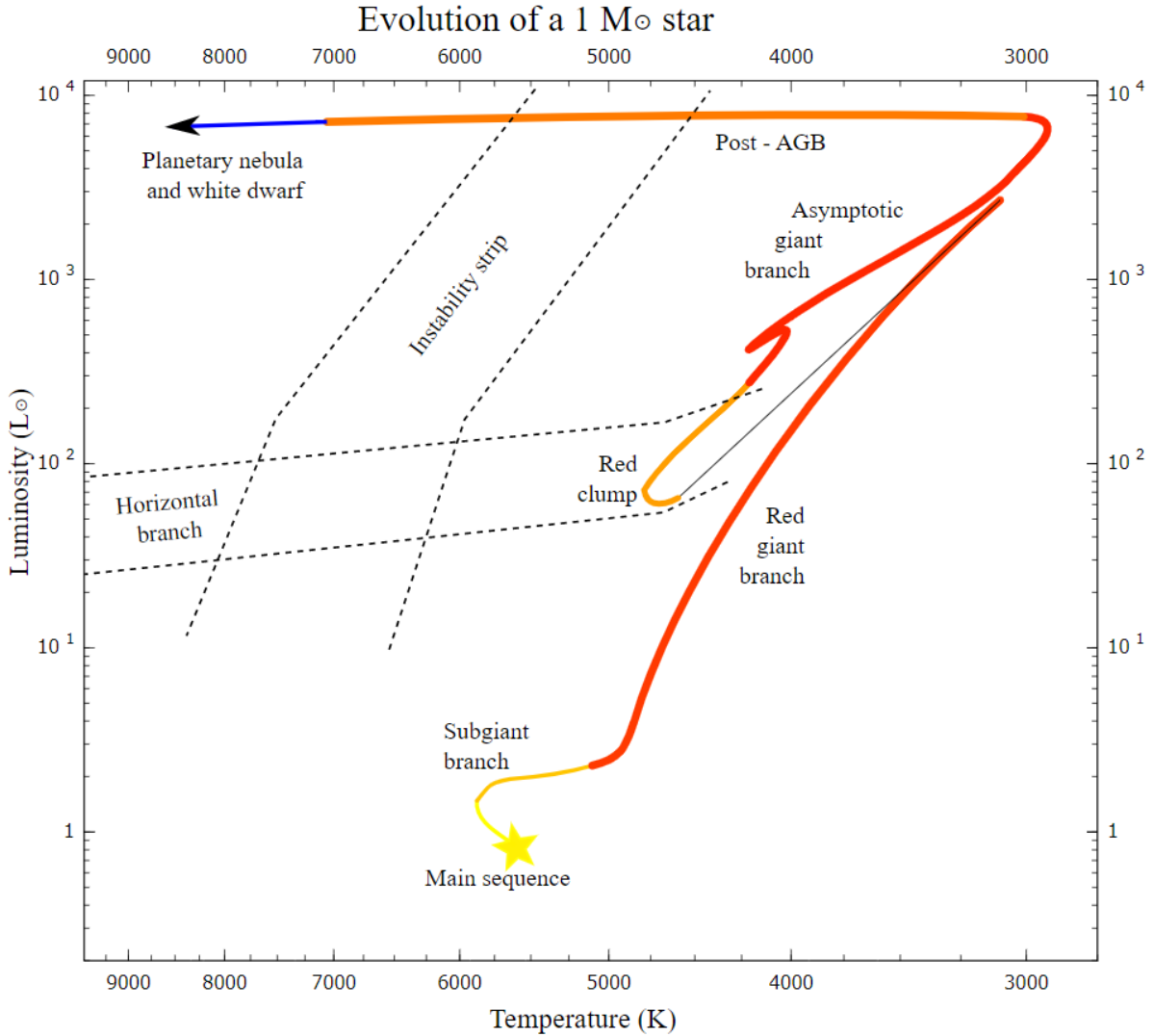


Figure 2: Stellar evolution of a star of $1M_{\odot}$. After leaving the Main Sequence (MS), the star passes to the Subgiant branch (SGB) and then to the Red Giant Branch (RGB). Subsequently, it spends time in the Red Clump (RC) and in the Horizontal Branch (HB) and ends up in the Asymptotic Giant Branch (AGB), phase at which it begins to lose mass until it dies, leaving a white dwarf and a planetary nebula behind. Image taken from [8].

2. Theoretical framework

The following is intended to delve into what has been previously stated in section 1 and to introduce some of the basic concepts and tools used in astronomy, so that the reader is familiarized with the ideas and notation used throughout the dissertation.

2.1. Mapping the sky: the Hipparcos mission

For several hundred years, the measurement of star positions was the main activity of astronomers due to the fact that all astronomical observations had to be performed from ground-based observatories, what made the task incredibly difficult and time-consuming given that factors such as perturbations in the atmosphere, lack of sky visibility and gravitational and thermal flexure of telescopes could not be avoided. However, in 1989 the European Space Agency (ESA) launched the HIgh Precision PARallax COLlecting Satellite (Hipparcos, shown in figure 3), the first project in the history of humankind devoted to precise astrometry directly from space, thus by-passing many of the previous difficulties. Subsequently, with the high-precision measurements of the positions, parallaxes and apparent magnitudes of the 118218 stars that compose the Hipparcos catalogue, astronomers were finally able to calculate the nearby stars' proper motions and radial distances (as seen from Earth) with great accuracy for the first time (the first attempts to do so were made from the ground in the early 19th century, but clearly lacked precision), thereby starting a new era in astronomy. Nowadays (2022) the most precise spacecraft dedicated to astrometry is Hipparcos' successor, Gaia, which was launched in 2013 as a part of ESA's Horizon 2000+ long-term scientific program and is expected to keep operating in a Lissajous orbit around the Sun-Earth L_2 Lagrangian point until 2025, aiming to construct the largest and most precise 3D catalog ever made with more than 1 billion astronomical objects —mainly stars—, a huge number that only represents 1% of the estimated Milky Way population anyway.

2.2. Calculating the distance to a star: the stellar parallax

To calculate the distance to a star, astronomers recur to the trigonometric parallax, a technique of triangulation in which the observer measures the angular position of an object from two observation points separated by a known baseline distance. In the specific case of astronomy, it refers to the apparent displacement of a nearby star as seen from

an observer on Earth, as shown in figure 4. Basic trigonometry allows to see that the distance to the star (D) and the parallax angle (plx) are connected by the relationship

$$D = \frac{1\text{AU}}{\tan(plx)} \approx \frac{1\text{AU}}{plx}, \quad (2.1)$$

where the approximation $\tan(\theta) \approx \theta$ was used since the parallax angles of stars are very small.



Figure 3: The Hipparcos satellite being tested under the Large Solar Simulator prior to the start of the mission in 1989. Image taken from [9].

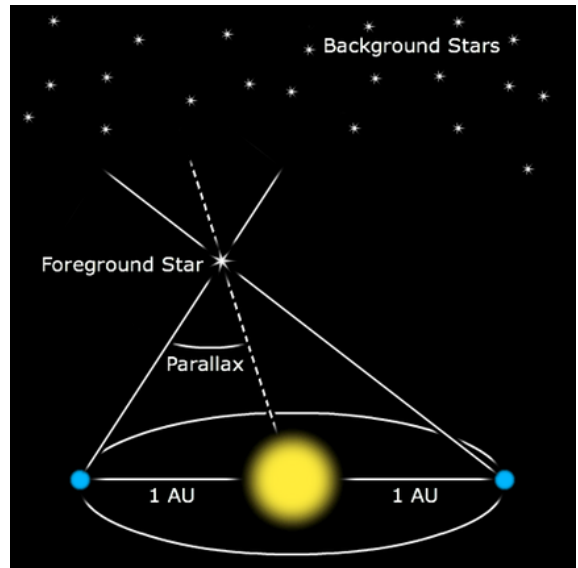


Figure 4: Illustrative diagram for how the stellar parallax is calculated. The blue circle is the Earth, which orbits the Sun —the yellow circle—with an orbital radius of 1 astronomical unit (AU). Image taken from [10].

If the parallax angle is of the order of miliarcseconds (m.a.s)—what is always the case for the closest stars to Earth—the following formula can be used to approximate the distance to the object:

$$D = \frac{1000}{plx}, \quad (2.2)$$

where (plx) is the parallax angle observed in [m.a.s] and D is the actual distance to the object given in parsecs [pc], which are defined as the distance at which an object has a parallax of 1 arcsecond, which is approximately equal to 3,26 light-years or 206265 astronomical units (AU) [11].

2.3. Measuring the energy radiated by a star

2.3.1. The apparent magnitude (m)

Back in ancient Greece, astronomer Hipparchus —one of the first sky watchers to catalog stars— tried to describe how bright each star appeared in the sky and thus assigned an **apparent magnitude** $m = 1$ to the brightest ones and $m = 6$ to the dimmest ones. Astronomers have continued to use that method since then and have thus extended Hipparchus' scale in both directions, from $m = -26,83$ for the Sun to $m = 30$ for the faintest object detectable. By the modern definition, a difference of 5 apparent magnitudes corresponds exactly to a factor of 100 in brightness, which means that a difference of $\Delta m = 1$ corresponds exactly to a brightness ratio of $100^{1/5} \approx 2,512$. Consequently, a first-magnitude star appears 2,512 times brighter than a second-magnitude star and $2,512^2 = 6,310$ times brighter than a third-magnitude star and so on [11].

2.3.2. Flux, luminosity and the inverse square law

In physics, the "brightness" of a star is actually measured in terms of the radiant flux received from the star, which is the total amount of light energy of all wavelengths that crosses a unit area (say, the detector) oriented perpendicularly to the direction of the light's travel per unit time. If one assumes that no light is absorbed during its journey to the observer, then the radiant flux F measured at a distance r from the center of the star is related to the intrinsic luminosity (L , the energy emitted per unit time by the star) by means of equation

$$F = \frac{L}{4\pi r^2}, \quad (2.3)$$

which is the well-known **inverse square law for light** [11].

2.3.3. The absolute magnitude

Using equation 2.3, astronomers are able to assign an absolute magnitude (M) to each star, which is defined to be the apparent magnitude a star would have if it were located at a distance of 10 pc. Since a difference of 5 apparent magnitudes corresponds to a factor of 100 in brightness —as was discussed at the beginning of this subsection—, the flux ratio of two stars is given by

$$\frac{F_2}{F_1} = 100^{\frac{m_1 - m_2}{5}}. \quad (2.4)$$

Mixing equations 2.3 and 2.4 for the case of a single star seen from two different distances (10 pc and D), one can easily get to

$$m - M = 5\log_{10}\left(\frac{D}{10pc}\right), \quad (2.5)$$

which is the well-known **distance modulus equation**, which relates the star's distance, apparent magnitude and absolute magnitude [11].

If one now considers the case of two stars at the same distance, a similar procedure leads to equation 2.4 becoming

$$\frac{L_2}{L_1} = 100^{\frac{M_1 - M_2}{5}}, \quad (2.6)$$

and letting one of those stars be the Sun reveals the direct relationship between a star's absolute magnitude and its luminosity:

$$L = L_{\odot}10^{\left(\frac{M_{\odot} - M}{2.5}\right)}, \quad (2.7)$$

where $L_{\odot} = 3,839 \times 10^{26}$ [W] and $M_{\odot} = +4,74$ are the Sun's luminosity and absolute visual magnitude, respectively [11].

2.4. The color and temperature of a star

2.4.1. The connection between color and temperature

It is known since the 19th century that any object with a temperature above absolute zero emits light of all wavelengths with varying degrees of efficiency. If stars are considered **blackbodies** (i.e., objects that absorb and reradiate all of the light energy incident upon them), then one finds that they emit a continuous spectrum with some energy at all wavelengths described by the Planck function plotted in figure 5,

$$B_{\lambda(T)} = \frac{\frac{2hc^2}{\lambda^5}}{e^{\frac{hc}{\lambda K_B T}} - 1}, \quad (2.8)$$

where $h = 6,621 \times 10^{-34}$ [J.s] is Planck's constant, T [K] is the absolute temperature of the object, λ [m] is the wavelength of the emitted light, $K_B = 1,381 \times 10^{-23}$ [$\frac{J}{K}$] is Boltzmann's constant and $c = 299792458$ [$\frac{m}{s}$] is the speed of light. It can be seen

that the spectrum peaks at a wavelength λ_{max} that becomes shorter with increasing T , a relationship known as **Wien's displacement law**:

$$\lambda_{max}T = 0,002897755 \text{ m.K} \quad (2.9)$$

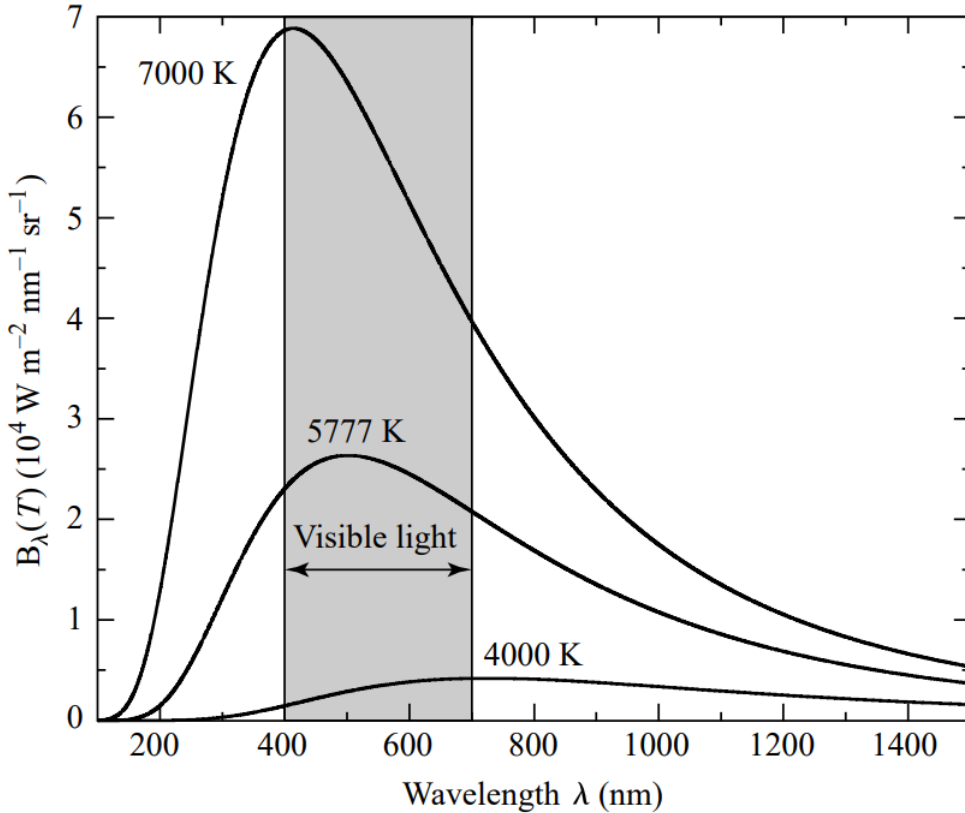


Figure 5: *Blackbody spectrum (Planck function $B_{\lambda(T)}$).* Image taken from [11].

Experiments performed by Josef Stefan in 1879 showed that the luminosity of a blackbody of surface area A is given by equation

$$L = \sigma AT^4, \quad (2.10)$$

where $\sigma = 5,670 \times 10^{-8} \left[\frac{W}{m^2 K^4} \right]$ is the Stefan-Boltzmann constant. For the specific case of a star of radius R and an effective surface temperature T_{eff} , this ends up leading to equation

$$L = 4\pi R^2 \sigma T_{eff}^4, \quad (2.11)$$

which can be used to reckon the radius R of the star's photosphere if T_{eff} and L are already known [11].

2.4.2. The color index

The apparent and absolute magnitudes discussed in section 2.3 are actually measured over all wavelengths of light emitted by the star and are thus known as bolometric magnitudes, denoted m_{bol} and M_{bol} , respectively. Nonetheless, in practice astronomers actually measure the radiant flux of a star only within a certain wavelength region defined by the sensitivity of the detector. In the standard UBV system, a star's apparent magnitude is measured through three filters and designated by three capital letters [11]:

- U, the star's apparent ultraviolet magnitude, measured through a filter centered at 365 nm with 68 nm as effective bandwidth.
- B, the star's apparent blue magnitude, measured through a filter centered at 440 nm with 98 nm as effective bandwidth.
- V, the star's apparent visual magnitude, measured through a filter centered at 550 nm with 89 nm as effective bandwidth.

Hence, the $B - V$ color index, for example, is defined as

$$B - V = M_B - M_V, \quad (2.12)$$

where (B, M_B) and (V, M_V) are related by equation 2.5.

Moreover, if stars are considered blackbodies, it is possible to use Ballesteros' formula to obtain an estimate of the star's effective surface temperature [12]:

$$T_{eff} = 4600K \left(\frac{1}{0,92(B - V) + 1,7} + \frac{1}{0,92(B - V) + 0,62} \right). \quad (2.13)$$

Thus, the larger the color index, the redder (or cooler) the object is and, conversely, the smaller the color index, the bluer (or hotter) the object is. Table 6 shows typical color indexes values and their correspondent effective surface temperatures for different classes of stars.

2.5. Dissecting the light of a star: the spectral lines

In 1802, William Wollaston passed sunlight through a prism to produce a rainbow-like spectrum and discovered that a number of dark spectral lines were superimposed on the continuous spectrum at points where the Sun's light had been absorbed at certain discrete wavelengths. In the following years, many of these dark lines were catalogued and, with

Class	B-V	U-B	V-R	R-I	T_{eff} (K)
O5V	-0.33	-1.19	-0.15	-0.32	42,000
B0V	-0.30	-1.08	-0.13	-0.29	30,000
A0V	-0.02	-0.02	0.02	-0.02	9,790
F0V	0.30	0.03	0.30	0.17	7,300
G0V	0.58	0.06	0.50	0.31	5,940
K0V	0.81	0.45	0.64	0.42	5,150
M0V	1.40	1.22	1.28	0.91	3,840

Figure 6: Typical effective surface temperatures and color indexes for different classes of stars. Image taken from [13].

the prism spectroscope invented by Joseph von Fraunhofer (shown in figure 7), Robert Bunsen and Gustav Kirchhoff found that they actually corresponded exactly to the bright emission lines of heated elements in the laboratory, what led to the revolutionary idea that every element produces its own pattern of spectral lines and thus may be identified by its unique spectral line "fingerprint". The production of these lines is summarized in the three Kirchhoff's laws [11]:

- A hot, dense object produces a continuous spectrum with no dark spectral lines, described by the Planck function (equation 2.8).
- A hot, diffuse gas produces bright emission lines that are produced when an electron makes a downward transition from a higher energy orbit to a lower energy orbit, thus losing an amount of energy (ΔE) that is carried away by a single photon of frequency $f = \frac{\Delta E}{h}$.
- A cool, diffuse gas in front of a source of continuous spectrum produces dark absorption lines in the continuous spectrum, produced when an electron makes a transition from a lower energy orbit to a higher energy orbit by absorbing a photon of energy $\Delta E = hf$.

Since the spectral lines are the elements' fingerprints, this discovery also allowed to determine the radial velocity of stars (v_r) by means of **the non-relativistic Doppler shift equation**:

$$\frac{\lambda_{\text{obs}} - \lambda_{\text{rest}}}{\lambda_{\text{rest}}} = \frac{\Delta\lambda}{\lambda_{\text{rest}}} \approx \frac{v_r}{c}, \quad (2.14)$$

where λ_{rest} is the spectral line's measured wavelength at rest (in the laboratory) and λ_{obs} the spectral line's observed wavelength in the spectrum of the star.

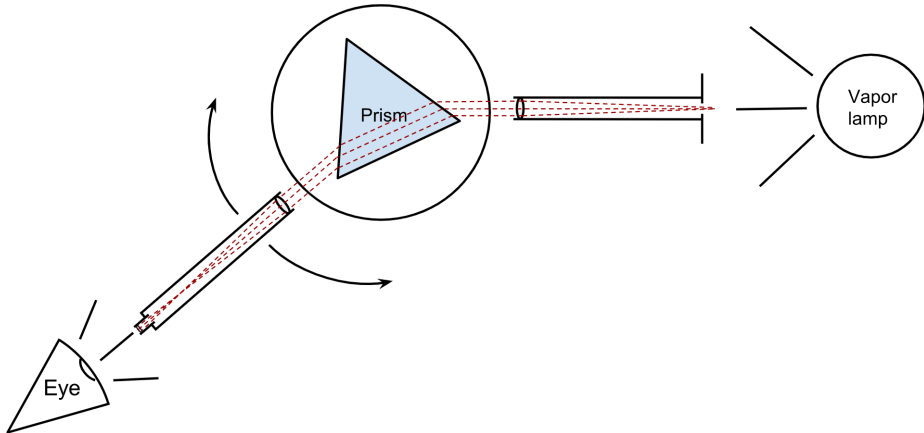


Figure 7: Diagram of a prism spectroscope. The light emitted from the vapor lamp is parallelized with a collimator and then passed through a prism in which it is refracted twice (once when entering and once when leaving). Since the angle with which light is refracted depends on its wavelength, this leads to a spectrum of thin lines of light, each observable at a different angle, which can be used to compute the wavelength. Image taken from [11].

2.5.1. The strength of a spectral line: the Equivalent Width (EW)

The strength of a spectral line is measured in terms of its equivalent width EW , which is defined as [11]

$$EW = \int_{-\infty}^{\infty} \left[\frac{F_c - F_{(\lambda)}}{F_c} \right] d\lambda, \quad (2.15)$$

where $F_{(\lambda)}$ is the radiant flux of the spectral line and F_c is the value of the flux from the continuous spectrum outside the spectral line (i.e., the maximum possible flux). Geometrically speaking, the EW would then be the width of a box reaching up to the continuum that has the same area as the spectral line, as can be seen in figure 8.

It must also be noted that, when the spectrum is normalized in such a way that the maximum possible intensity is $F_c = 1$ (with arbitrary flux units), equation 2.15 reduces to

$$EW = \int_{-\infty}^{\infty} [1 - N_{(\lambda)}] d\lambda, \quad (2.16)$$

where $N_{(\lambda)} \equiv \frac{F_{(\lambda)}}{F_c}$ is the normalized flux of the spectral line.

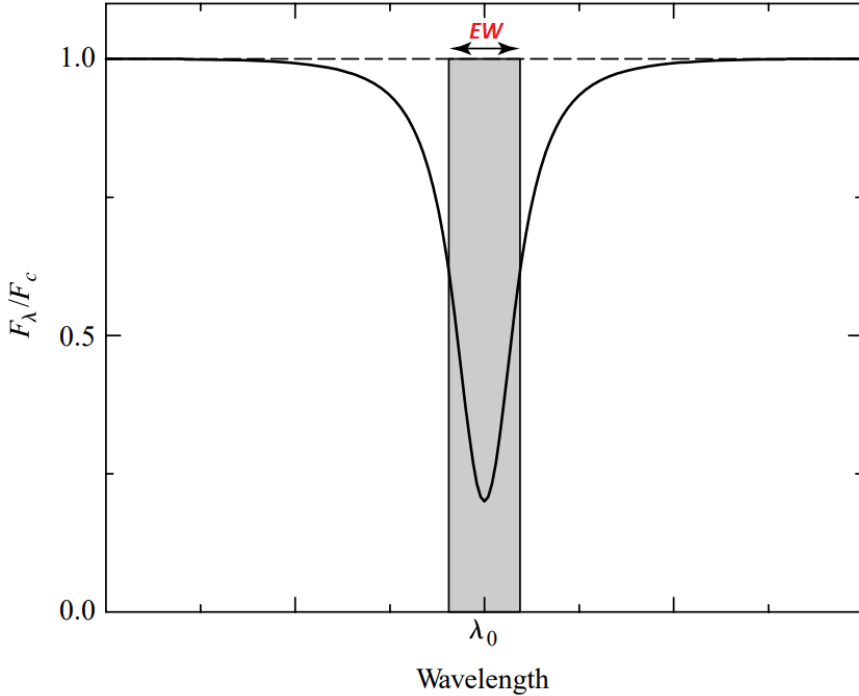


Figure 8: Geometrical definition of the Equivalent Width (EW) of a spectral line. Image taken from [11].

2.5.2. How spectral lines are broadened

Although spectral lines are formed when an absorption or emission of a photon with an energy equivalent to $\Delta E = \frac{hc}{\lambda_0}$ happens, they cannot be infinitely sharp as equation $\lambda_0 = \frac{hc}{\Delta E}$ would initially suggest; the absorption or emission line has indeed its maximum (or minimum) at $\lambda = \lambda_0$, but there exist three main mechanisms that broaden the line [11]:

- **Natural broadening:** This follows from Heisenberg's uncertainty principle $\Delta E \approx \frac{\hbar}{\Delta t}$, what ends up giving a broadening of

$$\Delta\lambda_N \approx \frac{\lambda_0^2}{2\pi c} \left(\frac{1}{\Delta t_i} + \frac{1}{\Delta t_f} \right), \quad (2.17)$$

which is usually of the order of 1×10^{-5} nm and where Δt_i is the lifetime of the electron in its initial state and Δt_f the lifetime in the final state.

- **Doppler broadening:** If one considers stars as gases following the Maxwell-Boltzmann distribution, then the light absorbed or emitted by their atoms is Doppler-shifted by means of equation 2.14, thus giving

$$\Delta\lambda_D \approx \frac{2\lambda_0}{c} \sqrt{\frac{2K_B T}{m}}, \quad (2.18)$$

which is of the order of 1×10^{-2} nm and where m is the mass of the atom that produces the spectral line.

- **Pressure and collisional broadening:** This comes from the fact that the orbitals of an atom can be perturbed in a collision with a neutral atom or by a close encounter involving the electric field of an ion, what gives a broadening

$$\Delta\lambda_{PC} = \frac{\lambda_0^2}{c} \frac{1}{\pi\Delta t_0} \approx \frac{\lambda_0^2 n\sigma}{c} \sqrt{\frac{2K_B T}{m}}, \quad (2.19)$$

which is of the order of 1×10^{-5} nm and where σ is the atom's collision cross section and n is the number density of the atoms.

2.5.3. A way to calculate abundances

The model explained here for calculating the lines' profiles makes the basic assumption that the star's photosphere acts as a source of blackbody radiation and that the atoms above it remove photons from this continuous spectrum, thus forming absorption lines; however, an element's greater EW does not necessarily imply something as simple as the star being made of primarily that element, for the EW depends not only on the abundance of the element but also on the quantum-mechanical details of how atoms absorb photons, thus making the ionization state of the atom or molecule even more important. If those variables are taken into account properly and curves of growth are available (such as the one shown in figure 9), then it is even possible to use the Boltzmann and Saha equations to estimate N_a , the number of absorbing atoms per unit area that have electrons in the proper orbital for absorbing a photon at the wavelength of the spectral line [11].

2.6. Stellar classification: the different kinds of stars

Most stars are currently classified under the Morgan-Keenan (MK) system, which gives stars both a spectral and a luminosity class. The former consists of one letter from the sequence {O, B, A, F, G, K, M} —which form a temperature sequence from the hottest (O type) to the coolest (M type)— and a numeric digit from 0 to 9 that marks the sublevel, being 0 the hottest and 9 the coolest; thus, for example, {B1, B9, A0, A1, F5, G8, K1} form a sequence from hotter to cooler. Figure 10 shows the main characteristics of each spectral type.

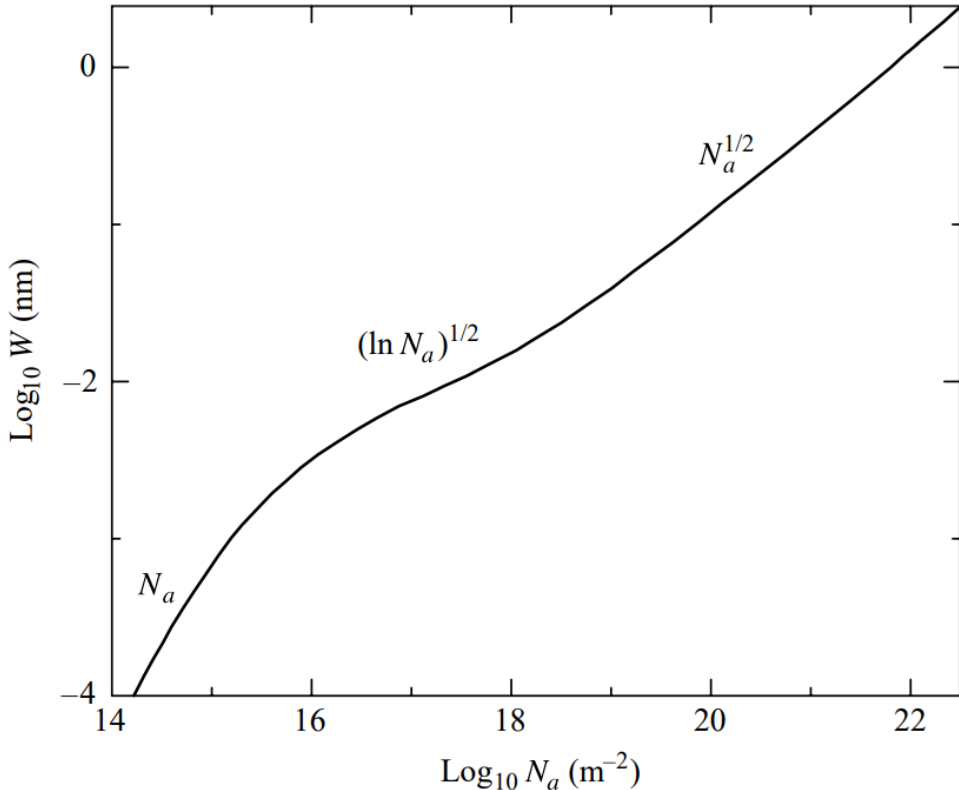


Figure 9: Curve of growth for the K line of Ca II. As N_a increases, the functional dependence of the equivalent width (W) changes. Image taken from [11].

In the case of the luminosity, the MK system adds a roman numeral from 0 to VII. Luminosity class 0 or Ia+ is used for hypergiants, class I for supergiants, class II for bright giants, class III for regular giants, class IV for subgiants, class V for Main Sequence stars, class VI for subdwarfs and class VII for white dwarfs, as can be seen in figure 1, which shows very clearly both the spectral and luminosity classes in the HR diagram . In general, for stars of the same spectral type, narrower lines are produced by more luminous stars, as is suggested by the pressure and collisional broadening of equation 2.19: since the less luminous and smaller stars of the MS have denser atmospheres (i.e., greater n in equation 2.19), collisions occur more frequently and thus the absorption spectral lines are broadened more. Figure 11 exhibits the digitized spectra of some MS classes and, besides, figure 12 displays the dependence of some spectral line strengths on temperature [11].

2.7. Stellar evolution: the life cycle of a star

The life of a star begins when part of a nebula's material (which is mainly hydrogen) gravitationally collapses into an object that, if it has enough mass ($\geq 0, 1M_\odot$), starts releasing potential gravitational energy in the form of heat and thus increases its temperature over millions of years until it reaches a temperature above 10 million Kelvins, point at which

Spectral Type	Characteristics
O	Hottest blue-white stars with few lines Strong He II absorption (sometimes emission) lines. He I absorption lines becoming stronger.
B	Hot blue-white He I absorption lines strongest at B2. H I (Balmer) absorption lines becoming stronger.
A	White Balmer absorption lines strongest at A0, becoming weaker later. Ca II absorption lines becoming stronger.
F	Yellow-white Ca II lines continue to strengthen as Balmer lines continue to weaken. Neutral metal absorption lines (Fe I, Cr I).
G	Yellow Solar-type spectra. Ca II lines continue becoming stronger. Fe I, other neutral metal lines becoming stronger.
K	Cool orange Ca II H and K lines strongest at K0, becoming weaker later. Spectra dominated by metal absorption lines.
M	Cool red Spectra dominated by molecular absorption bands, especially titanium oxide (TiO) and vanadium oxide (VO). Neutral metal absorption lines remain strong.
L	Very cool, dark red Stronger in infrared than visible. Strong molecular absorption bands of metal hydrides (CrH, FeH), water (H ₂ O), carbon monoxide (CO), and alkali metals (Na, K, Rb, Cs). TiO and VO are weakening.
T	Coolest, Infrared Strong methane (CH ₄) bands but weakening CO bands.

Figure 10: *Main characteristics of the MK system's spectral types. Image taken from [11].*

it starts producing helium in its core from the fusion of hydrogen via the proton-proton (pp) chain. These newborn stars then fall somewhere along the MS of the HR diagram depending on their initial mass and chemical composition, as is shown in figure 13.

2.7.1. Main Sequence (MS) evolution

Although all stars on the MS are converting hydrogen into helium and thus share similar evolutionary characteristics, some differences do exist, being the dominant energy-production process the most important one. For stars within the range $[0.3M_{\odot}, 1.2M_{\odot}]$, the pp-chain is the dominant process and hence they have cores that transmit energy predominantly by radiation. As the low-mass star evolves along the MS, eventually all

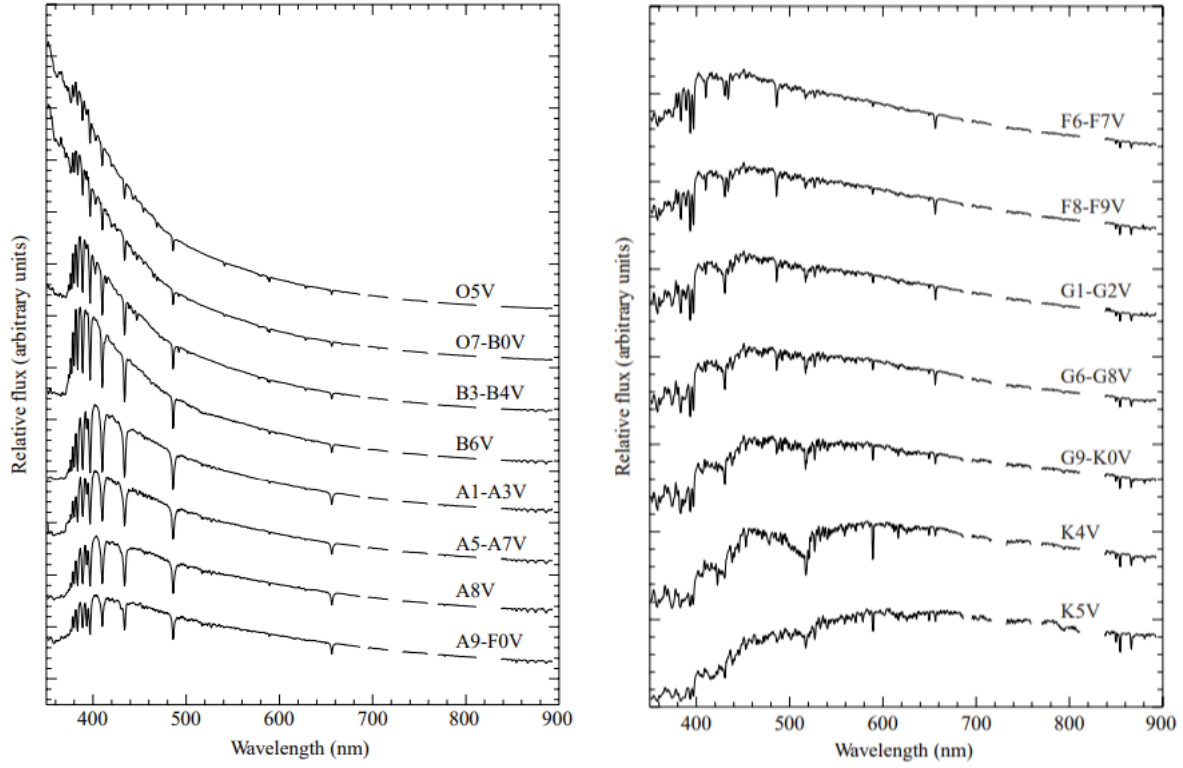


Figure 11: *Digitized spectra of Main Sequence classes O5-K5 displayed in terms of relative flux as a function of wavelength. Figures taken and adapted from [11].*

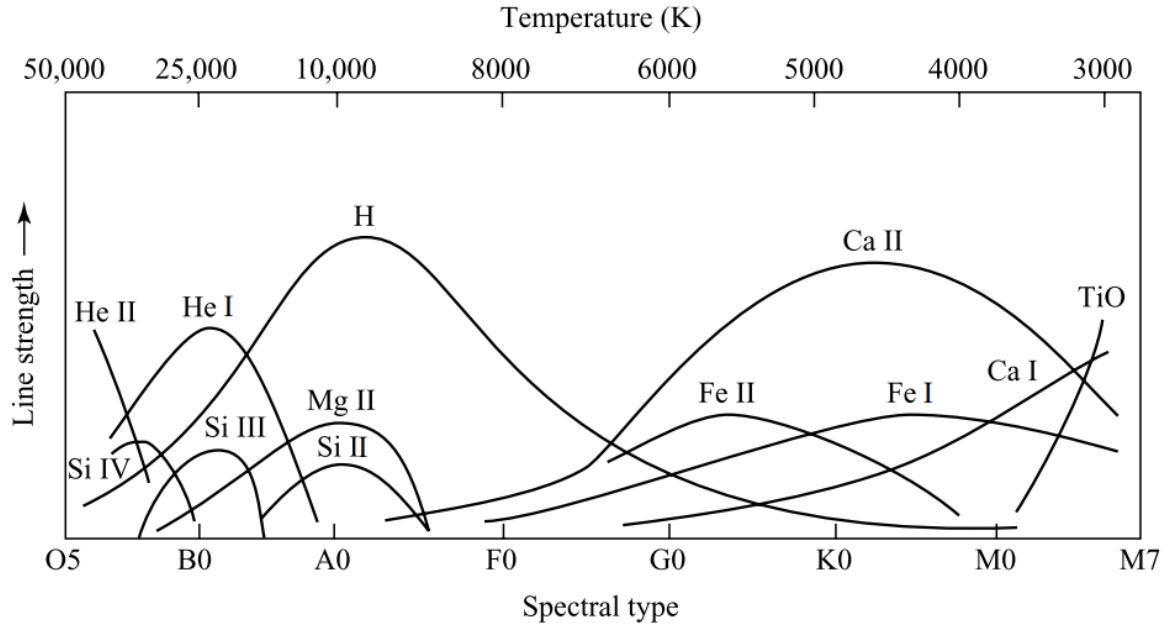


Figure 12: *Dependence of spectral line strengths on temperature. Image taken from [11].*

the hydrogen at its center is completely depleted (point 3 of the evolutionary tracks shown in figure 13) and the core turns into an inert helium mass that keeps growing due to the

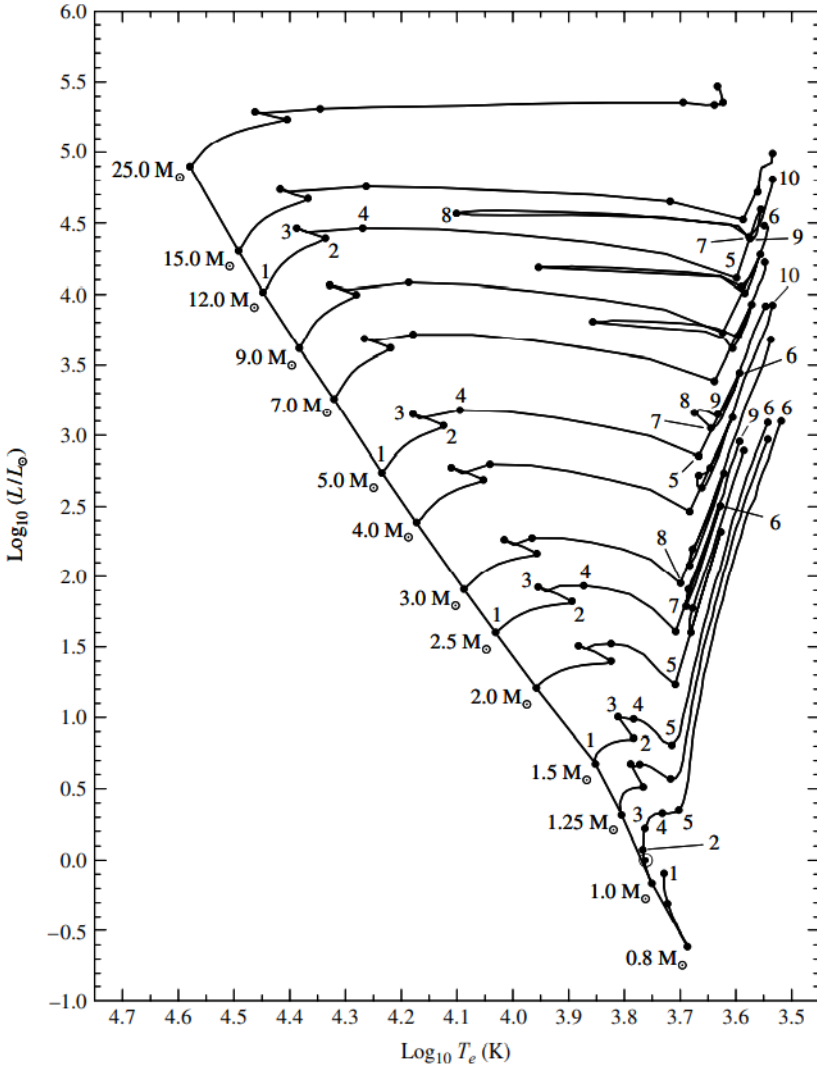


Figure 13: *Evolutionary tracks for stars with different initial compositions. The more massive the star, the less time it takes it to complete its evolutionary track.* Image taken from [13].

helium production that keeps going on a hydrogen shell around it, which radiates even more energy than the previous hydrogen-burning core and thus makes the star ascend in the HR diagram.

On the other hand, more massive stars ($\geq 1.2 M_\odot$) achieve higher temperatures and thus their dominant energy-production process is the CNO cycle, which produces more energy than the pp-chain and thus makes more massive stars have convective cores, which transmit energy in a more efficient way than radiative cores and mix the star's material, keeping the core composition nearly homogeneous. These stars are said to end their MS phase when their mass fraction of hydrogen reaches about $X = 0.05$ in the core, point at which they start to contract [11].

2.7.2. The Subgiant Branch (SGB)

For both low- and intermediate-mass stars, as the shell continues to consume the available hydrogen at the base of the star's envelope, the helium core steadily increases in mass and becomes nearly isothermal until the Schönberg-Chandrasekhar limit is reached (point 4 in figure 13), causing the core to contract and the envelope to expand, thus reducing the effective temperature, what results in a redward movement in the HR diagram.

2.7.3. The Red Giant Branch (RGB)

As a consequence of the stellar envelope's expansion and the decrease in effective temperature, the photospheric opacity increases due to the additional contribution of the H^- ion and, as a result, a convection zone develops near the surface for both low- and intermediate-mass stars. As the evolution continues toward point 5 in figure 13, the convection zone extends deep into the interior of the star, increasing the energy transmission efficiency and causing a rapid ascent along the RGB of the HR diagram. When the convection zone encounters regions where the chemical composition has been modified by nuclear processes, the processed material becomes mixed with the material above it, causing observable changes in the composition of the photosphere (such as decreases in lithium and nitrogen compositions, as well as helium and carbon increases) that collectively form what is called **the first dredge-up** phase, which can be appreciated in figures 14 and 15, which depict the evolution of low- and intermediate-mass stars, respectively [11].

2.7.4. The Helium Core Flash

When stars reach the tip of the RGB (points 6 in figure 13), the central density and temperature become high enough that quantum-mechanical tunneling becomes effective through the Coulomb barrier acting between helium nuclei, allowing the triple alpha process to begin in an explosive way that makes the core reach luminosities as high as $10^{11} L_\odot$, comparable to that of an entire galaxy. However, most of this energy never even reaches the surface, but is instead absorbed by the overlying layers of the envelope, which are pushed outward and thus cool, resulting in an abrupt decrease in the luminosity of the star and a contraction of its envelope [11].

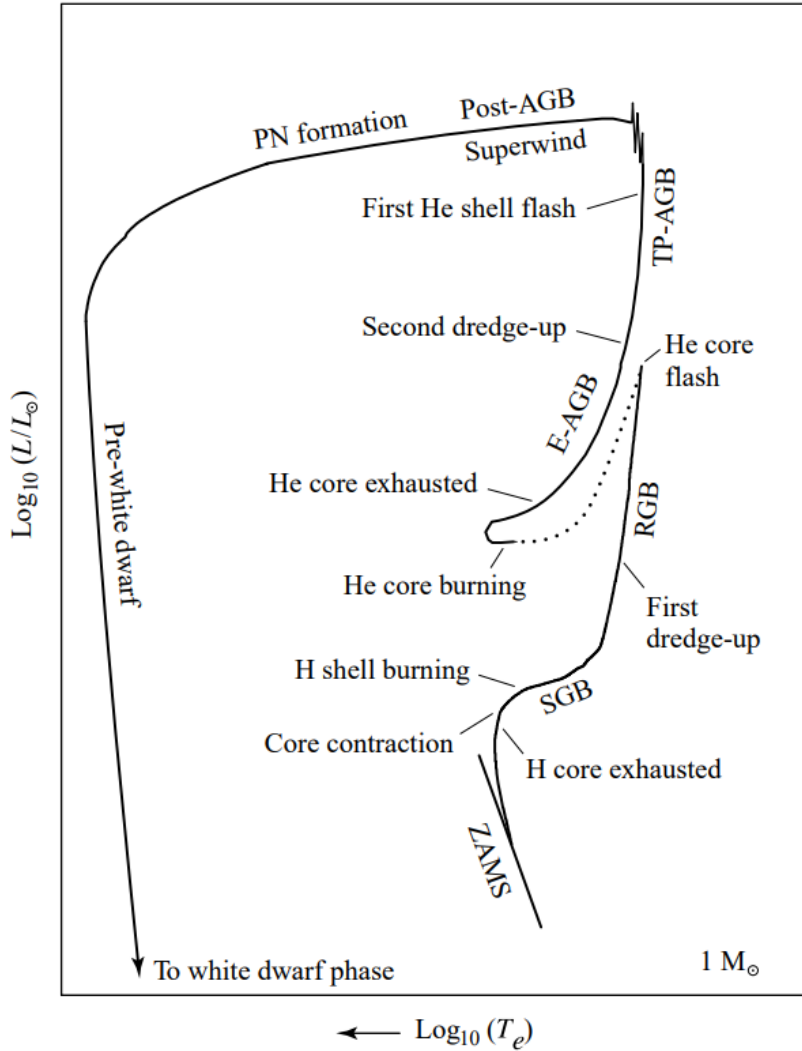


Figure 14: A schematic diagram of the evolution of a low-mass star of $1 M_{\odot}$ from its birth in the MS to the formation of a white dwarf. The dotted phase represents the rapid evolution following the helium core flash. Image taken from [11].

2.7.5. The Horizontal Branch (HB)

For both low- and intermediate-mass stars, as the star's envelope contracts following the RGB tip, the increasing compression of the hydrogen-burning shell ends up causing the energy output of the star to begin to increase again, what makes the effective temperature rise and creates a convective core as a consequence of the triple alpha process' high temperature sensitivity. The result of this is a blueward motion along the HB (as shown in figures 14 and 15) that is essentially the helium-burning analog of the hydrogen-burning MS, but with a much shorter time scale. Later on, briefly after beginning the redward portion of the HB loop, the He core gets completely exhausted after being fused into carbon and oxygen, ultimately causing the CO core to contract rapidly, as was the case with the He core during the post-MS evolution along the SGB [11].

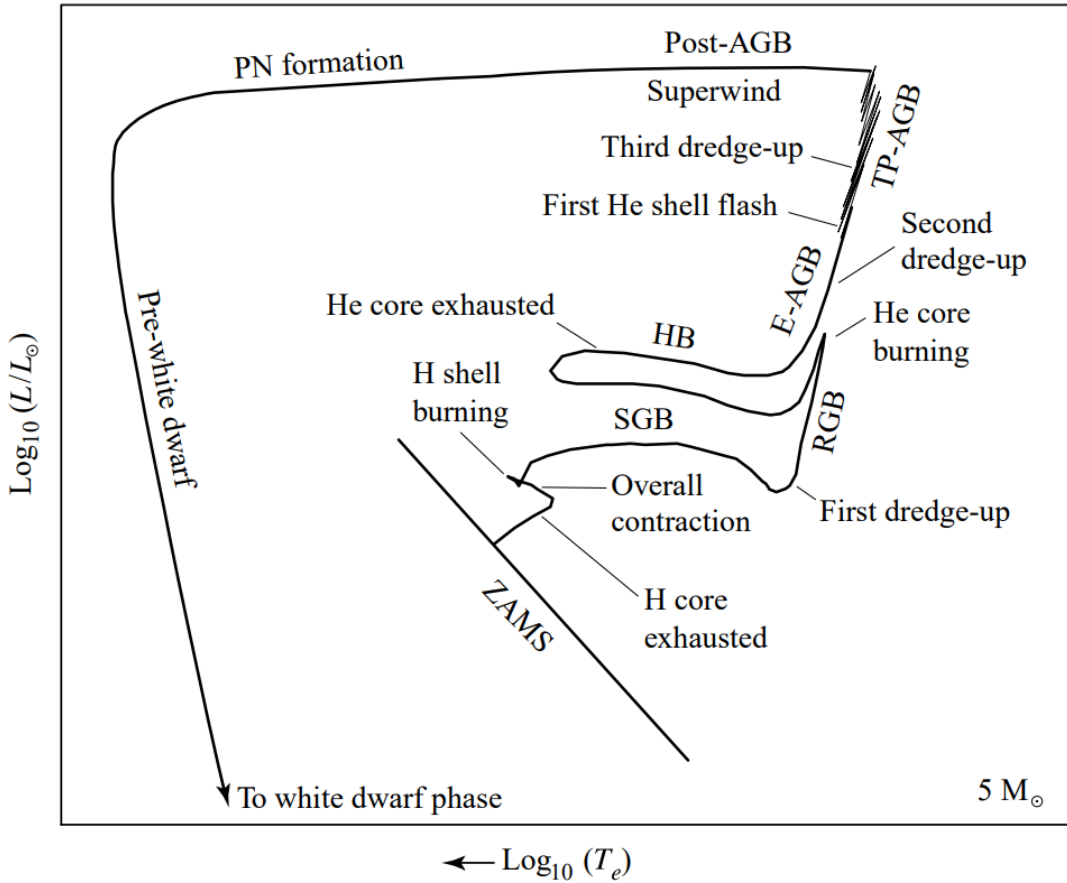


Figure 15: A schematic diagram of the evolution of an intermediate-mass star of $5 M_{\odot}$ from its birth in the MS to the formation of a white dwarf. Image taken from [11].

2.7.6. The Early Asymptotic Giant Branch (E-AGB)

The next step of the process, the Asymptotic Giant Branch (AGB), gets its name from the fact that it approaches the RGB asymptotically from the left and may be thought of as the helium-burning-shell analog to the hydrogen-burning-shell RGB. During the Early Asymptotic Giant Branch phase (E-AGB), the energy produced from helium fusion dominates the star's energy output and makes the star expand, what forces the surface temperature to decrease and the opacity to increase, thereby making the convective envelope to deepen again, resulting in **the second dredge-up**, a second chemical mixing that this time increases the surface content of helium and nitrogen [11].

2.7.7. The Thermal-Pulse Asymptotic Giant Branch (TP-AGB)

On the upper portion of the AGB lies the next phase of the star's life, the thermal-pulse AGB (TP-AGB), in which the hydrogen-burning shell reignites and dominates the energy

output, but this time competing with a narrowing helium-burning shell that begins to turn on and off in a quasi-periodic way that provokes abrupt luminosity changes at the surface that astronomers can identify clearly. Because of the sudden increase in energy flux due to these helium-shell flashes, a convection zone is established between the helium-burning shell and the hydrogen-burning shell and, if the star is big enough (mass $\geq 2M_{\odot}$), it extends down into regions that have been chemically changed before, thus causing a **third dredge-up phase** in which the carbon-rich material is brought to the surface, decreasing the ratio of oxygen to carbon [11].

2.7.8. The Post-Asymptotic Giant Branch (Post-AGB)

During the Post-AGB, the star moves blueward in the HR diagram and makes heavier elements such as neon and magnesium at its core during a mass-loss stage whose mechanisms are still not well-understood, but that are known to rapidly deplete the star's envelope, causing the hydrogen- and helium-burning shells to extinguish and the luminosity of the star to drop abruptly, revealing a central hot object (the old red giant's degenerate C-O core or ONeMg core in the case of more massive stars) that will cool to become a white dwarf surrounded by a thin layer of residual H and He, which is the stage prior to the formation of a neutron star or a black hole [11].

2.7.9. Planetary nebulae

When the white dwarf forms, the shell of gas around it, the **planetary nebula** —which used to be the white dwarf's progenitor star's envelope—, expands until its material is completely dissipated into the interstellar medium after about only 50000 years, thus forming the ideal conditions for dust to gravitationally collapse and form stars again. This poetic, cyclic process of star formation, death and rebirth is evident in the variations in composition between stars because, when the dying star's matter is given back to the interstellar medium, it has already been enriched with heavier elements that were produced through the various sequences of nuclear reactions governing a star's life and, as a result, when the next generation of stars is formed, it possesses higher concentrations of these heavy elements than did its ancestors, thus giving astronomers a way to measure not only stars' age, but the whole universe's age [11].

2.8. The Red Clump

The clump of red giants (commonly known as the Red Clump, RC) is an outstanding feature in the color-magnitude diagrams of intermediate-age star clusters and nearby

galaxies that is made mostly of low-mass stars in the stage of core He-burning, which appear red and very close to the first-ascent RGB due to their big convective envelopes, as can be seen in figure 2. Those big convective envelopes result from either a moderately high metallicity or, more generally, a significant amount of mass (a few $0.1 M_{\odot}$) above the H-burning shell. Low-mass stars without such a buffer of mass or extremely low metallicities will burn helium at higher effective temperatures, thus defining more extended features that define what is commonly referred to as the Horizontal Branch (HB), shown in figure 15.

Although the RC is sometimes called "the red extremity of the HB", RC stars are far more abundant than HB stars and it is estimated that they actually make about 1/3 of all red giants. This lack of recognition may be due to the fact that, even despite their ubiquity, RC stars were virtually unknown until the 1970s, contrary to HB stars, which have been frequently studied in globular clusters for more than a century [14].

2.8.1. Characteristics and origin of the RC

RC stars are low-mass stars in their stage of central convective He-burning, with a surrounding radiative H-burning shell and an H-rich convective envelope. The entire core-helium-burning (CHeB) evolution consists in the progressive conversion of the He in the core into C and O, together with a moderate migration of the H-burning shell. During the CHeB evolution, most of the luminosity is provided only by the H- and He-burning regions, with neutrino losses being negligible and the gravitational luminosity being relevant only at the very end, as the He-burning region migrates from the He-exhausted core into a shell and the star enters into the E-AGB [14].

The main factors that determine CHeB stars' luminosity are the core and the envelope masses, which are set by the evolution previous to beginning the He-burning phase (i.e., the ZACHeB phase). The core mass at helium ignition (M_{core}^0) presents a plateau for all low-mass stars (as is shown in figure 16), which develop electron-degenerate cores after the MS. Since these stars have greater pressure support and their centers are cooled by high electron conductivity, their He ignition is delayed and they follow the evolution along the RGB (shown in figure 14), phase in which their cores accrete by-products from the H-burning shell until reaching a mass of about $0.47 M_{\odot}$, point at which the He ignites in a flash (the **helium flash** of section 2.7.4), leading to the progressive lifting of core degeneracy during less than 2 million years. The existence of an initial mass that a star is required to have to avoid He degeneracy (M_{HeF} , which is estimated to be close to $2.5 M_{\odot}$ [14]) and thus avoid going through the abrupt helium flash is then what explains why low-mass CHeB stars appear as a clump in the color-magnitude diagrams: since their mass is less than M_{HeF} , their core masses M_{core}^0 are very similar (as seen in figure 16) and

thus their differences in luminosity and effective temperature are limited to those caused by their different envelope masses and compositions [14].

On the other hand, in the case of stars with initial masses $\geq M_{HeF}$, the ZACHeB luminosity monotonically increases with the stellar mass (as shown in figure 16), with the consequence of the formation of two new subgroups: the secondary red clump (SRC, composed by CHeB stars with masses between M_{HeF} and $M_{HeF} + 0.3M_\odot$ and fainter than those of the classical RC) and the vertical structure (VS, composed by CHeB stars with masses greater than $M_{HeF} + 0.3M_\odot$ and brighter than those of the classical RC). Although caused by stars with a distinct evolutionary history, these 2 substructures are located close enough to the main RC to be inextricably associated with it and, in many cases, observationally indistinguishable from it [14]; for this reason, the distinction between the RC's substructures is out of the scope of this dissertation and thus the RC will be treated as a whole in the following sections.

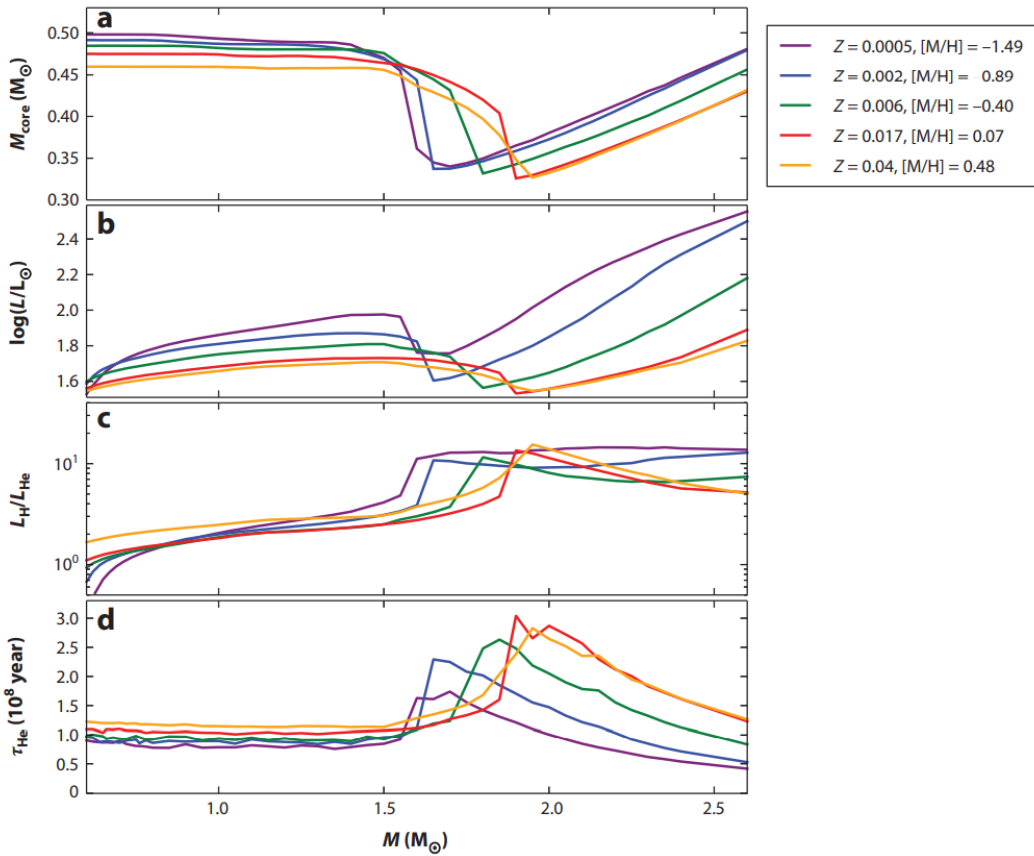


Figure 16: Some crucial parameters at the beginning of the core helium-burning (CHeB) lifetime as a function of mass and metallicity, for the entire mass interval relevant for the definition of the Red Clump. Panels show (a) the H-exhausted core mass M_{core} , (b) the total stellar luminosity, (c) the ratio between the luminosities of the H-burning shell and the He-burning core and (d) the total CHeB lifetimes, τ_{He} . Image taken from [14].

2.8.2. The RC in the HR diagram

Soon after the success of Hipparcos mission, astronomers were able to make color-magnitude diagrams from the high-precision parallaxes of all stars within a 100 pc radius from Earth and, since then, it has been estimated [14] that around 508 stars from Hipparcos' catalogue are RC stars, all contained within the ranges $M_V = [0.5, 1.5]$ and $B - V = [0.9, 1.25]$, accounting for approximately 31% of the red giants within that catalogue. Figure 17 shows three different versions of the Hipparcos-derived color-magnitude diagrams, being the $(B - V, M_V)$ version the most reliable one due to the uniformity and accuracy of its photometry.

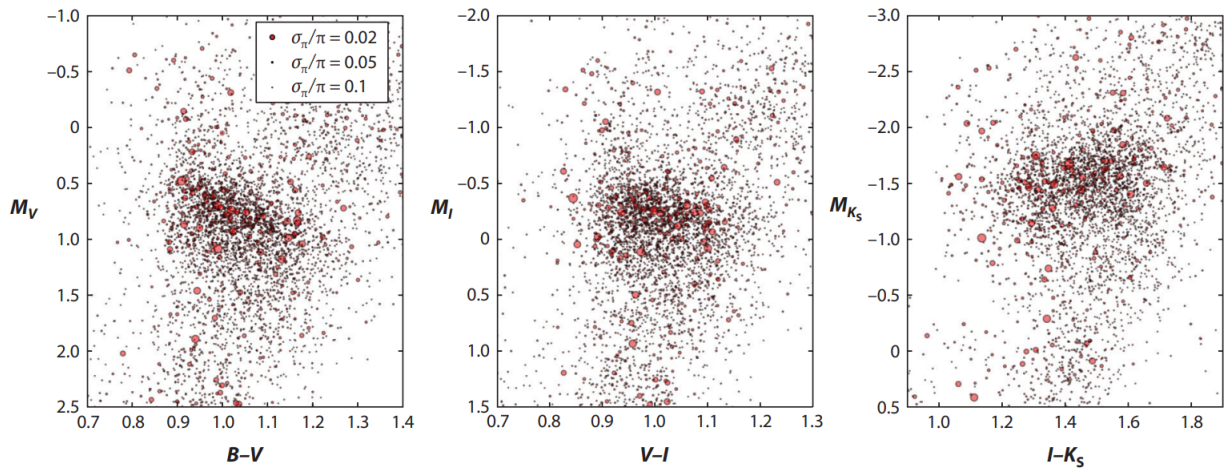


Figure 17: *The Solar Neighborhood's RC revealed by Hipparcos in a few color-magnitude diagrams. Only stars with parallax errors $\frac{\sigma_\pi}{\pi}$ smaller than 10% are plotted. Image taken from [14].*

2.8.3. Why the Red Clump?

What is the importance of Red Clump stars? Why do astronomers study this zone in the HR diagram? The answer to these questions falls on the ubiquity of RC stars and their intrinsic properties, which make the RC stand out clearly in the color-magnitude diagrams of clusters or galaxies, making it a useful distance indicator. There exists a series of "red clump methods" in which candidate RC stars are used to investigate and measure stellar extinctions, distances, chemistry and kinematics in many nearby galaxies and, in the case of the Milky Way and the Magellanic Clouds, RC methods are even the primary methods to perform 3D mapping of stars and interstellar dust [14]. In this way, it is this growing importance and appreciation in RC methods what motivates astronomers to find ways to quickly identify RC stars, as is the case with this dissertation.

2.9. Previous works on the subject

Stellar spectroscopy has provided useful information on the physical properties of stars such as effective temperature, metallicity and surface gravity for decades, but those photospheric characteristics have often been hampered by systematic uncertainties. A few years ago, the APOKASC project —which is the combination of APOGEE and Kepler projects— for red giants revealed a puzzling offset between the surface gravities $\log(g)$ determined spectroscopically and those determined using asteroseismology, which studies the oscillations in stars and is thus largely dependent on the stellar evolutionary status. This offset is plotted in figure 18 as a function of the stellar mass and shows that, for some reason, the offset in $\log(g)$ depends on whether the star is at the core He-burning phase (RC stars) or at the H shell-burning phase (RGB stars), what turns out to be a baffling and unexpected result since, according to classical low-mass stellar evolution (as was shown in section 2.7), it is not expected that the photosphere is influenced by ongoing internal nucleosynthesis.

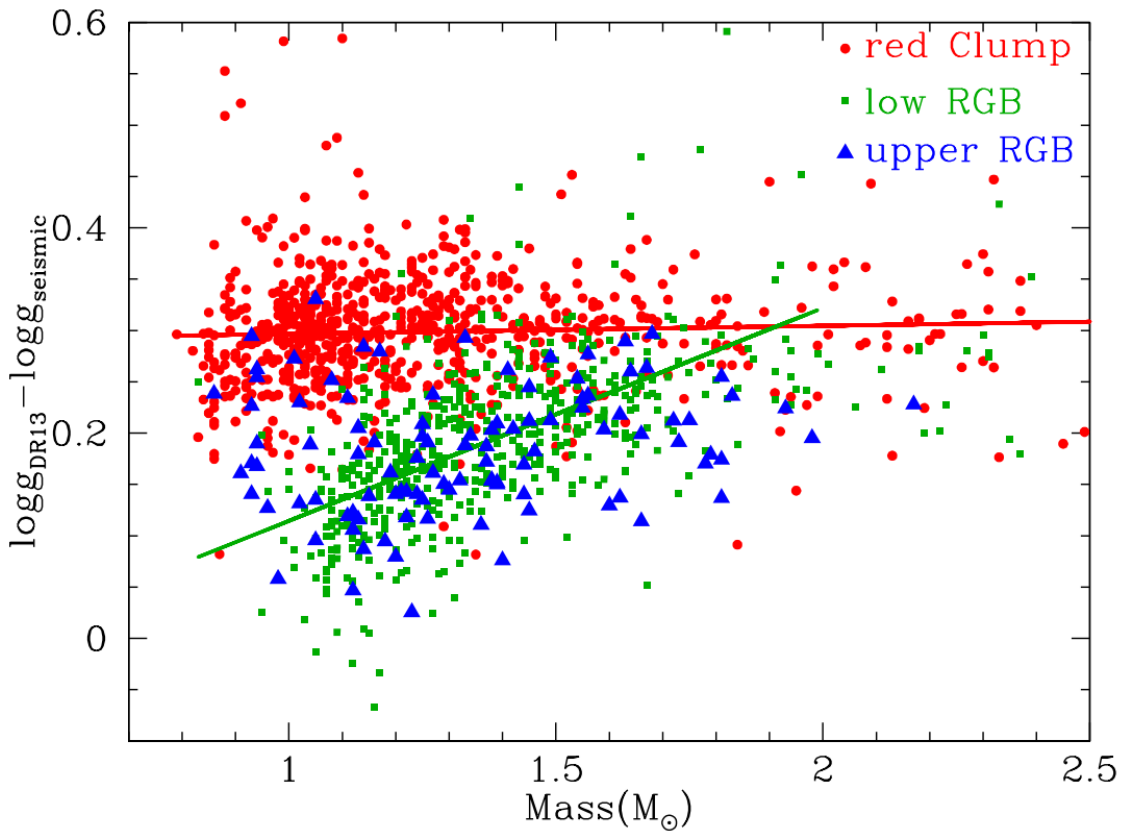


Figure 18: Difference between the $\log(g)$ derived from APOGEE DR13 and the $\log(g)$ obtained by asteroseismology as a function of stellar mass. Image taken from [5].

In 2016, [5] identified that, if this problematic $\log(g)$ phenomenon turns out to be a photospheric effect, understanding it actually represents an extraordinary chance to

unambiguously distinguish between the stellar evolutionary status of RC and RGB stars from spectroscopy alone, something that has long been sought in astronomy. With that in mind, [5] tried to narrow down the spectroscopic origin of this effect by constraining and testing unexplored spectroscopic variables such as abundances and isotopic ratios like $^{12}\text{C}/^{13}\text{C}$, but the only conclusion they could get was that ^{13}C is probably not the missing spectroscopic factor that explains the $\log(g)$ problem, but some CN-cycling related phenomenon instead.

Some years later, while studying the differential redshift of Ti I lines in K-type stars to better understand granulation signatures in stellar spectra, [7] found that, at least within their sample of 11 stars, RC stars have stronger CN I lines than RGB stars, as deduced from the EWs measured for those lines. If that were the general case, then the CN-cycling theory proposed by [5] could be on the right path and thus the EW of CN lines could become the parameter that would allow to distinguish red giants' evolutionary status from spectroscopy alone; that is, in short, the main motivation for this dissertation.

3. Observational data

In this section, the process of how RC and RGB stars were selected and of how their spectra were obtained is going to be explained. For this dissertation, a total of 31 stars were obtained from searches in Hipparcos' catalogue [15] and in the UVES-POP [16] and PEPSI [17] online databases, as will be explained below.

3.1. Selecting RC stars from Hipparcos' catalogue

3.1.1. Choosing the star catalogue

Following the steps of [14], the chosen catalogue of stars to work with was Floor van Leeuwen's revised version of Hipparcos [15], which has more reliable parallaxes than the original Hipparcos catalogue and was accessed through the VizieR online catalogue service provided by the Centre de données astronomiques de Strasbourg [18]. The reason for using this catalogue was that, although more recent catalogues such as GAIA's have higher apparent visual magnitude (V) stars and more accurate measurements for parallaxes, that did not really matter in this case since what was been looked for were spectra of stars in the RC of the HR diagram and those can usually only be found for the closest stars, given that their closeness (less V) guarantees better-quality spectra. Moreover, considering that Hipparcos is a pioneering work and that it uses the classical $B - V$ index, the cross-identification of stars turns out to be easier.

3.1.2. First reduction of data: the negative parallax filter

Since the calculation of the absolute visual magnitudes of the stars (M_V) is absolutely necessary in order to be able to locate them on the HR diagram, the first reduction of data consisted of filtering the stars with parallaxes less than or equal to zero, since that leads to an error in equation 2.2 and thus also in equation 2.5. After applying this filter, the 117955 stars in the revised Hipparcos catalogue could be reduced to 113942 stars, which together form a HR diagram pretty similar to the one already shown in figure 1.

3.1.3. Second reduction of data: the B-V color index filter

The following step was to apply the $B - V$ color index filter with the objective of eliminating the stars that were not located within the $B - V$ range of the RC of the HR diagram, which was considered to be $B - V = [0.9, 1.25]$, as could be deduced from [14] and figure 17. As a result, the sample could further be reduced to 25714 stars.

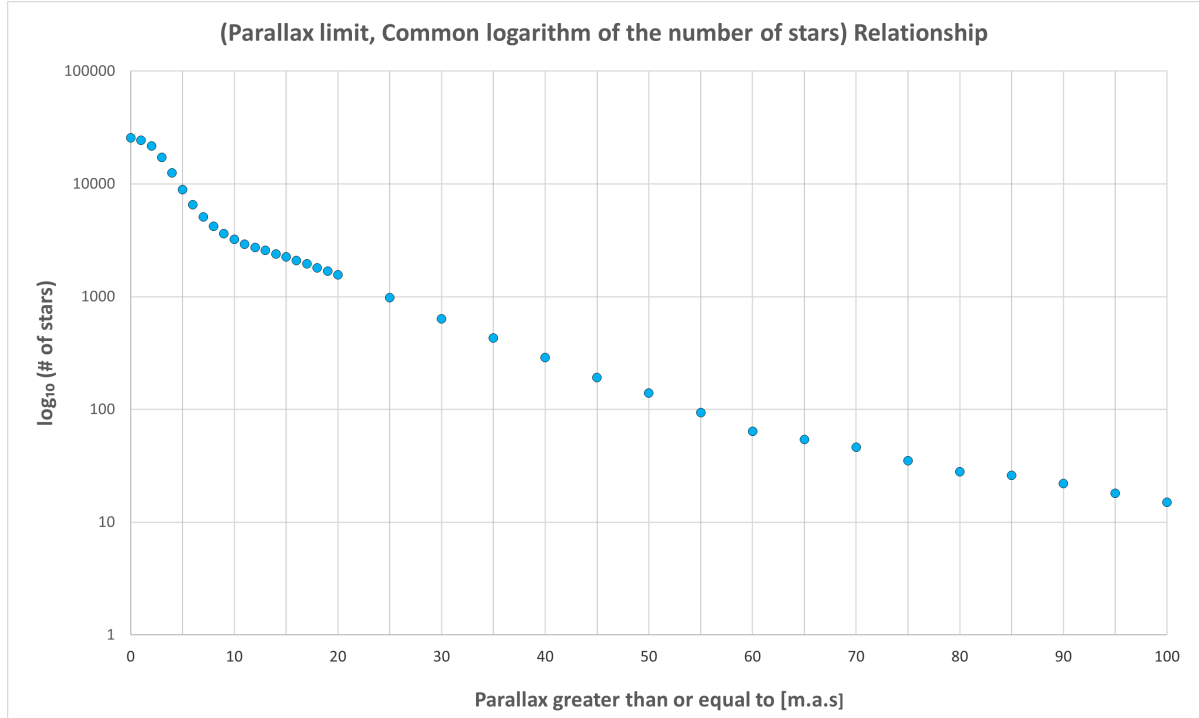


Figure 19: *Logarithmic relationship between the number of stars and their parallaxes. An apparent break of the relationship appears at $plx = 10$ m.a.s.*

3.1.4. Third reduction of data: the average partition error filter

Next, a statistical analysis was carried out with the aim of finding an appropriate range to filter the noise out. Figure 19 shows that there is a logarithmic relationship between the parallax and the number of stars, what means that, as is expected, the number of stars increases exponentially with distance. Nonetheless, this relationship apparently breaks at $plx = 10$ m.a.s, what could actually mean that, from that point onward, Hipparcos' catalogue starts having less accurate data. To further confirm this idea, the distances to the stars were calculated using equation 2.2 and their partition error was calculated as is explained in appendix A. As table 20 shows, the mean partition error in the distances associated to parallaxes of less than 10 m.a.s is much greater than that in the distances associated to parallaxes greater than or equal to that value, what confirms $plx = 10$ m.a.s

as a suitable point to cut the data. Now, the result of the filter was a further reduction to 3219 stars.

Parallax range [m.a.s]	Average partition error in distance [%]	Average partition group error [%]
>100	2,5	2,4
[90, 100]	0,6	
[80, 90]	0,7	
[70, 80]	0,9	
[60, 70]	3,3	
[50, 60]	3,5	
[40, 50]	3,6	
[30, 40]	4	
[20, 30]	7	8,4
[11, 20]	9,5	
[10, 11]	8,1	
[9, 10]	9	
[8, 9]	8,2	
[7, 8]	10,2	85,4
[6, 7]	11,5	
[5, 6]	14,6	
[4, 5]	19	
[3, 4]	26,2	
[2, 3]	40	
[1, 2]	71,7	
[0, 1]	490,3	

Figure 20: Average partition error for the distances associated with different parallax ranges. It can be appreciated how parallaxes of less than 10 m.a.s lead to very inaccurate results.

3.1.5. Forth reduction of data: the absolute visual magnitude filter

The final reduction consisted of filtering the data to fit the M_V range that encloses the RC, which, according to [14] and figure 17, could be considered to be $M_V = [0.5, 1.5]$. With this, data could be further reduced to only 446 stars.

3.1.6. Limiting the wavelength range and looking for the spectra

Finally, the spectra of the 446 candidate stars were searched in the UVES-POP database [16] but the only useful spectra found were those of the 8 stars showed in figure 23 since, following the steps of [7], the wavelength range [7400 Å, 7500 Å] was chosen because it is a short range (what helps to avoid wavelength-dependent line-depth variations) with a great abundance of CN I lines that is located towards longer wavelengths, what reduces the risk of blends due to the diminished density of absorption lines and also facilitates the work due to the absence of TiO I lines, as can be deduced from figure 12.

Considering that the found spectra of the RC stars are pretty similar to each other, 2 of them are going to be shown below (figures 21 and 22) so that the reader can appreciate that their similarity is so great that it is even possible to locate the same spectral lines with the naked eye.

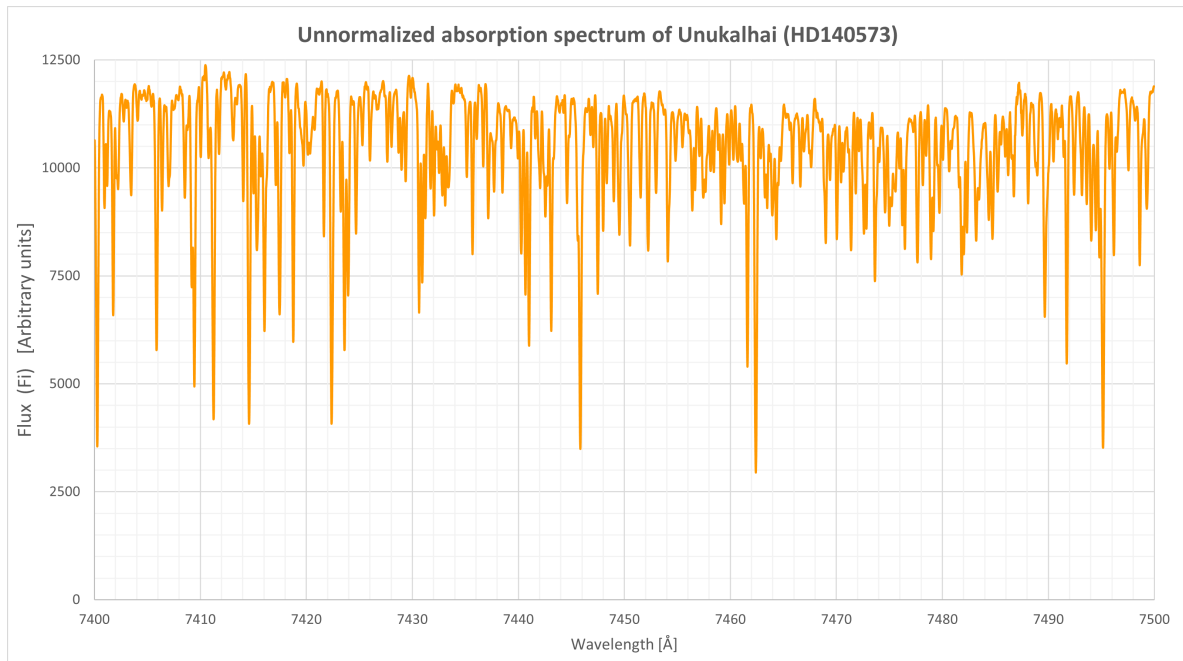


Figure 21: *Unnormalized absorption spectrum of RC star Unukalhai.*

3.2. Picking stars directly from UVES-POP

While looking for RC stars in UVES-POP library, it was found that UVES-POP can actually give a full list of its library's stars (which are around 300 [16]) with their Henry Draper Catalogue number and their luminosity and spectral classifications within the Morgan-Keenan system, what made the search for stars much more easier since now

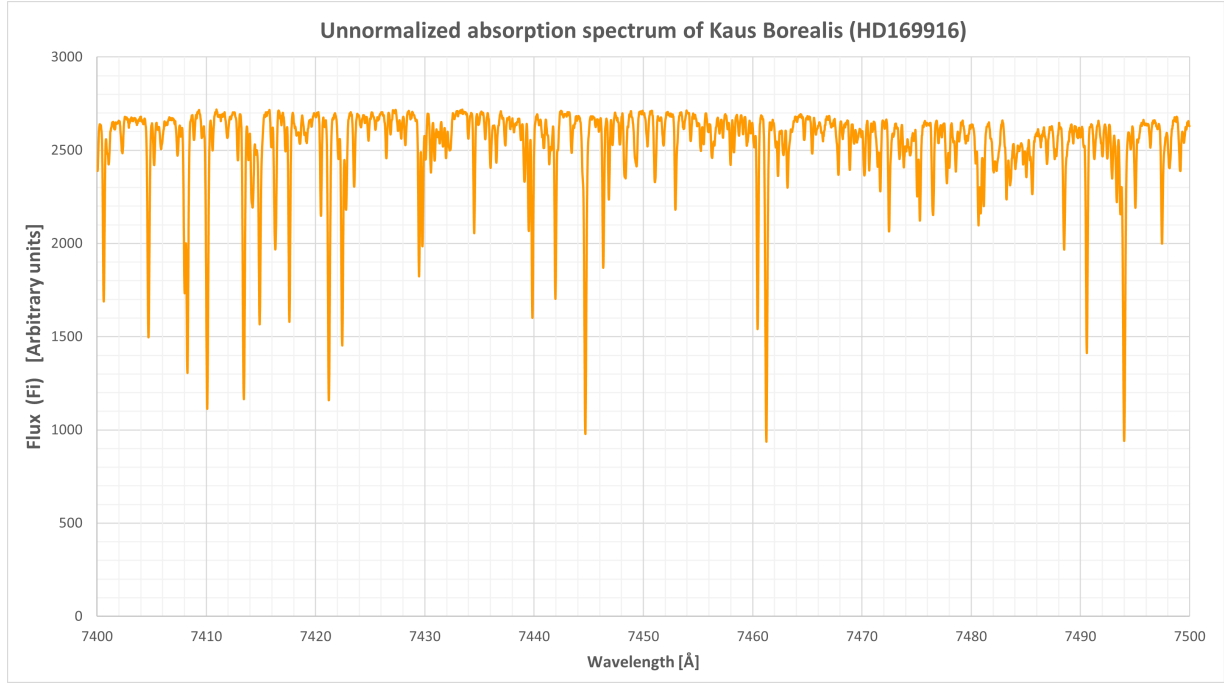


Figure 22: *Unnormalized absorption spectrum of RC star Kaus Borealis.*

it was not necessary to look for RGB stars in Hipparcos' catalogue and then look for their spectra in online libraries such as UVES-POP's. After searching for the B and V magnitudes of UVES-POP's stars in SIMBAD database [19], their B-V index and absolute visual magnitudes M_V could be computed, thus allowing to locate them in the HR diagram shown in figure 23.

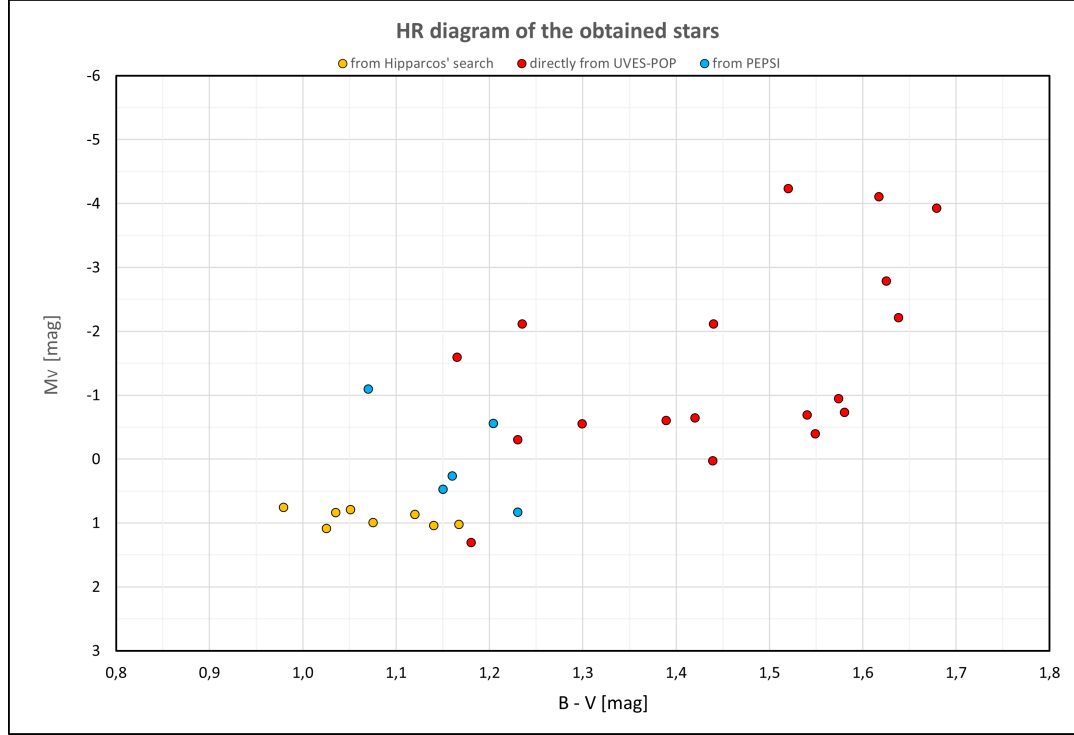


Figure 23: *HR diagram showing the origin of the spectra of the studied stars.*

With this, 18 stars within the desired $B - V$ and M_V ranges were added to this dissertation's catalogue, hence reaching 26 stars until this point. Below are shown the spectra of 2 UVES-POP's RGB stars so that the reader notes that it is possible to identify the same spectral lines in them due to their similarity, just as it was possible for RC stars.

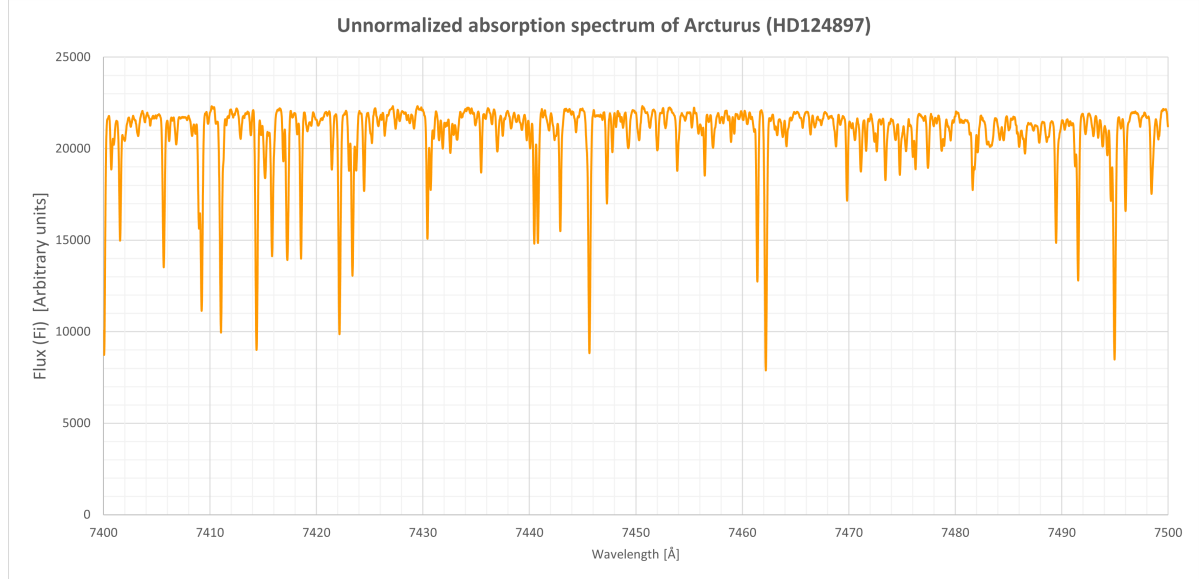


Figure 24: *Unnormalized absorption spectrum of RGB star Arcturus.*

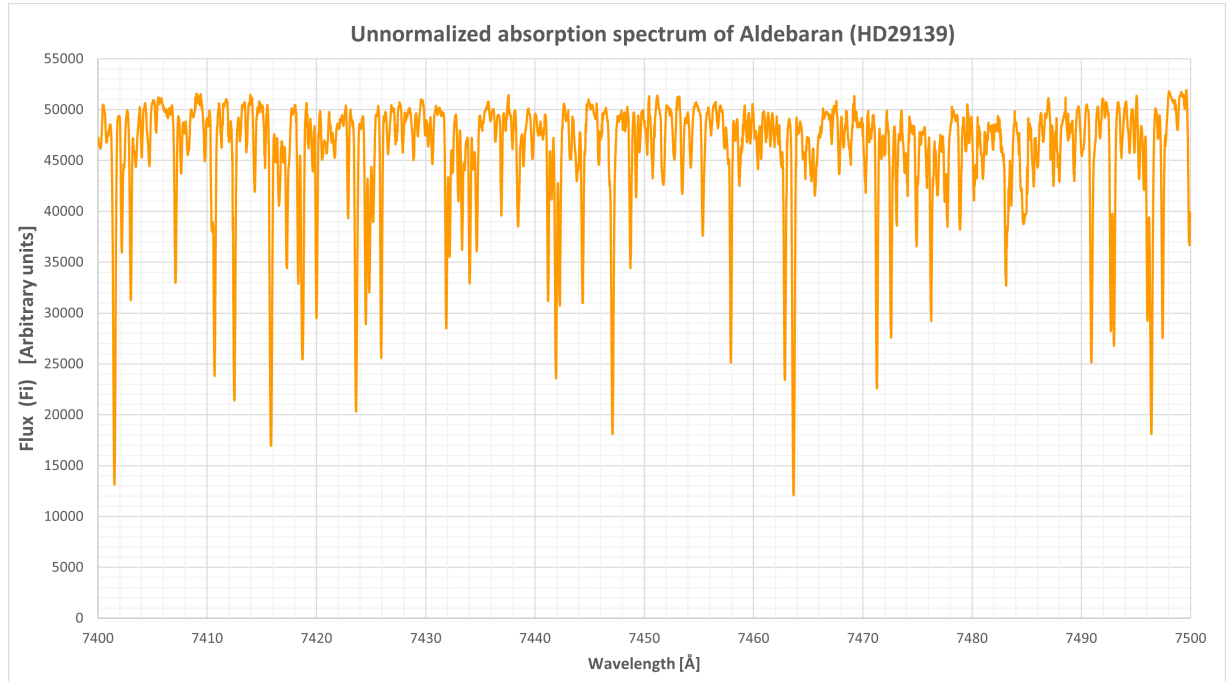


Figure 25: *Unnormalized absorption spectrum of RGB star Aldebaran.*

3.3. Visualizing PEPSI's stars

The hunt for more RGB and RC stars continued unsuccessfully in other online libraries. The libraries of ELODIE and SOPHIE spectrographs and of the European Southern Observatory (ESO) gave the spectra of many stars within the desired M_V and $B - V$ limits, but none of them showed the desired [7400 Å, 7500 Å] wavelength range. The only library where more stars could be found was that of the Potsdam Echelle Polarimetric and Spectroscopic Instrument (PEPSI^[17]), but another problem arose immediately: it was possible to visualize the spectra with PEPSI's spectrum viewer (shown in figure 26), but not to access to their flux and wavelength data, thus making impossible the use of equation 2.16 to find the spectral lines' EWs. In the end, the obstacle was overcome by calculating the EWs by means of the visual method explained in section 6, thus allowing to add 5 more stars to this dissertation's catalogue, which is fully shown in tables 76 and 77.

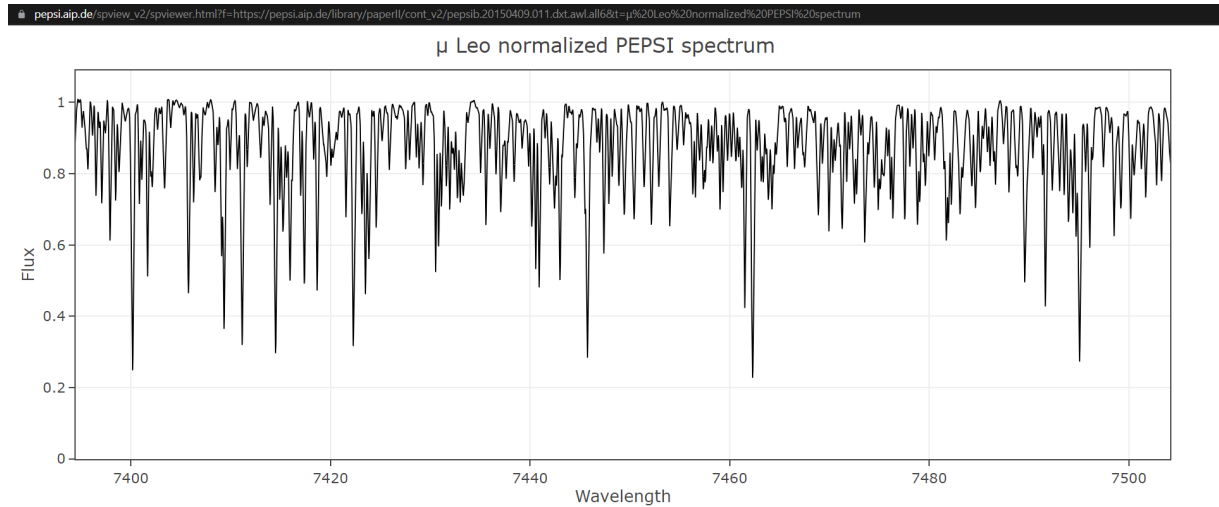


Figure 26: *Star μ Leonis' spectrum as viewed from PEPSI's spectrum viewer. The viewer can be accessed online and gives the possibility of zooming in to see the spectral lines more clearly.*

While figure 23 shows the origin of the spectra of the stars obtained in sections 3.1, 3.2 and 3.3, figure 27 shows HR diagram of the studied stars but now showing their evolutionary state, which was assigned to them after an extensive research both in the VizieR catalogues^[18] and in the scientific papers available in SIMBAD database^[19]. The classification, astrometric quantities and sources used to know the stars' evolutionary status are presented in tables 76 and 77 of appendix B.

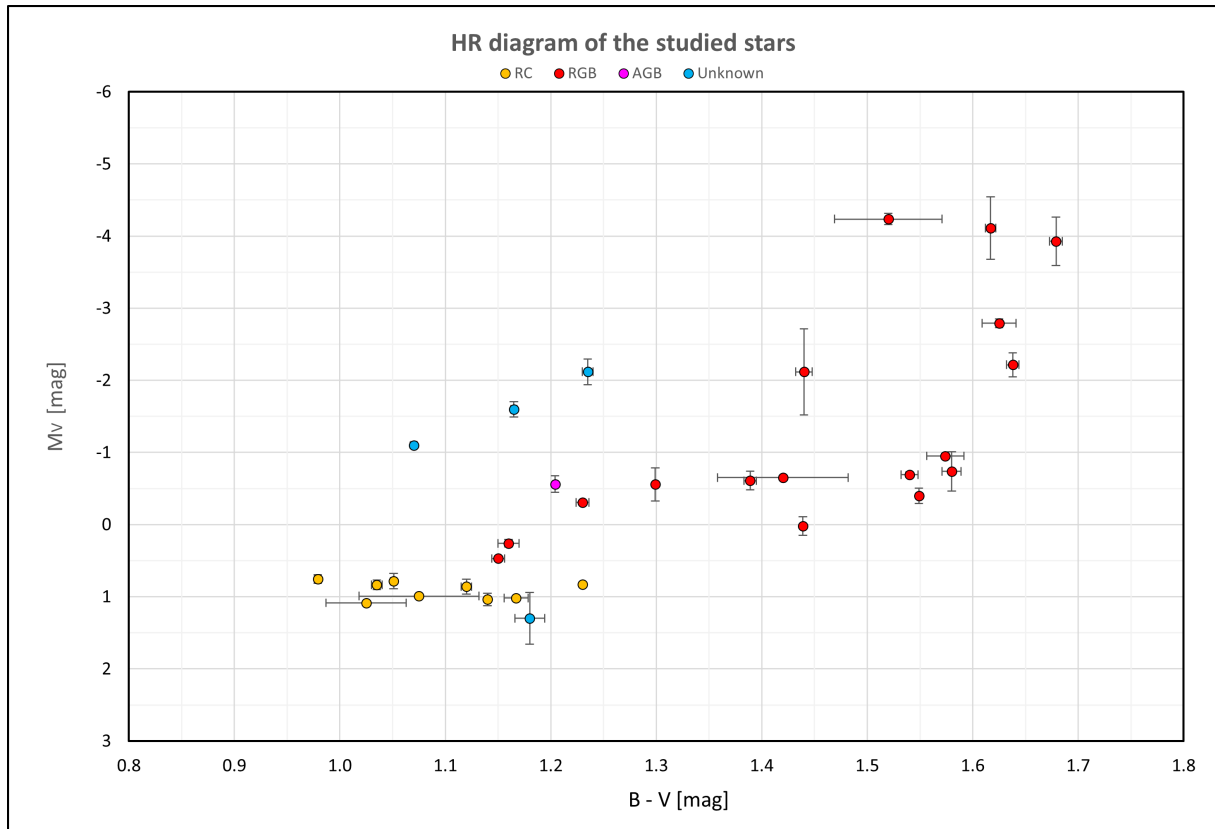


Figure 27: *HR diagram showing the evolutionary state of the studied stars as found in literature.*

4. Normalizing the spectra

Most of the stellar absorption spectra used in this dissertation were found in UVES-POP library [16] without being normalized, with arbitrary flux units. Although that is not a crucial problem that prevents the calculation of the EWs of the spectral lines, it is a not-so-desirable condition since data visualization, analysis and comparison become more difficult and cumbersome. In consequence, it was decided to normalize all the stellar absorption spectra as will be shown below for the specific case of RC star Unukalhai.

4.1. Plotting the original spectrum

The first step is to plot the original spectrum from the wavelength (λ_i) and unnormalized flux (F_i) data acquired from the online libraries. In the case of Unukalhai, UVES-POP library gives the spectrum shown in figure 21, where it can be seen that the flux is originally given in arbitrary units within the range [0, 12500].

4.2. Calculating the maximizing function

The second step is to create a maximizing function to delimit the upper part of the spectrum. Since the original spectrum obtained from the libraries only gives the unnormalized flux as a function of wavelength (i.e., they give an unnormalized flux F_i for each wavelength λ_i , such that $F_i = F_{(\lambda_i)}$), the maximized flux M_i for each λ_i was found with the function

$$M_i = \text{MAX}(F_{i-100}, F_{i-99}, \dots, F_{i+99}, F_{i+100}), \quad (4.1)$$

what means that the M_i corresponding to each λ_i is the maximum of 201 unnormalized flux points, going from 100 steps behind the current F_i to 100 steps after it. In the case of Unukalhai, this gives the maximizing function shown in figure 28, in which the upper part of the spectrum was zoomed in so that the details of the maximizing function can be seen.

4.3. Averaging the maximized flux values

The third step is to average the maximized flux so that the profile of the upper part of the spectrum is better delimited. To do this, the average maximized flux A_i corresponding

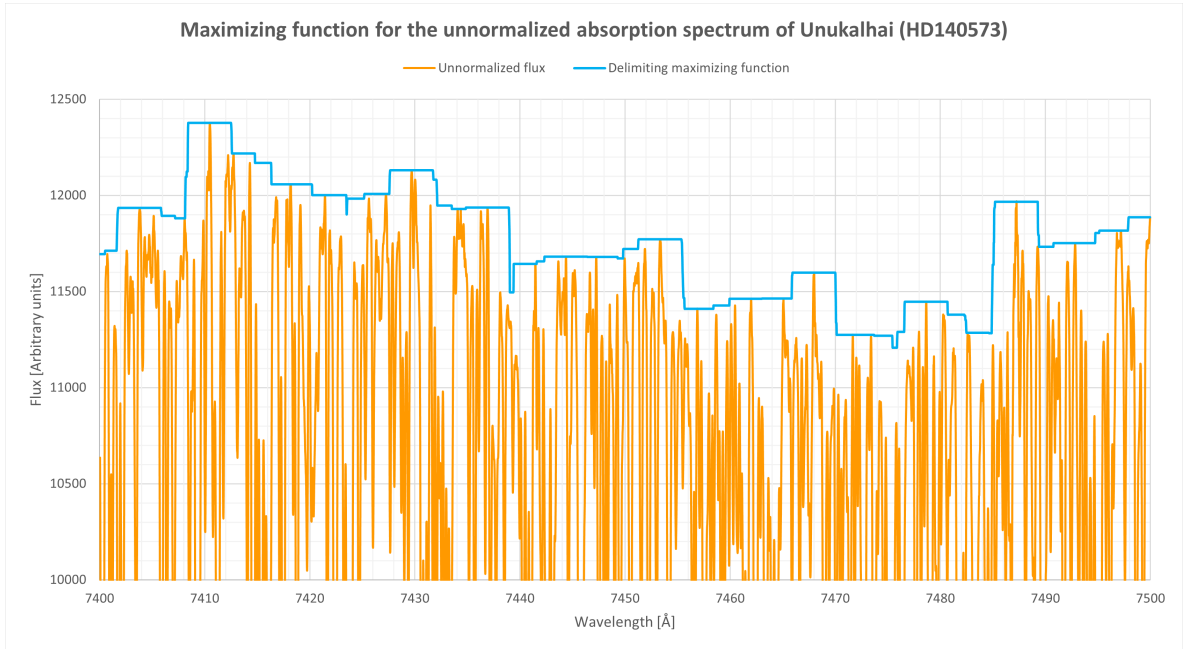


Figure 28: Maximizing function for the unnormalized absorption spectrum of star Unukalhai.

to a wavelength λ_i can be calculated with the equation

$$A_i = \left[\sum_{j=i}^{j=i+200} \frac{M_{j-100}}{201} \right] + b_{Noise}, \quad (4.2)$$

where M_{j-100} is the maximized flux defined in equation 4.1. The first term on the right hand side of the equation is the average of 201 maximized flux values (from the point λ_{i-100} to the point λ_{i+100}) and b_{Noise} is a constant required to eliminate some noise from the spectrum, as can be seen in figure 29 for the case of Unukalhai.

4.4. Obtaining the normalized spectrum

Finally, the normalized flux N_i for each wavelength λ_i is obtained with the relationship

$$N_i = \frac{F_i}{A_i}, \quad (4.3)$$

where F_i and A_i are defined as before. Coupling this with equations 4.1 and 4.2 leads to the final expression to normalize the spectrum:

$$N_i = \frac{F_i}{\left[\sum_{j=i}^{j=i+200} \frac{M_{j-100}}{201} \right] + b_{Noise}} \quad (4.4)$$

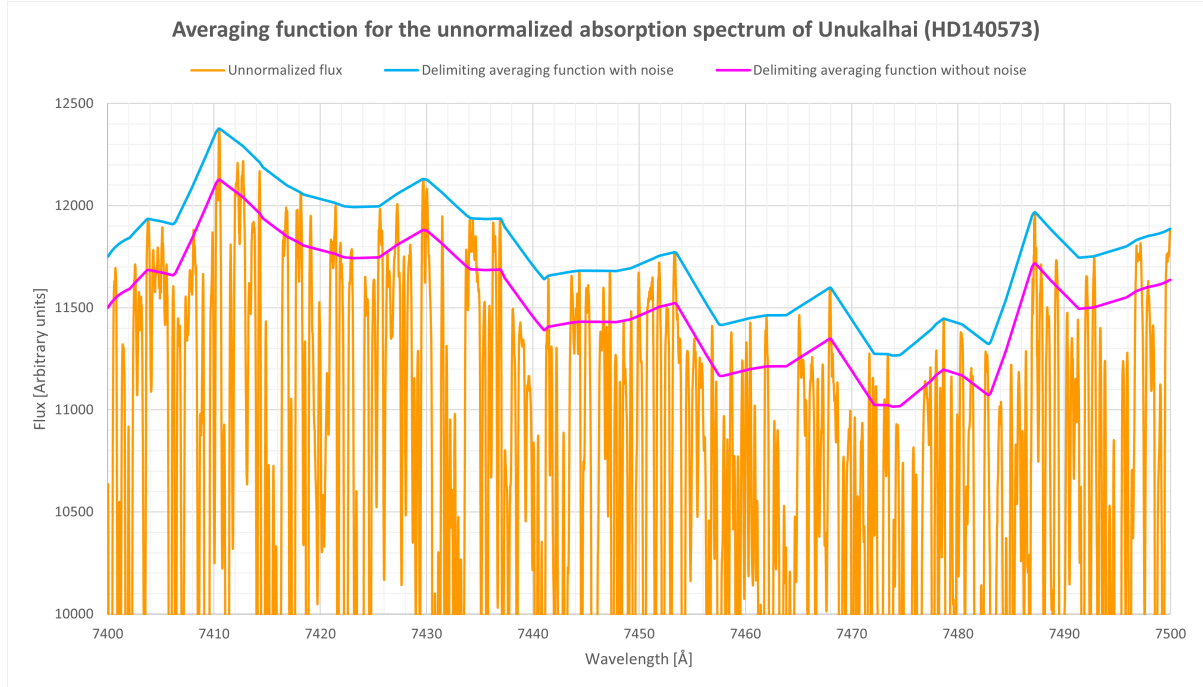


Figure 29: *Averaging function for the unnormalized absorption spectrum of star Unukalhai.* The blue function corresponds to equation 4.2 with $b_{Noise} = 0$, while the magenta function is also equation 4.2 but with $b_{Noise} = -250$, which is the useful value because it filters the tops of the peaks, which are considered to be instrumental noise.

$$\implies N_i = \frac{F_i}{\left[\sum_{j=i}^{j=i+200} \frac{\text{MAX}(F_{j-200}, F_{j-199}, \dots, F_{j-1}, F_j)}{201} \right] + b_{Noise}}. \quad (4.5)$$

The result is a spectrum whose normalized flux values N_i are contained mostly within the range $[0, 1]$ except for some peaks that can go up to 1.01 due to the uncertainty of the normalizing method and the instrumental noise, as can be seen in figure 30 for the case of Unukalhai.

4.5. Getting the inversed normalized spectrum

It is also possible to get the inversed normalized spectrum by simply applying the formula

$$I_i = 1 - N_i \quad (4.6)$$

$$= 1 - \frac{F_i}{\left[\sum_{j=i}^{j=i+200} \frac{\text{MAX}(F_{j-200}, F_{j-199}, \dots, F_{j-1}, F_j)}{201} \right] + b_{Noise}} \quad (4.7)$$

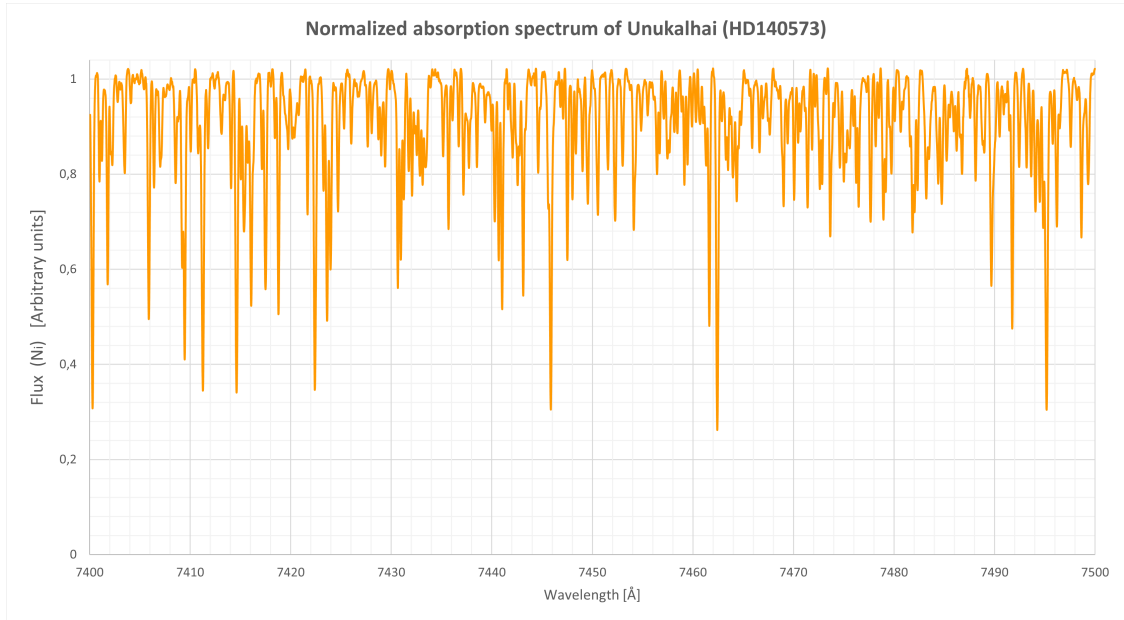


Figure 30: Normalized absorption spectrum of star *Unukalhai*.

$$\implies I_i = \frac{\left[\sum_{j=i}^{i+200} \frac{\text{MAX}(F_{j-200}, F_{j-199}, \dots, F_{j-1}, F_j)}{201} \right] + b_{\text{Noise}} - F_i}{\left[\sum_{j=i}^{i+200} \frac{\text{MAX}(F_{j-200}, F_{j-199}, \dots, F_{j-1}, F_j)}{201} \right] + b_{\text{Noise}}}. \quad (4.8)$$

Although this step could seem to be optional, that is actually not the case since, as equation 2.16 suggests, performing the calculation of the inverse normalized flux (equation 4.8) is necessary to find the EWs of the absorption spectral lines. Visually, the result is something similar to an emission spectrum, as can be seen in figure 31.

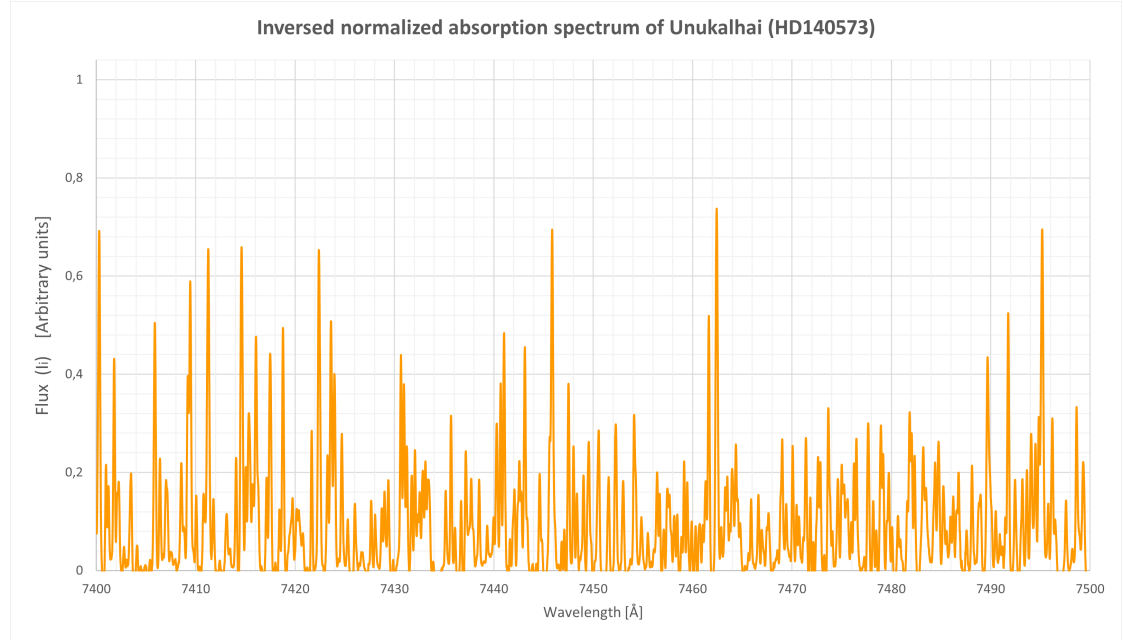


Figure 31: Inversed normalized absorption spectrum of star *Unukalhai*.

5. Selection of spectral lines

The process of how the absorption lines were selected and identified is going to be explained in this section. Absence of blends and line strength were the applied criteria when looking for the sample of lines and, since this dissertation desires to explore the relationship between iron, titanium and cyanide lines, other elements and molecules were excluded.

5.1. Looking for the spectral lines in a model star's spectrum

In order to be able to identify the absorption spectral lines in the spectra, a model absorption spectrum was requested from VALD-3 database [20] (using the option "Extract Stellar"), with the following parameters:

- **Starting wavelength:** 7400 Å(air)
- **Ending wavelength:** 7500 Å(air)
- **Detection threshold:** 0.002
- **Microturbulence:** 0 $\frac{km}{s}$
- T_{eff} : 4500 K
- $\log(g)$: 1 (g in cgs units)

As has been previously said, the wavelength range [7400 Å, 7500 Å] was chosen because it lies just where the photospheres of the studied stars absorb the most light (thus giving broader, clearer lines) and because it is the range where Fe I lines are clearest and where TiO I lines almost disappear, as can be inferred from equation 2.9 and figures 5 and 12. Additionally, the obtained theoretical line depths of the model spectrum are shown in figures 32 to 35, which now allow to choose the deepest and/or unblended lines.

5.2. Selected Ti I lines

The only reference for titanium ended up being Ti I 7440,5765 Å(as shown in table 36), for it is the only one that is not blended with another CN I, Fe I or another element's lines, as can be deduced from figures 32 to 35.

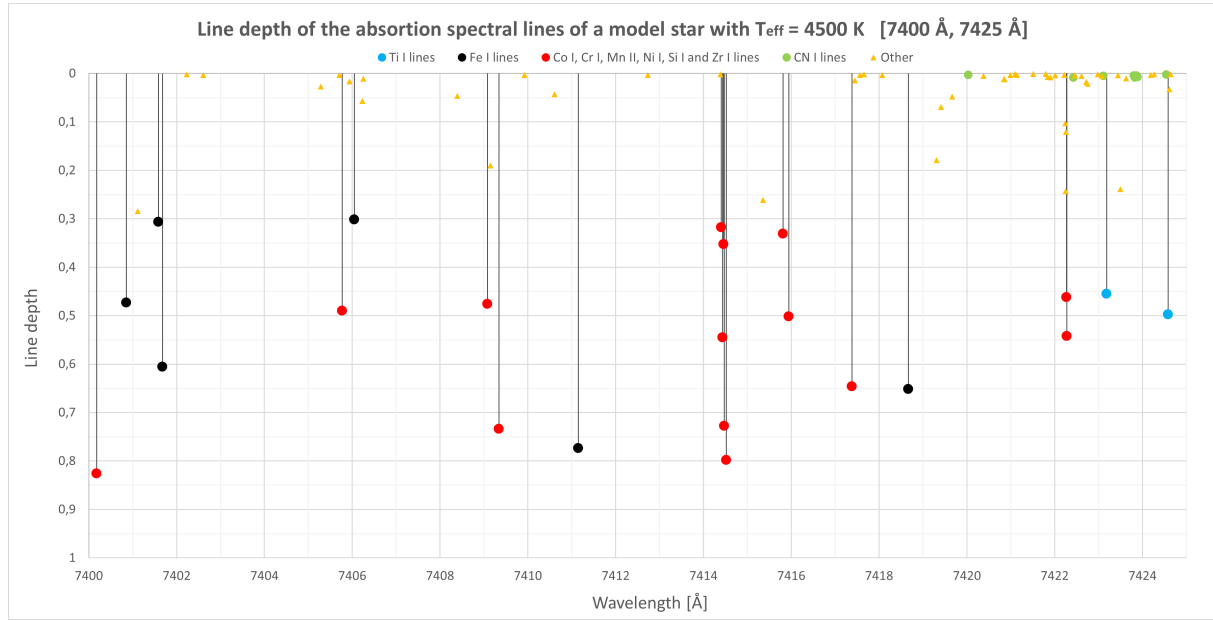


Figure 32: *Line depths of VALD-3's model absorption spectrum's lines within the wavelength range [7400 Å, 7425 Å].*

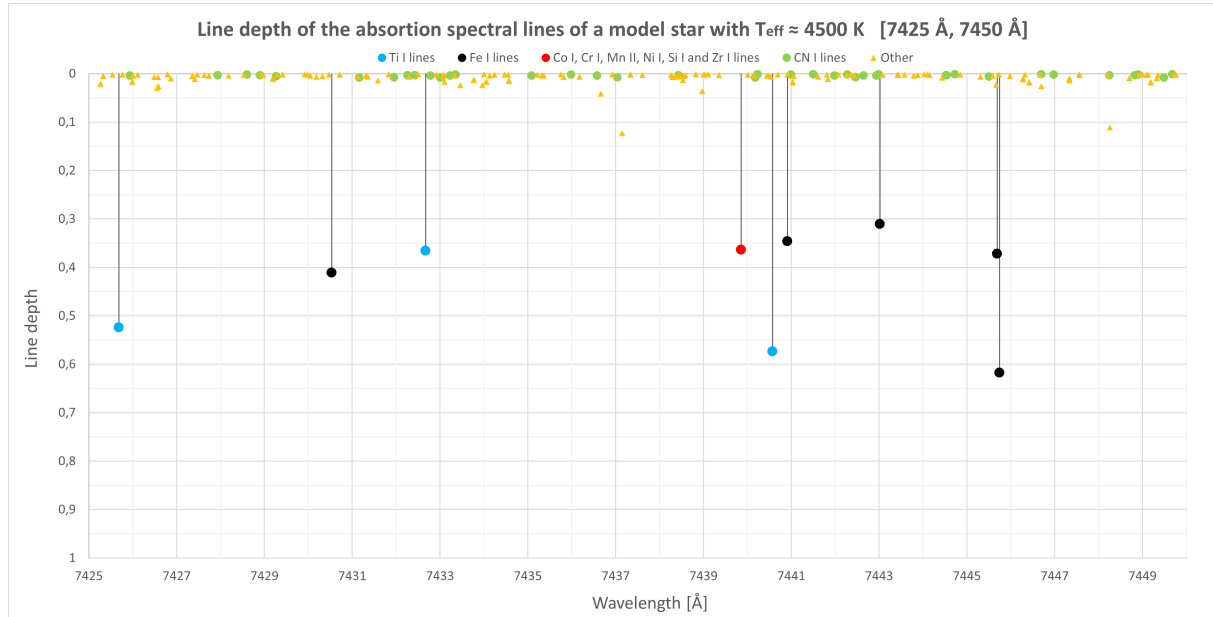


Figure 33: *Line depths of VALD-3's model absorption spectrum's lines within the wavelength range [7425 Å, 7450 Å].*

5.3. Selected Fe I lines

In the case of the Fe I lines, 11 of them satisfied the criteria (absence of blends and good-enough line depth), but only 4 of them —the ones shown in table 37— were studied, for they were considered to be not only the deepest ones but also very well-spaced along the wavelength range. This can again be easily deduced from figures 32 to 35.

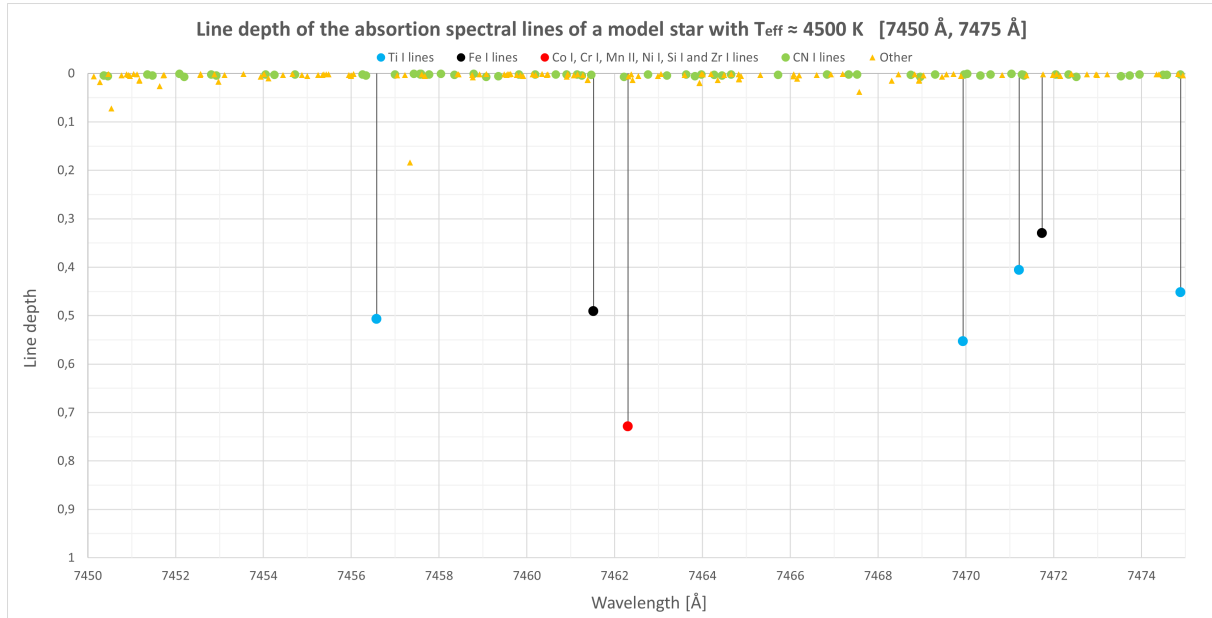


Figure 34: Line depths of VALD-3's model absorption spectrum's lines within the wavelength range [7450 Å, 7475 Å].

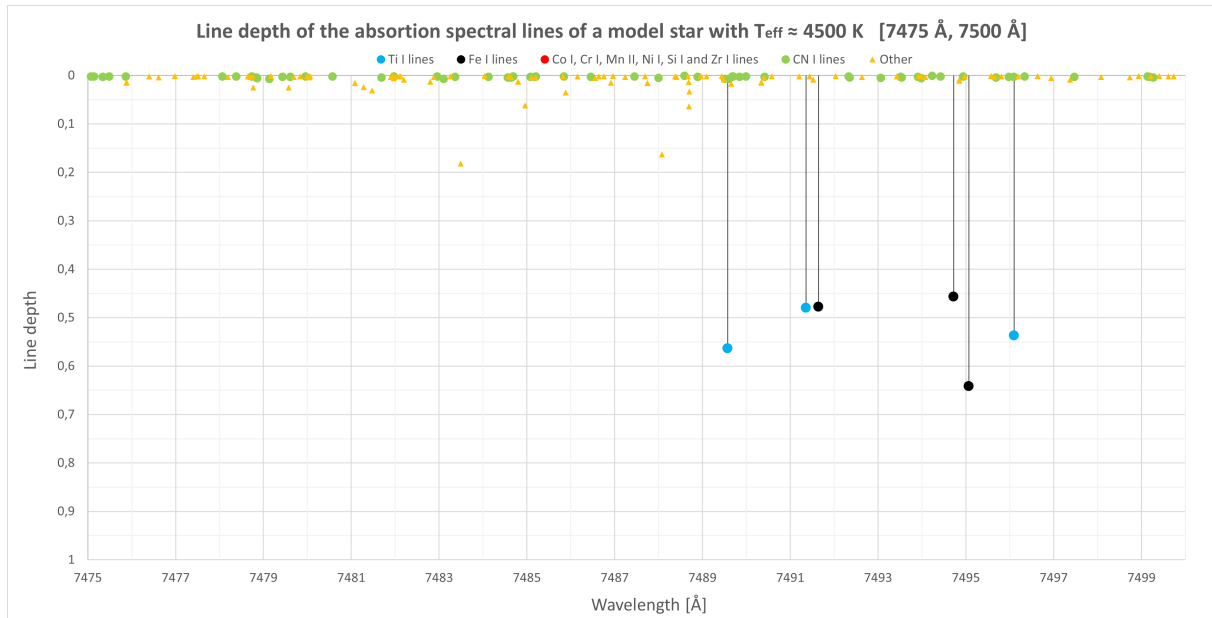


Figure 35: Line depths of VALD-3's model absorption spectrum's lines within the wavelength range [7475 Å, 7500 Å].

Species	λ (Air)	χ (eV)	$\log g f$
Ti I	7440,5765	2,2556	-0,86

Figure 36: List of studied Ti I lines. Data taken from [20].

5.4. Selected CN I lines

In the case of CN I lines, the process to find suitable spectral lines was not so simple since, as can be seen in figures 32 to 35, VALD-3's stellar model gave CN I and other

Species	λ (Air)	χ (eV)	$\log gf$
Fe I	7411,1544	4,2833	-0,299
Fe I	7445,7508	4,2562	-0,102
Fe I	7461,5206	2,5592	-3,58
Fe I	7495,0674	4,2204	0,052

Figure 37: List of studied Fe I lines. Data taken from [20].

molecules or element's lines a very short line depth, thus making it impossible to identify suitable lines visually; that does not mean that the star does not have CN I lines (or, at least, deep-enough ones), but rather that VALD-3's models still need to be improved to give more accurate line depths. With the above in mind, all of VALD-3 model's lines were plotted with a constant line depth of 1 in order to find unblended and deep-enough CN I lines, as can be appreciated in figures 39 and 40, where it becomes clear that most of the CN I lines had to be discarded for not being deep enough or being blended with other lines. Along the whole wavelength range [7400 Å, 7500 Å], the only 4 suitable CN I lines found were those of table 38, 3 of which could be identified by means of figures 39 and 40.

Species	λ (Air)	χ (eV)	$\log gf$
CN I	7448,2448	0,9557	-1,647
CN I	7451,3553	0,8046	-2,144
	7451,4725	0,7165	-1,858
CN I	7452,0863	0,7627	-2,289
	7452,1941	0,8252	-1,443
CN I	7488,0011	0,9612	-1,394

Figure 38: List of studied CN I lines. Data taken from [20].

One detail that the reader might have already noted is that in figures 39 and 40 there are actually 5 CN I lines instead of 3. That is actually true, but, considering that both pairs of adjoining lines come from the same CN I molecule, their EWs could be considered to have the same temperature dependence (as equations 2.17, 2.18 and 2.19 suggest) and they were thus considered to be a single line for practical purposes, since another blended, not so deep CN I lines would have to be used otherwise.

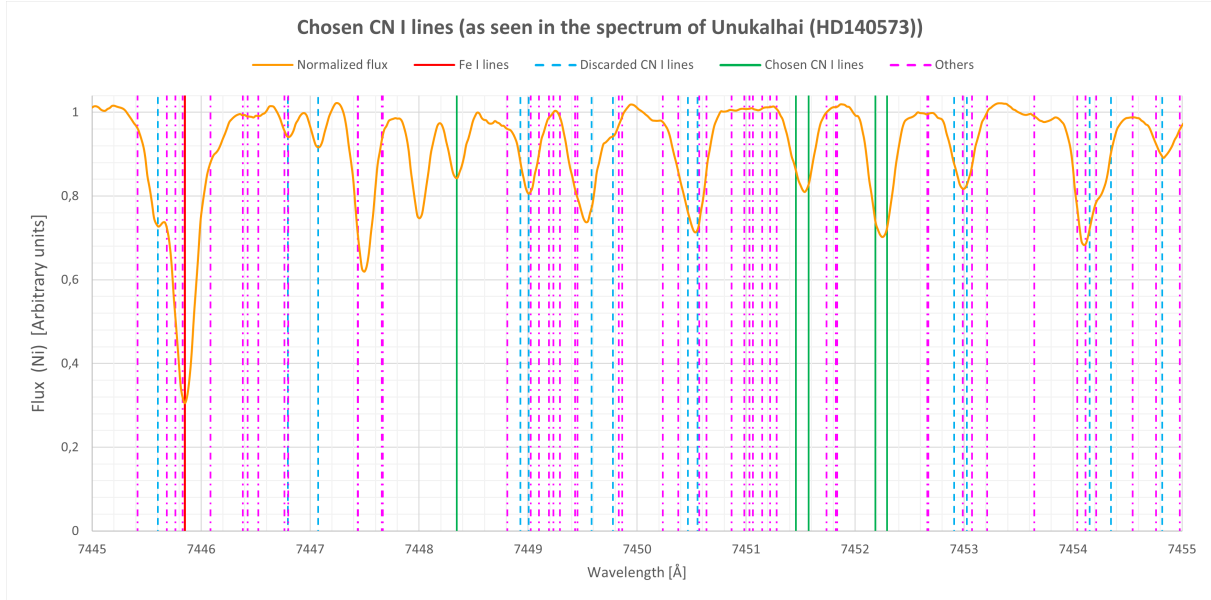


Figure 39: Illustration of how the CN I lines were selected, as seen in RC star Unukalhai's spectrum.

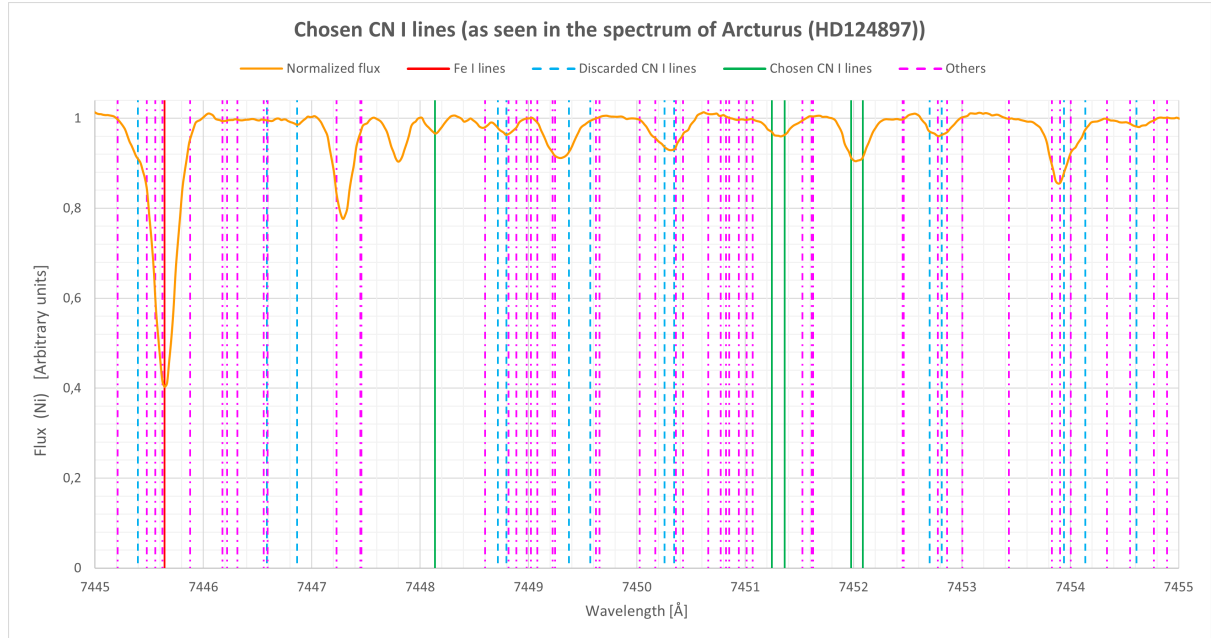


Figure 40: Illustration of how the CN I lines were selected, as seen in RGB star Arcturus' spectrum.

5.5. Visualization of the studied lines in the spectra

Lastly, the whole set of studied Ti I, Fe I and CN I spectral lines (tables 36, 37 and 38) can be seen plotted in figures 41 and 42, which show the normalized spectra of Unukalhai and Arcturus, respectively. Those figures show (and figures 39 and 40 show it even more clearly) that, having normalized the spectra and identified the unblended spectral lines, it

is now even possible to see with the naked eye —just by looking at the spectra— that RC stars like Unukalhai have stronger CN I lines, thus indicating that the proposed hypothesis exposed in [7] and at the beginning of this dissertation might be on the right track.

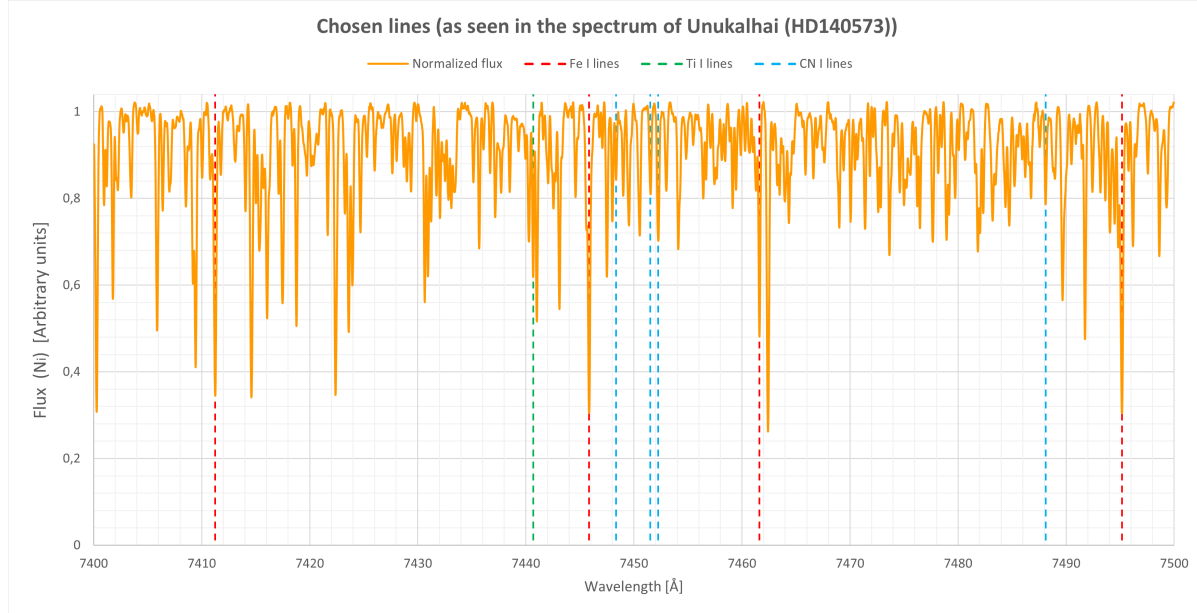


Figure 41: Total set of studied Fe I, Ti I and CN I lines plotted in RC star Unukalhai's spectrum.



Figure 42: Total set of studied Fe I, Ti I and CN I lines plotted in RGB star Arcturus spectrum.

6. Measuring the strength of the spectral lines

The mathematical equations used to model the spectral lines are going to be illustrated in this section, as well as the procedure used to compute their EWs, which was a direct method in the case of UVES-POP's stars and a visual method in the case of PEPSI's stars (since their spectral data could not be accessed).

6.1. Modeling the spectral lines

In order to compute the EWs of the spectral lines, the latter were considered to have a gaussian profile centered at the laboratory wavelengths given by VALD-3 database, what means that the inverses normalized absorption flux I_i and their corresponding wavelengths λ_i were assumed to be correlated by the equation

$$I_{(\lambda_i)} = I_i = \frac{1}{\sigma\sqrt{2\pi}} e^{-\frac{1}{2}\left(\frac{\lambda_i - \lambda_0}{\sigma}\right)^2}, \quad (6.1)$$

where σ is the standard deviation of the spectral line's inverses flux and λ_0 its expected value, which is the spectral line's wavelength given by VALD-3. Taking the natural logarithm on both sides leads to

$$\ln(I_i) = \ln \left[\frac{1}{\sigma\sqrt{2\pi}} e^{-\frac{1}{2}\left(\frac{\lambda_i - \lambda_0}{\sigma}\right)^2} \right] \quad (6.2)$$

$$= \ln \left(\frac{1}{\sigma\sqrt{2\pi}} \right) + \ln \left[e^{-\frac{1}{2}\left(\frac{\lambda_i - \lambda_0}{\sigma}\right)^2} \right] \quad (6.3)$$

$$= \ln \left(\frac{1}{\sigma\sqrt{2\pi}} \right) - \frac{1}{2} \left(\frac{\lambda_i - \lambda_0}{\sigma} \right)^2 \ln(e) \quad (6.4)$$

$$= \ln \left(\frac{1}{\sigma\sqrt{2\pi}} \right) - \frac{1}{2} \left[\frac{\lambda_i^2 - 2\lambda_i\lambda_0 + \lambda_0^2}{\sigma^2} \right] \quad (6.5)$$

$$= -\frac{1}{2\sigma^2} \lambda_i^2 + \frac{\lambda_0}{\sigma^2} \lambda_i + \left[-\frac{\lambda_0^2}{2\sigma^2} + \ln \left(\frac{1}{\sigma\sqrt{2\pi}} \right) \right], \quad (6.6)$$

where it is now useful to define the constants

$$a \equiv -\frac{1}{2\sigma^2} \quad (6.7)$$

$$b \equiv \frac{\lambda_0}{\sigma^2} \quad (6.8)$$

$$c \equiv \left[-\frac{\lambda_0^2}{2\sigma^2} + \ln\left(\frac{1}{\sigma\sqrt{2\pi}}\right) \right], \quad (6.9)$$

which now allow to easily identify a parabola of the form

$$f_{(\lambda_i)} = \ln(I_i) = a\lambda_i^2 + b\lambda_i + c, \quad (6.10)$$

which can be used to isolate and model each spectral line. Given that the required steps to compute the EW are the same for each spectral line, the process is going to be illustrated here once, for the case of Unukalhai's absorption spectral line Fe I 7411,1544 Å:

6.1.1. Computing the wavelength shift $\Delta\lambda$

The first step is, of course, to compute the wavelength shift of the spectral lines due to the radial movement of the stars as seen from Earth. For all stars this was calculated from the definition of $\Delta\lambda$ given in equation 2.14, using the spectral line Fe I 7445,7508 Å as λ_{rest} since it appears in all spectra and is the most prominent line. In the case of Unukalhai, the shift was found to be $\Delta\lambda = 0,1012$ Å, thus locating the original laboratory-frame line Fe I 7411,1544 Å now at $\lambda_0 = 7411,2556$ Å.

6.1.2. Isolating the desired spectral line

After knowing the $\Delta\lambda$ required to locate the lines, the next step is to isolate each spectral line. Since the accuracy of the regression algorithms of Microsoft Excel —and of every other software or programming language— decreases as the magnitude of the involved numbers increases, the profile of the spectral line had to be completely moved, relocating its center at values near $\lambda = 0$. This means that the operation $\lambda_i - \lambda_{shift}$ was performed to the wavelength data of the spectral line, being λ_{shift} the first integer wavelength below the wavelength of the spectral line. In the specific case of Unukalhai's line Fe I 7411,1544 Å, the value $\lambda_{shift} = 7411$ Å was chosen, thus relocating the center of the spectral line at $\lambda_0 \approx 0,2556$ Å —after having accounted for the $\Delta\lambda$ —, as can be appreciated in figure 43.

The reader must note that performing the operation $\lambda_i - \lambda_{shift}$ does not affect the

magnitude of the EW, for the only change that happens is the shifting of the spectral line's center λ_0 , leaving the area under it unchanged. Furthermore, the inversed normalized flux is used here instead of the normalized flux for the reasons already explained in section 4.5. For illustrative purposes, figure 44 shows how Unukalhai's original normalized absorption spectral line Fe I 7411,1544 Å looks like.

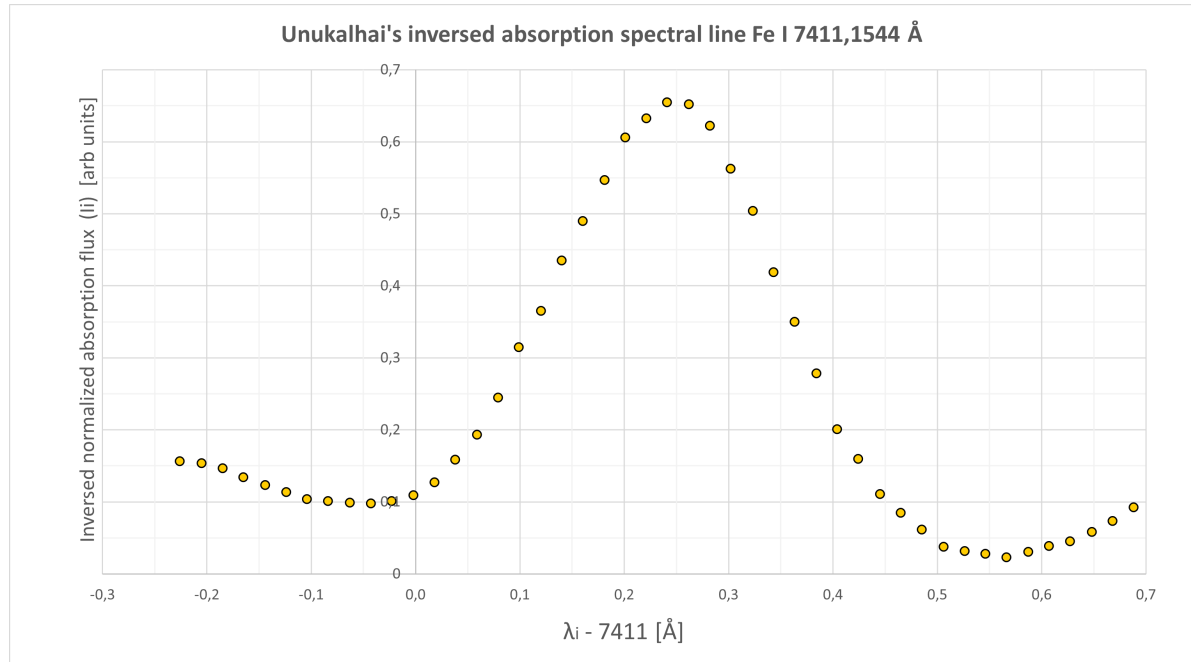


Figure 43: *Unukalhai's inversed absorption spectral line Fe I 7411,1544 Å after being relocated by performing the operation $\lambda_i - 7411 \text{ Å}$.*

6.1.3. Parabolic regression

After having isolated the desired spectral line, the natural logarithm of the inversed normalized absorption flux (I_i) was obtained in order to be able to use equation 6.10. This operation transforms the I_i values as is shown in figure 45, in which the yellow dots represent the maximum number of data points that maximizes the coefficient of determination (R^2) of the parabolic regression shown in color cyan and the blue and red dots are, respectively, the discarded lower and upper data that do not belong to the parabolic profile that the spectral line is expected to have in the $(\lambda_i, \ln(I_i))$ space. In the specific case of Unukalhai's line Fe I 7411,1544 Å —the one shown in figure 45—, the 23 yellow dots give a parabola with $R^2 = 0,9972$ and constants $a = -39,6710$, $b = 18,7860$ and $c = 2,6562$, or, more specifically, the equation

$$\ln(I_i) = -39,6710\lambda_i^2 + 18,7860\lambda_i + 2,6562 \quad (6.11)$$

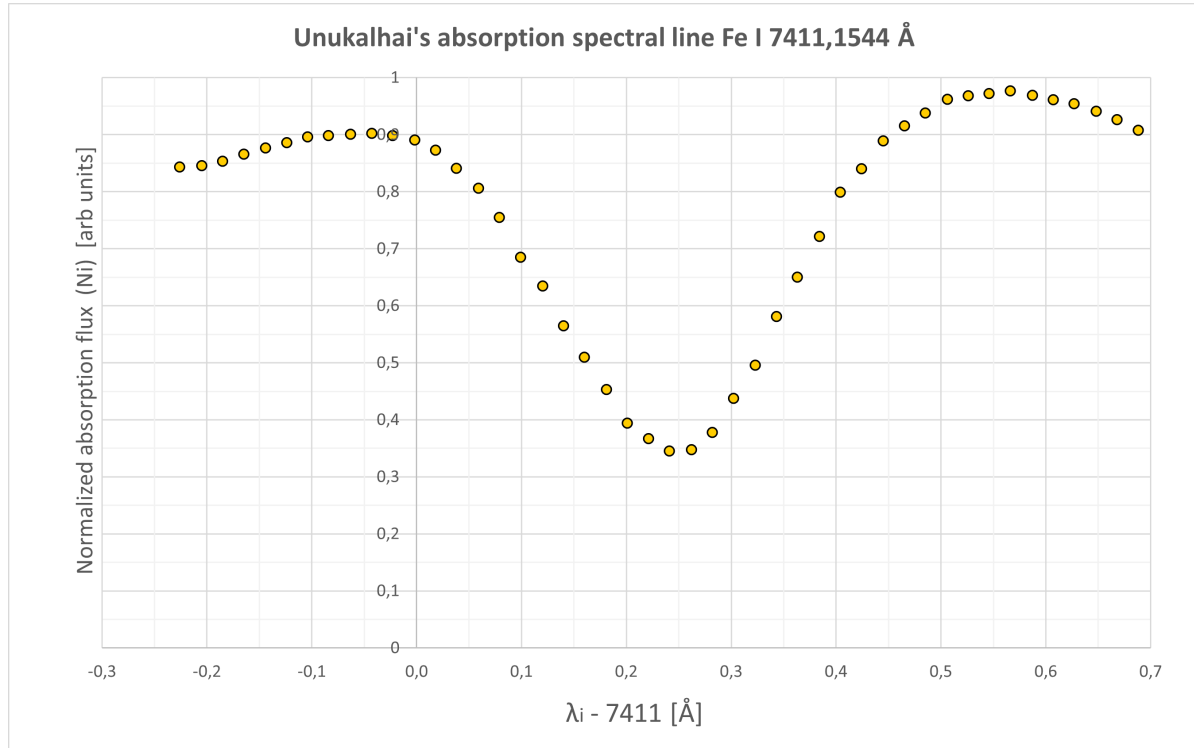


Figure 44: *Unukalhai's normalized absorption spectral line Fe I 7411,1544 Å after being relocated by performing the operation $\lambda_i - 7411 \text{ Å}$.*

6.1.4. Obtaining the isolated spectral line's gaussian profile

With the numerical value of the parabolic regression's coefficients it is now possible to use the definitions of a , b and c to find the parameters σ and λ_0 that allow to plot the profile of the isolated spectral line. In the specific case of Unukalhai's line Fe I 7411,1544 Å, these parameters acquire the values $\sigma = 0,1123$ and $\lambda_0 = 0,2368 \text{ Å}$, thus giving the inversed absorption spectral line a gaussian profile described by the equation

$$I_{(\lambda_i)} = I_i = \frac{1}{0,1123\sqrt{2\pi}} e^{-\frac{1}{2}\left(\frac{\lambda_i - 0,2368}{0,1123}\right)^2}, \quad (6.12)$$

which is shown in figure 46.

6.2. Calculating the EWs (direct method)

After having obtained the gaussian profiles of the spectral lines, the only step left is to compute their EWs. This was achieved by means of directly using equation 2.16 for all UVES-POP stars' spectral lines —since their (λ_i, F_i) data were available—, but some remarks about this process must be made. The first of them is that, since the wavelength step of the original data is basically constant (most of the times it is equal to 0,020 Å and

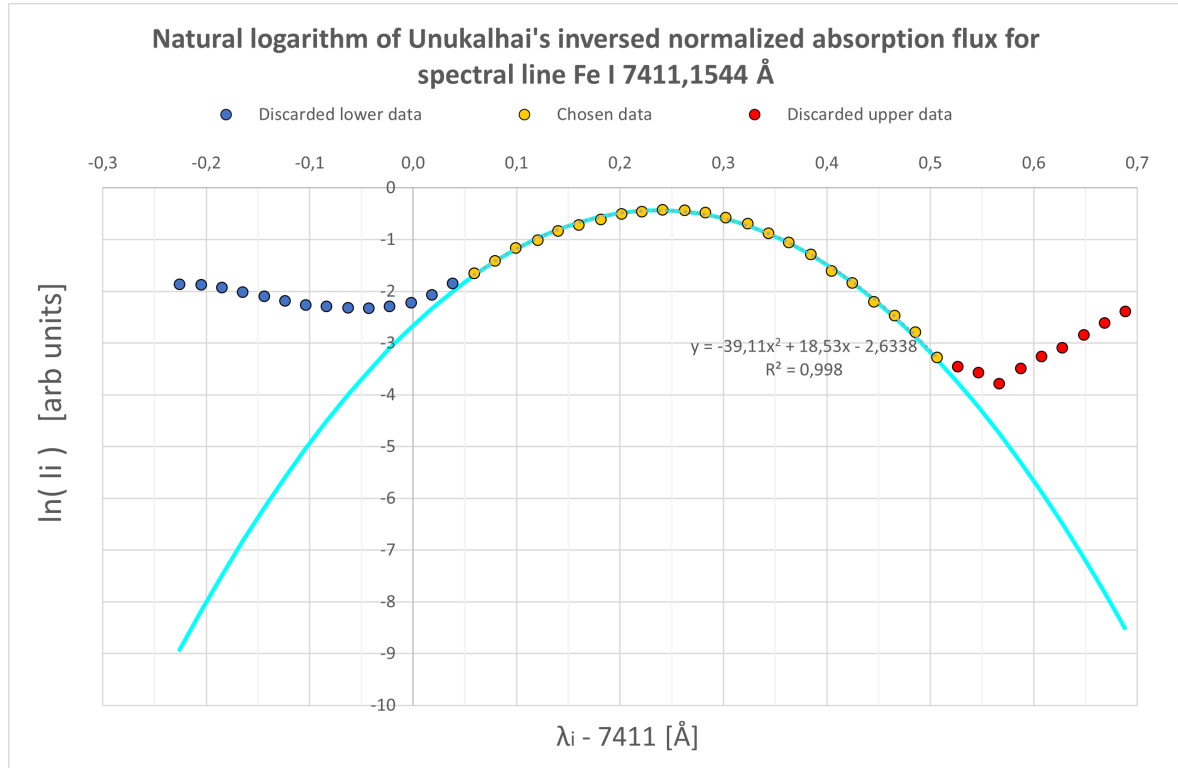


Figure 45: Natural logarithm of Unukalhai's inversed normalized absorption flux for spectral line Fe I 7411,1544 Å. The red and blue dots represent discarded data that, unlike the 23 green dots, do not adjust to the parabolic profile that the spectral line is expected to have in the $(\lambda_i, \ln(I_i))$ space.

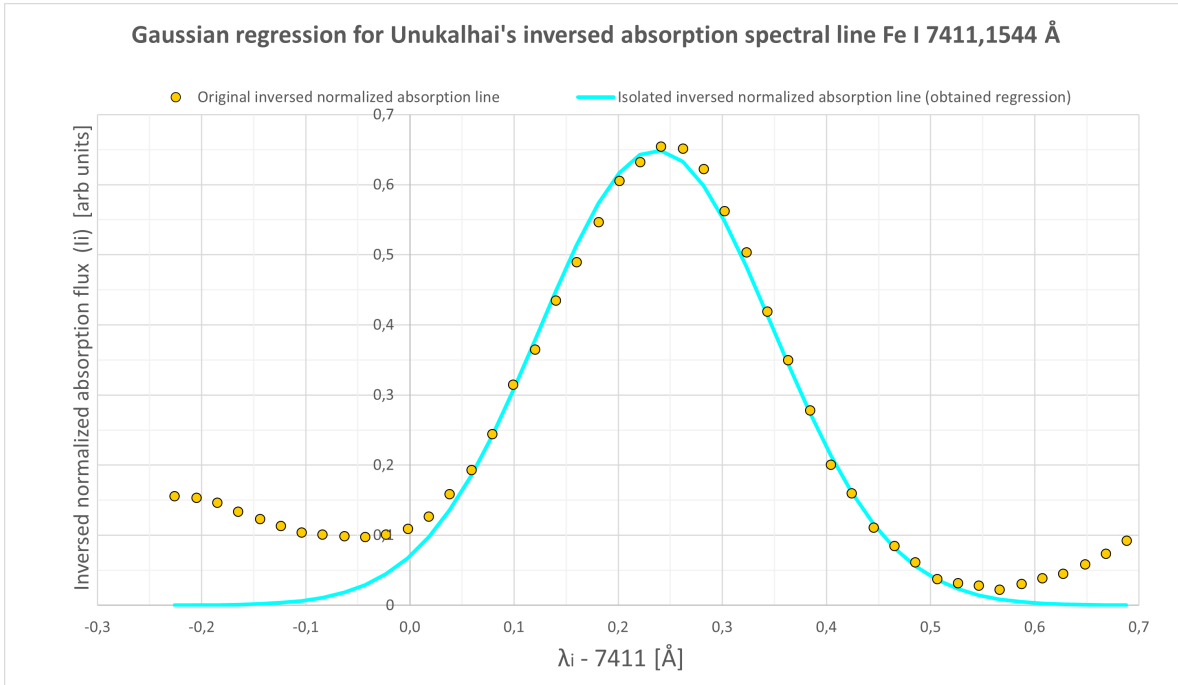


Figure 46: Gaussian regression for Unukalhai's line Fe I 7411,1544 Å (shown in cyan). As can be seen, the gaussian model of the spectral line is actually a good choice, since it matches many of the original flux data, which is shown in yellow.

sometimes to $0,021 \text{ \AA}$), equation 2.16 ends up reducing to

$$EW = d\lambda \int_{\lambda_{lower}}^{\lambda_{upper}} [1 - N_{(\lambda_i)}] = d\lambda \int_{\lambda_{lower}}^{\lambda_{upper}} I_{(\lambda_i)}, \quad (6.13)$$

where the constant step $d\lambda$ is calculated with the expression $d\lambda = \frac{\lambda_{upper} - \lambda_{lower}}{\#steps}$, with "steps" being the number of wavelength steps contained within the range $[\lambda_{lower}, \lambda_{upper}]$.

The second remark concerns the choice of the limits λ_{lower} and λ_{upper} : with the aim of standardizing the calculation of the EWs, the gaussian profile of the spectral lines was cut at the points where the inversed normalized absorption flux became less than $1,0 \times 10^{-4}$. In consequence, in the especific case of Unukalhai's line Fe I 7411,1544 \AA , the chosen extreme wavelengths were $\lambda_{lower} = 7410,774 \text{ \AA}$ (which has a corresponding inversed absorption flux of $1,326 \times 10^{-4}$) and $\lambda_{upper} = 7411,688 \text{ \AA}$ (which has a corresponding inversed absorption flux of $2,016 \times 10^{-4}$). This leads to equation 6.13 becoming

$$EW = \left(\frac{7411,688 \text{ \AA} - 7410,774 \text{ \AA}}{46 \text{ steps}} \right) \int_{7410,774 \text{ \AA}}^{7411,688 \text{ \AA}} \frac{1}{0,1123\sqrt{2\pi}} e^{-\frac{1}{2}\left(\frac{\lambda_i - 0,2368}{0,1123}\right)^2} \quad (6.14)$$

$$\approx 0,178701 \text{ \AA} = 178,701 \text{ m\AA}, \quad (6.15)$$

which is the EW of Unukalhai's line Fe I 7411,1544 \AA , whose visual depiction can be appreciated in figure 47.

6.3. Calculating the EWs (visual method)

Since data from PEPSI's spectra were not available, their spectral lines' EWs had to be computed with a visual method that relies on the fact that there exists a constant proportionality between a spectral line's EW and its full width at half maximum (hereinafter "FWHM", which is defined as the difference between the two λ values at which the inversed flux of the spectral line is equal to half of its maximum value), namely,

$$Q = \frac{EW \times F_c}{FWHM \times \frac{I_{(\lambda_0)}}{2}} = \frac{2EW \times F_c}{FWHM \times I_{(\lambda_0)}} = \frac{EW \times F_c}{\sqrt{2 \ln(2)} \sigma \times I_{(\lambda_0)}}, \quad (6.16)$$

where $I_{(\lambda_0)}$ is the intensity of the inversed flux at the center of the line λ_0 (i.e., $I_{(\lambda_0)}$ is a maximum), σ is the standard deviation of equation 6.1, F_c is the flux of the continuum and the relationship $FWHM = 2\sqrt{2 \ln(2)} \sigma$ was used.

If one takes the UVES spectra of section 6.2 and calculates the Q quotient of its spectral lines, the result is $Q \approx 2,0746 \pm 0,0031$, but the exact value of Q can be found

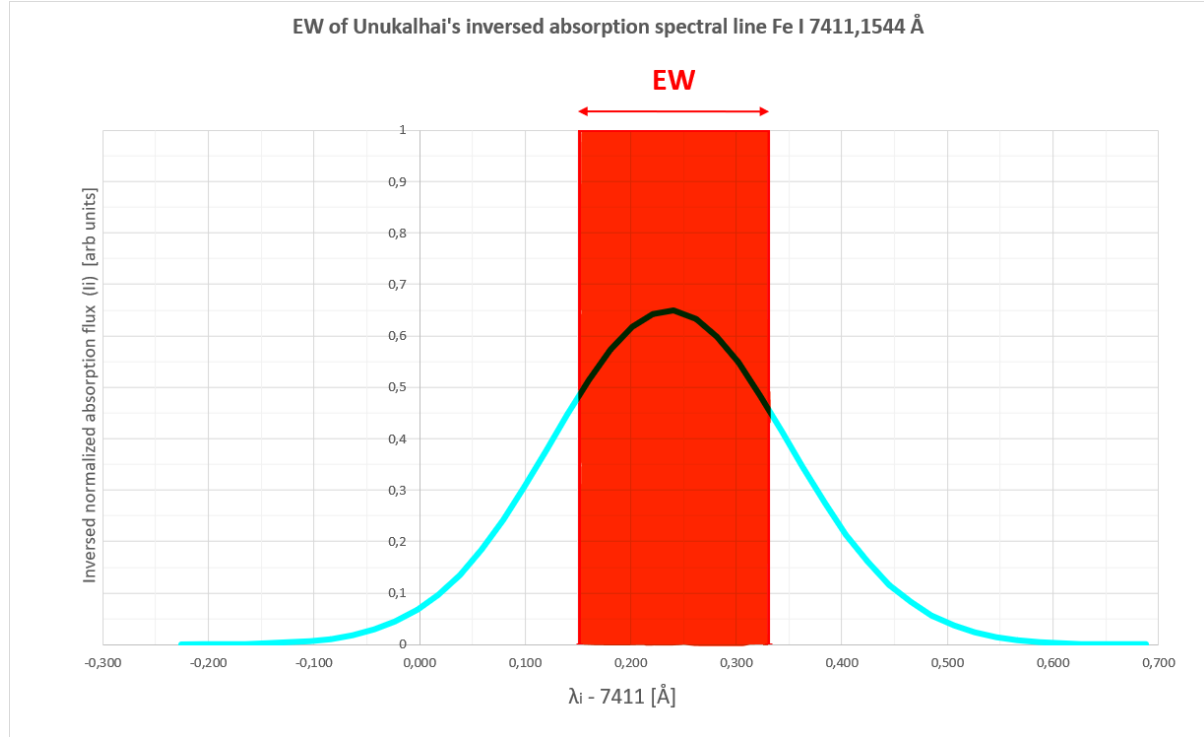


Figure 47: *EW of Unukalhai's inversed absorption spectral line Fe I 7411,1544 Å, which was calculated to be approximately equal to 0,178701 Å (or 178,701 mÅ). The red area is equal to the enclosed area by the line's gaussian profile.*

out by considering the simple case of a spectral line normalized to the continuum $F_c = 1$, with line depth equal to 1 and centered at $\lambda_0 = 0 \text{ Å}$. In that case, such line's inversed flux would be described as

$$I_{(\lambda_i)} = I_i = e^{-\frac{1}{2}(\sqrt{2\pi}\lambda_i)^2}, \quad (6.17)$$

where $\sigma = \frac{1}{\sqrt{2\pi}}$, as equation 6.1 suggests due to the fact that $\text{MAX}(I_i) = I_{(\lambda_0)} = 1 = \frac{1}{\sqrt{2\pi}\sigma}$. Using equations 2.16, 6.16 and 6.17 it is then possible to see that

$$Q = \frac{\int_{-\infty}^{\infty} e^{-\frac{1}{2}(\sqrt{2\pi}\lambda)^2} d\lambda}{\sqrt{2 \ln(2)} \frac{1}{\sqrt{2\pi}} \times 1} = \frac{1}{\sqrt{\frac{2 \ln(2)}{2\pi}}} = \sqrt{\frac{\pi}{\ln(2)}}, \quad (6.18)$$

thus turning equation 6.16 into

$$\boxed{EW = \sqrt{\frac{\pi}{\ln(2)}} \frac{FWHM \times I_{(\lambda_0)}}{2F_c}}, \quad (6.19)$$

which, assuming the spectra to be normalized into the flux range $[0, 1]$ (i.e., $F_c = 1$, as is the case with PEPSI's spectra), reduces to

$$EW = \sqrt{\frac{\pi}{\ln(2)}} \frac{FWHM \times I_{(\lambda_0)}}{2}. \quad (6.20)$$

With all this in mind, the EWs of PEPSI's stars were computed following the process below, which gives the example for Unukalhai's line Fe I 7411,1544 Å:

1. Normalize the spectrum within the flux range [0, 1] (in the case of PEPSI spectra this step is already done).

2. Locate the desired absorption spectral line after having accounted for the change of wavelength $\Delta\lambda$ due to the radial movement of the star. In this example, $\Delta\lambda = +0,1012$.

3. Locate the minimum value of the normalized data N_i (which are defined in equation 4.5) that belong to that spectral line. This point is labeled " $N_{(\lambda_0)}$ " and is shown in figure 48. In the specific case of Unukalhai's absorption spectral line Fe I 7411,1544 Å, this is $N_{(\lambda_0)} = 0,345201505$.

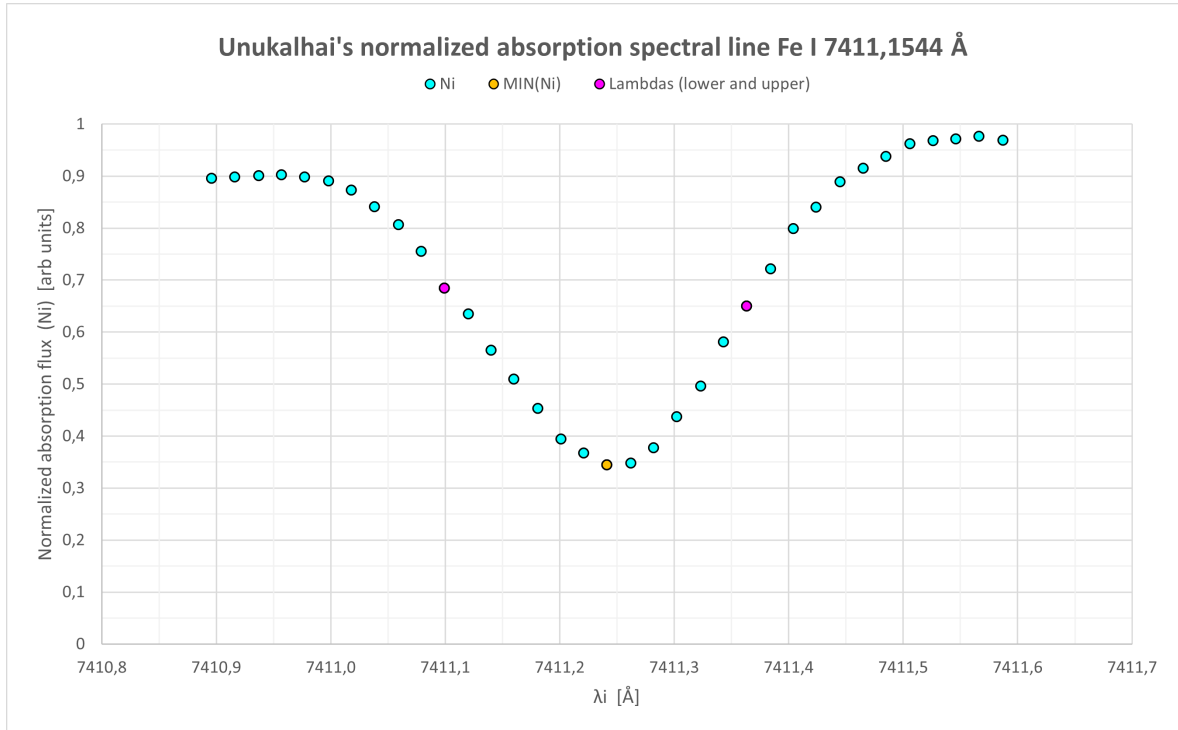


Figure 48: Illustrative diagram for how to visually obtain the EW from $N_{(\lambda_0)}$, λ_{lower} and λ_{upper} , as explained in section 6.3.

4. From the definition of the inversed normalized absorption flux (4.8) it is immediately clear that $MAX(I_i) = I_{(\lambda_0)} = 1 - N_{(\lambda_0)}$. In this specific example, $I_{(\lambda_0)} = 0,654798495$.

5. The value $\frac{I_{(\lambda_0)}}{2}$ is now calculated, for the wavelengths associated with that value are the ones that are going to define the FWHM, as is clear from equation $FWHM = \lambda_{\left(\frac{I_{(\lambda_0)}}{2}\right)_{upper}} - \lambda_{\left(\frac{I_{(\lambda_0)}}{2}\right)_{lower}}$ and figure 49. For this example, $\frac{I_{(\lambda_0)}}{2} = 0,327399248$.

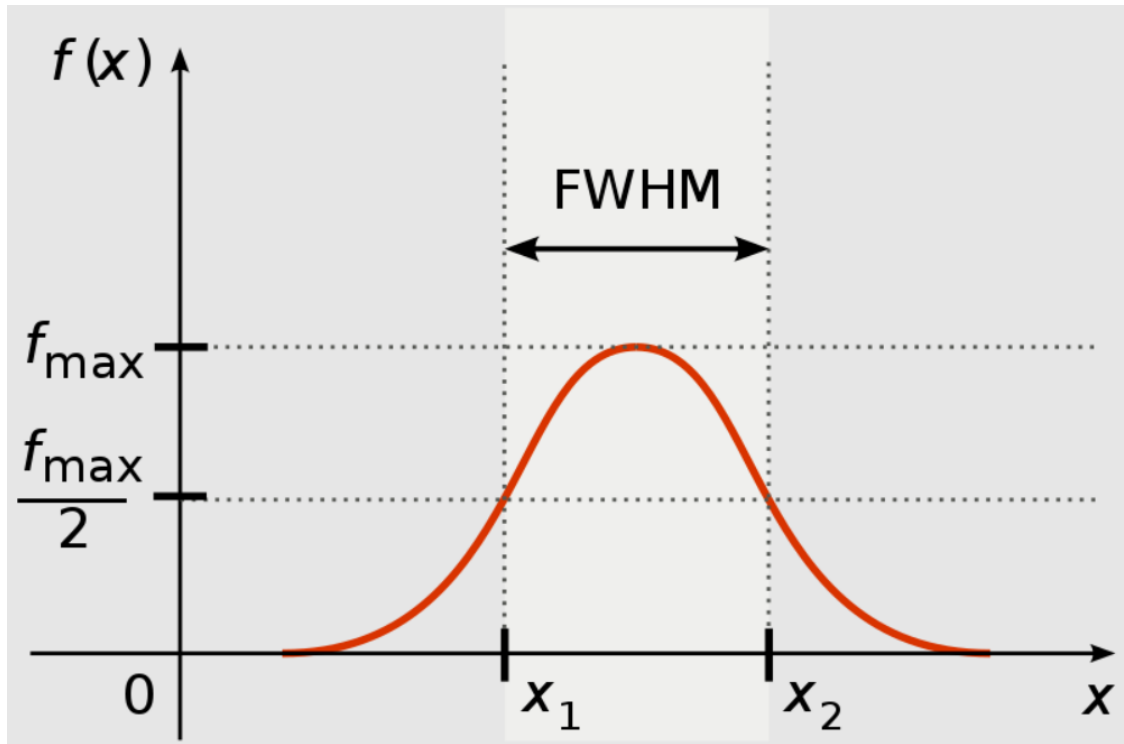


Figure 49: Geometric definition of the full width at half maximum (FWHM). Image taken from [11].

6. However, it is not necessary to plot the gaussian profile of the inversed spectral line—as is the case in section 4—because the wavelengths that define the line’s FWHM can be found directly in the normalized spectrum of figure 48 by just performing the operation $N_{FWHM} = 1 - \frac{I(\lambda_0)}{2}$. For this example, that is $N_{FWHM} = 0,672600753$.

7. Now the N_i closest to this flux value are looked for. In this example, those are $N_{lower} = 0,684938176$ and $N_{upper} = 0,650008553$, which are associated to the wavelengths $\lambda_{lower} = 7411,099 \text{ \AA}$ and $\lambda_{upper} = 7411,363 \text{ \AA}$, respectively.

8. The FWHM is calculated from equation $FWHM = \lambda_{upper} - \lambda_{lower}$, giving for this example $FWHM = 0,264 \text{ \AA}$.

9. Finally, the EW of the spectral line is found with equation

$$EW = \sqrt{\frac{\pi}{\ln(2)}} \frac{FWHM}{2} [1 - N(\lambda_0)]. \quad (6.21)$$

In this example, $EW \approx 0,179311813 \text{ \AA} \approx 179,312 \text{ m\AA}$, which is only 0,611 m\AA away from the same calculation with the direct method (equation 6.14) and thus gives confidence in the visual method.

7. Results and discussion

The results of the measurement of the EWs of the absorption spectral lines of Fe I, Ti I and CN I of the 31 stars found are going to be shown and discussed in this section, beginning with the numerical value obtained for the EWs and their averages, followed by the analysis of the quotients between those EWs and concluding with an exploration in which a connection between the quotients and some astrometric quantities is searched for.

7.1. The Equivalent Widths

The EWs of the Fe I, Ti I and CN I lines studied in all stars are shown in tables 50, 51 and 52, respectively. In order to be able to make sense of these data more easily, the average of those lines (\overline{EW}) was computed for each star and plotted against the star's M_V and $B - V$ index, as is depicted in figures 53 and 54, respectively. At first glance, these figures reveal that Fe I and Ti I are on average stronger in RGB stars and that CN I lines are stronger in RC stars, with the important detail that RC stars seem to have on average stronger Fe I, Ti I and CN I lines than RGB stars with the same $B - V$ index, as the range $B - V = [1.15, 1.25]$ of graph 53 suggests. However, these figures are far from giving the spectroscopic method to differentiate RC stars from RGB stars, for one figure seems to contradict the other in respect to the unknown stars: if one looks at figure 53, it might look like one of the stars whose evolutionary status is unknown (the one with $B - V = 1.07$, HD95689), is a RC star since all of its \overline{EW} s lie on the RC stars' lines, but that same star is the one with $M_V = -1.10$ in figure 54, which lies just above the RGB stars' lines among other 2 unknown stars; furthermore, there is another unknown star (HD95405) that presents this behavior but reversed: it looks like a RC star in the (M_V, \overline{EW}) graph, but like a RGB star in the $(B - V, \overline{EW})$ graph. These two cases show that the \overline{EW} s, the absolute visual magnitudes and the $B - V$ indexes are not enough to distinguish between RC and RGB stars, thus motivating a further exploration regarding the quotients of the \overline{EW} s.

7.2. Quotients of Equivalent Widths

Figures 55 and 56 show, respectively, the value of the quotients $\frac{\overline{EW}_{Ti}}{\overline{EW}_{CN}}$ and $\frac{\overline{EW}_{Fe}}{\overline{EW}_{CN}}$ plotted against the $B - V$ index, while figures 57 and 58 display the same quotients but against M_V . Figures 56 and 58 do not appear to give much information since both RC and RGB stars are dispersed and some of the unknown stars seem to be from the RC in one graph

	#	HD Identifier	Average EW [mÅ]			
			Fe I			
Group	---		7411,1544	7445,7508	7461,5206	7495,0674
RC	1	140573	178,7	180,7	102,4	196,7
	2	169916	131,8	141,7	74,1	155,6
	3	85503	177,2	192,1	120,2	214,2
	4	110458	153,0	171,9	91,9	232,5
	5	83240	135,5	149,7	79,5	165,4
	6	99322	135,9	152,7	77,1	165,5
	7	45415	133,1	150,4	77,4	161,9
	8	121416	152,1	165,2	96,7	178,7
	9	11643	159,3	165,6	91,0	176,0
	A1	RC Average	150,7	163,3	90,0	183,0
Unknown	10	95405	153,9	143,6	94,3	169,3
	11	202320	149,7	174,3	87,6	178,4
	12	148291	168,9	198,1	105,5	196,3
	13	95689	153,9	176,2	91,8	184,9
RGB	14	124897	129,1	144,3	81,4	149,3
	15	29139	132,2	163,3	106,3	164,2
	16	107446	141,5	163,9	102,1	172,7
	17	152786	166,2	193,0	124,2	198,7
	18	138688	148,0	125,1	103,7	221,0
	19	145206	6,3	178,2	107,1	180,0
	20	167818	167,2	196,0	113,9	206,9
	21	206778	195,9	243,0	137,1	265,2
	22	225212	217,2	266,5	153,6	271,3
	23	198357	150,2	169,5	107,4	177,9
	24	199642	122,5	150,3	96,8	156,3
	25	12642	135,2	165,3	109,6	173,7
	26	119090	100,9	135,9	91,9	145,6
	27	149447	139,8	167,8	109,6	169,3
	28	89736	182,0	220,6	141,2	222,1
	29	12929	135,0	148,8	88,9	152,1
	30	107328	131,8	155,8	89,9	164,5
	A2	RGB Average	141,2	175,7	109,7	187,7
AGB	31	220009	111,6	124,8	72,9	136,3

Figure 50: Equivalent Widths of the 4 Fe I lines studied in all spectra. All the uncertainties were assumed to be $\pm 5\%$ for the reasons explained in appendix A.

Group	#	HD Identifier	EW [mÅ]
			Ti I
RC	---		7440,5765
	1	140573	69,1
	2	169916	38,1
	3	85503	90,7
	4	110458	47,5
	5	83240	40,4
	6	99322	32,6
	7	45415	36,8
	8	121416	57,8
	9	11643	53,5
Unknown	A1	RC Average	51,8
	10	95405	42,3
	11	202320	37,2
	12	148291	55,2
RGB	13	95689	48,9
	14	124897	61,1
	15	29139	108,7
	16	107446	82,1
	17	152786	101,5
	18	138688	88,0
	19	145206	90,2
	20	167818	71,4
	21	206778	98,1
	22	225212	128,8
	23	198357	80,8
	24	199642	97,6
	25	12642	113,9
	26	119090	45,2
	27	149447	112,2
	28	89736	133,2
	29	12929	52,0
	30	107328	56,5
AGB	A2	RGB Average	89,5
	31	220009	52,4

Figure 51: Equivalent Width of the line Ti I 7440,5765 Å studied in all spectra. All the uncertainties were assumed to be $\pm 5\%$ for the reasons explained in appendix A.

Group	#	HD Identifier	Average EW [mÅ]			
			CN I			
			7448,245	7451,355 + 7451,473	7452,086 + 7452,194	7488,001
RC	---		7448,245	7451,355 + 7451,473	7452,086 + 7452,194	7488,001
	1	140573	28,0	39,9	75,8	42,2
	2	169916	9,0	10,5	32,0	14,9
	3	85503	39,1	58,9	90,1	50,6
	4	110458	17,0	25,2	57,0	29,1
	5	83240	11,1	15,7	41,7	18,4
	6	99322	11,5	16,1	39,1	14,9
	7	45415	10,2	14,7	36,4	14,8
	8	121416	16,6	28,8	58,9	29,0
	9	11643	15,1	25,8	57,3	24,8
Unknown	A1	RC Average	17,5	26,2	54,2	26,5
	10	95405	40,5	74,0	92,3	60,2
	11	202320	6,5	12,9	38,8	13,4
	12	148291	15,3	26,9	54,7	25,1
	13	95689	19,3	33,6	53,1	28,5
	14	124897	4,7	9,6	23,0	10,7
	15	29139	10,3	23,2	35,4	23,6
	16	107446	6,2	13,6	34,0	12,1
	17	152786	11,0	31,2	49,9	26,3
	18	138688	7,5	26,5	48,5	22,5
RGB	19	145206	18,7	32,6	55,0	26,8
	20	167818	8,8	18,6	40,4	19,3
	21	206778	3,5	8,2	40,6	16,2
	22	225212	22,8	43,9	70,6	41,0
	23	198357	10,2	18,2	43,6	17,8
	24	199642	3,6	9,7	18,4	6,7
	25	12642	14,7	31,8	40,0	21,8
	26	119090	1,5	3,7	15,0	5,1
	27	149447	11,1	21,0	35,8	17,9
	28	89736	22,2	43,5	56,2	37,5
	29	12929	13,3	21,4	42,1	19,0
	30	107328	10,9	15,5	27,4	16,2
	A2	RGB Average	10,6	21,9	39,8	20,0
AGB	31	220009	5,2	8,4	15,1	7,2

Figure 52: Equivalent Widths of the 4 CN I lines studied in all spectra. All the uncertainties were assumed to be $\pm 5\%$ for the reasons explained in appendix A.

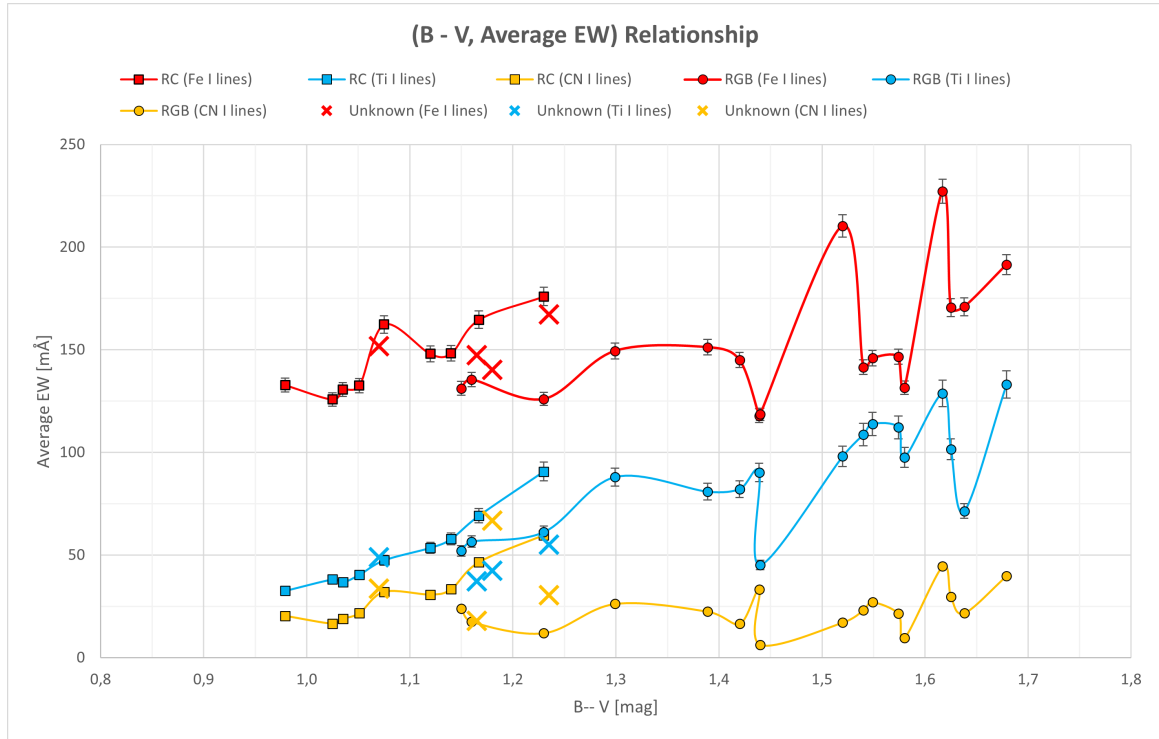


Figure 53: Average EW of 4 Fe I lines, 1 Ti I line and 4 CN I lines as a function of $B - V$ index, for RC, RGB and unknown stars.

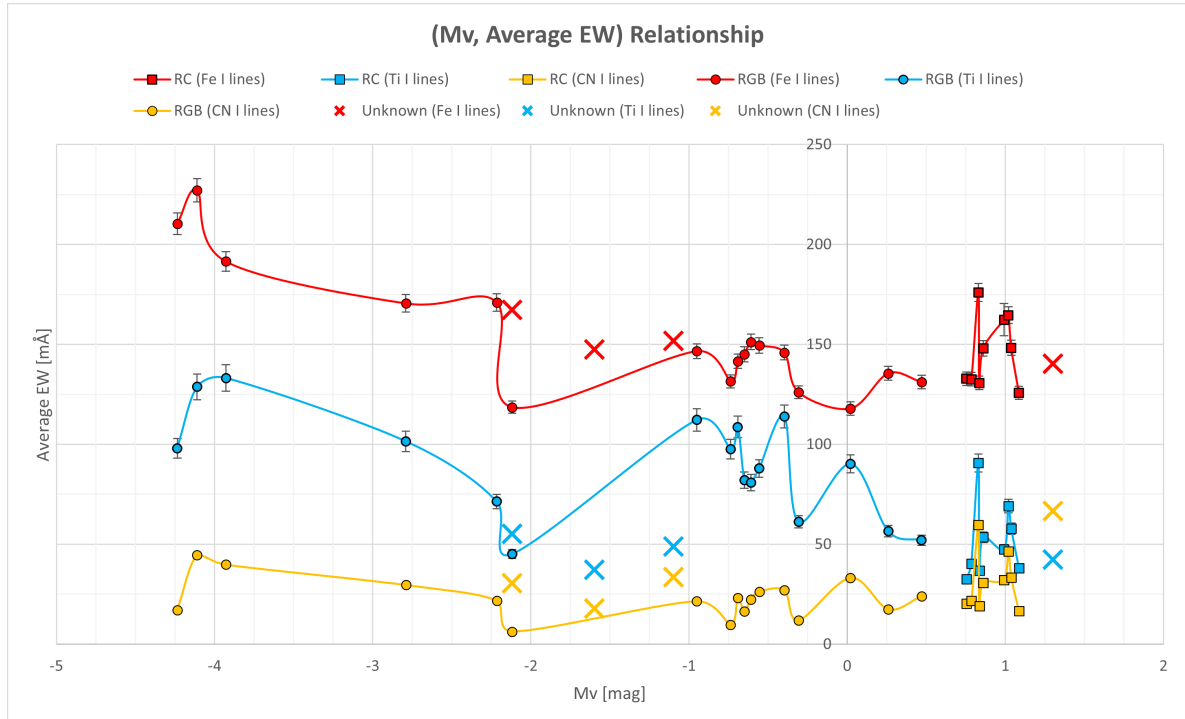


Figure 54: Average EW of 4 Fe I lines, 1 Ti I line and 4 CN I lines as a function of the absolute visual magnitude M_V , for RC, RGB and unknown stars.

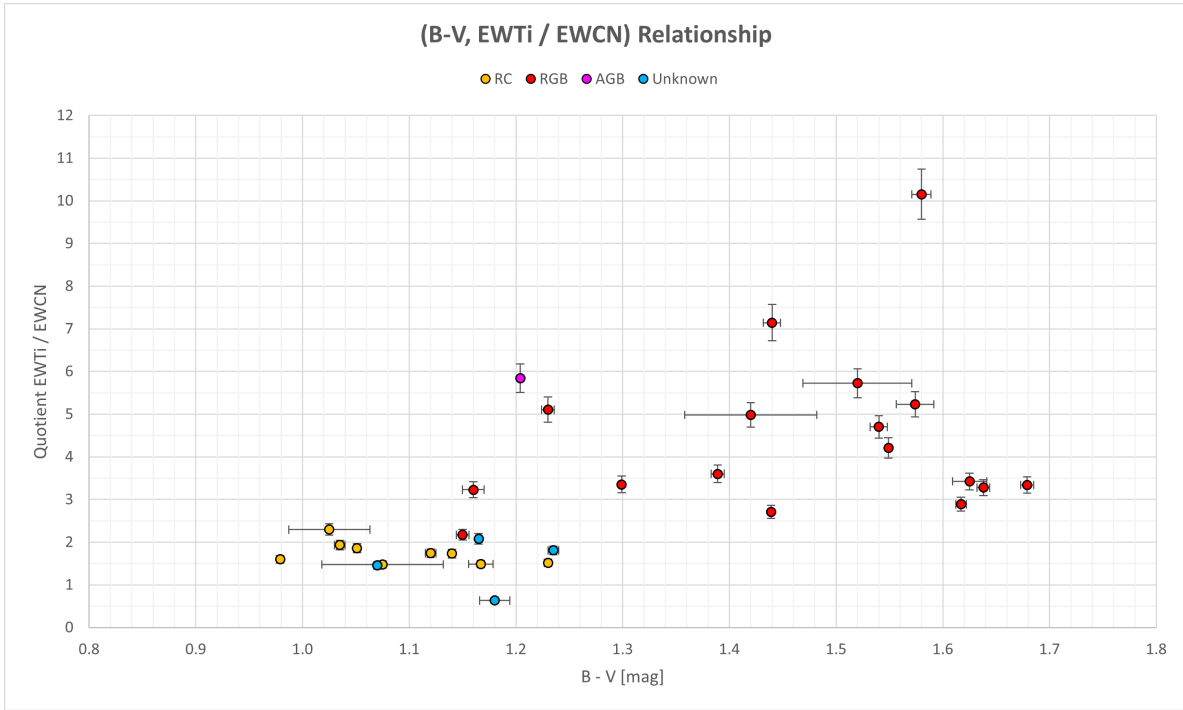


Figure 55: Quotient $\frac{\overline{EW}_{Ti}}{\overline{EW}_{CN}}$ as a function of $B - V$ index for RC, RGB, AGB and unknown stars.

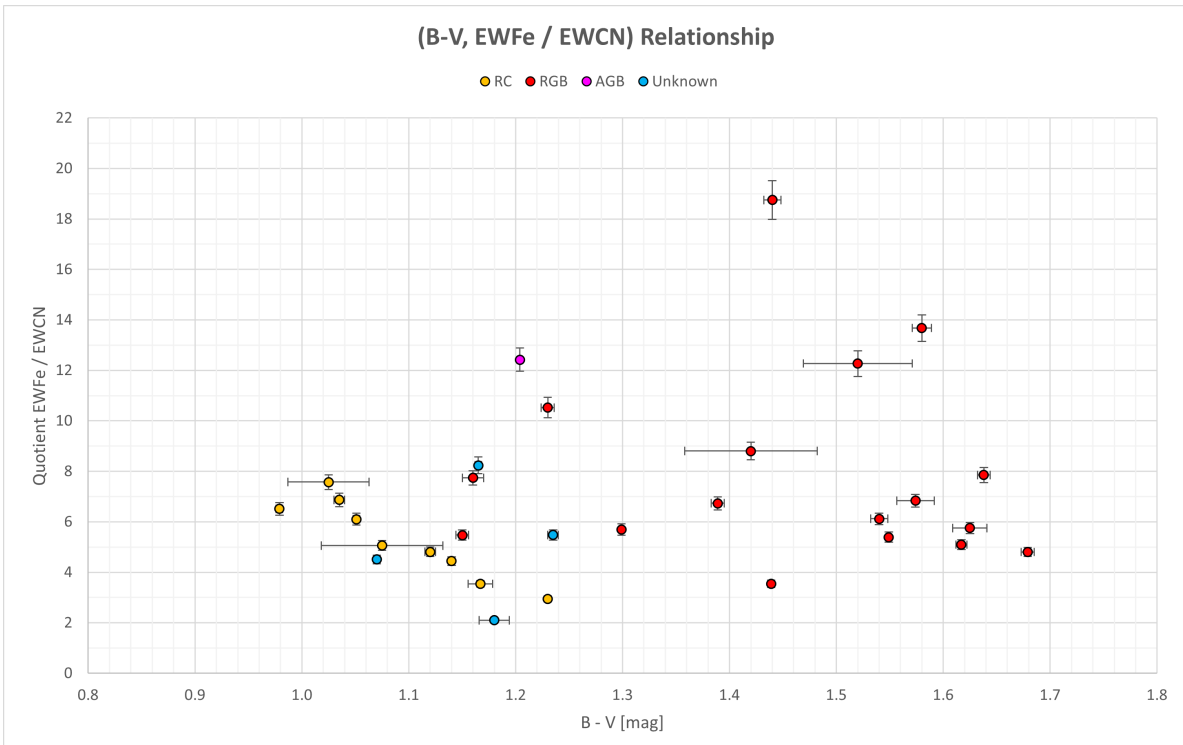


Figure 56: Quotient $\frac{\overline{EW}_{Fe}}{\overline{EW}_{CN}}$ as a function of $B - V$ index for RC, RGB, AGB and unknown stars.

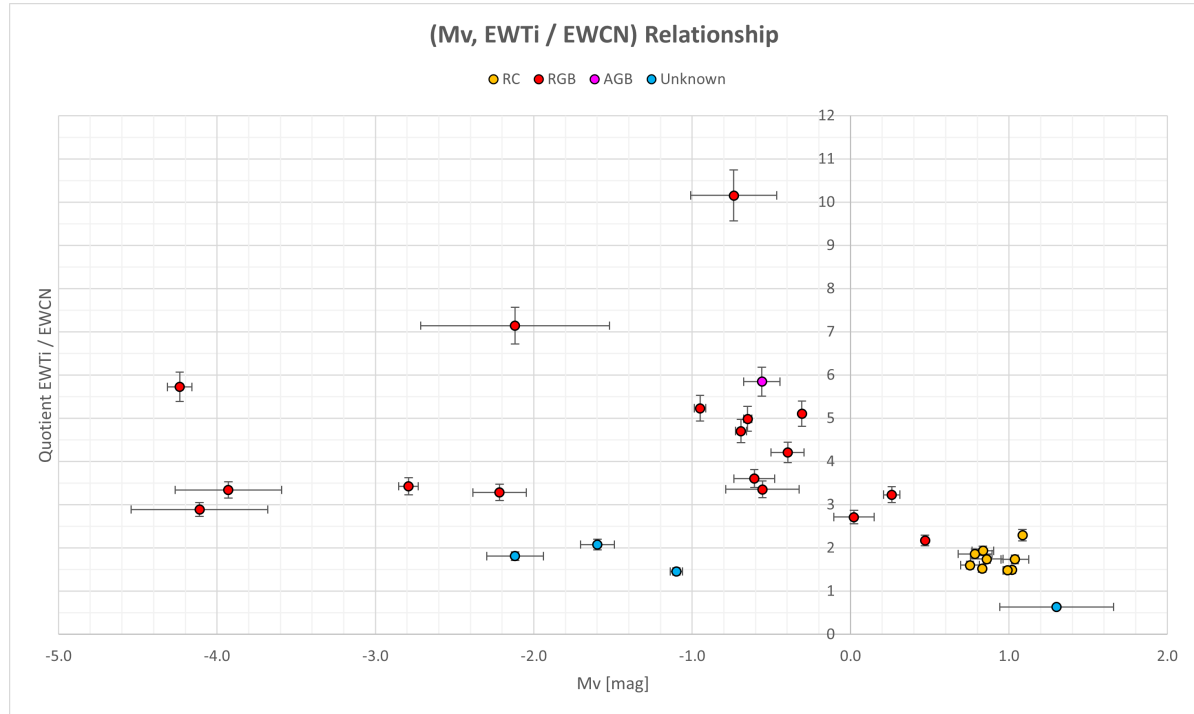


Figure 57: Quotient $\frac{\overline{EW}_{Ti}}{\overline{EW}_{CN}}$ as a function of the absolute visual magnitude M_V for RC, RGB, AGB and unknown stars.

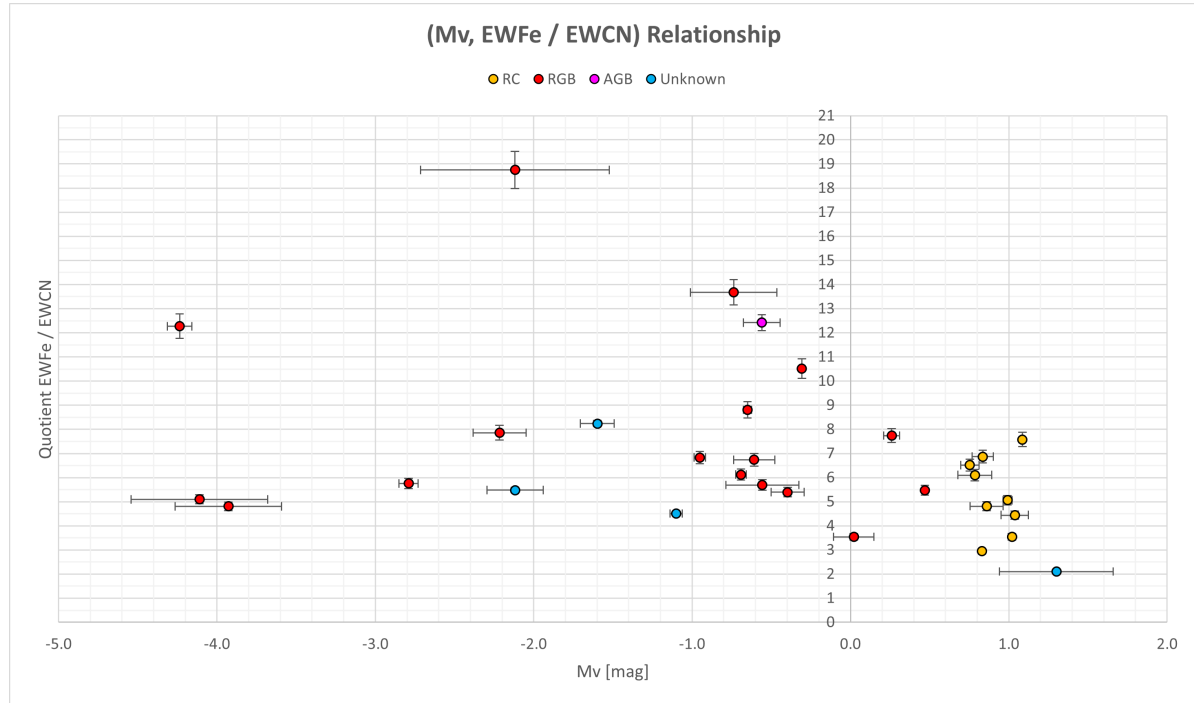


Figure 58: Quotient $\frac{\overline{EW}_{Fe}}{\overline{EW}_{CN}}$ as a function of the absolute visual magnitude M_V for RC, RGB, AGB and unknown stars.

but from the RGB in the other one, as was the case for figures 53 and 54; figures 55 and 57, on the other hand, give a promising result: the quotient $\frac{\overline{EW}_{Ti}}{\overline{EW}_{CN}}$ seems to be ≤ 2.5 for RC stars, and > 2.5 for RGB stars. In that case, the spectroscopic relationship

$$\frac{\overline{EW}_{Ti}}{\overline{EW}_{CN}} = \frac{\overline{FWHM}_{Ti} \times \bar{I}_{(\lambda_0_{Ti})}}{\overline{FWHM}_{CN} \times \bar{I}_{(\lambda_0_{CN})}} \leq 2.5 \quad (7.1)$$

would hold for RC stars, thus giving the initial impression that all of the four unknown stars are actually RC stars; however, a look at the HR diagram of the studied stars (figure 23) clearly shows that cannot be the case since three of those unknown stars are much brighter than RC stars, meaning they could be carbon stars (i.e., post-RC stars with high C content traveling up the AGB), as their low $\frac{\overline{EW}_{Ti}}{\overline{EW}_{CN}}$ seems to confirm. On the other hand, the initial impression also suggests that the only RGB star that appears with $\frac{\overline{EW}_{Ti}}{\overline{EW}_{CN}} < 2.5$ (the reddest RGB star, HD12929) might actually be a misclassified star. Given that one factor that could have provoked the misrating of HD12929 is an inaccurate parallax that would have brought with it a consequent inaccurate M_V , HD12929's updated parallax was looked for in SIMBAD's literature but no results were found since the star does not even seem to have a GAIA DR3 identifier, what means that the star (which has $V = 2$) is too bright for Gaia and that Hipparcos' parallax is probably very accurate, thus making the possibility of HD12929 being a RGB star more likely, but still leaving the question of whether it is misrated or not still open.

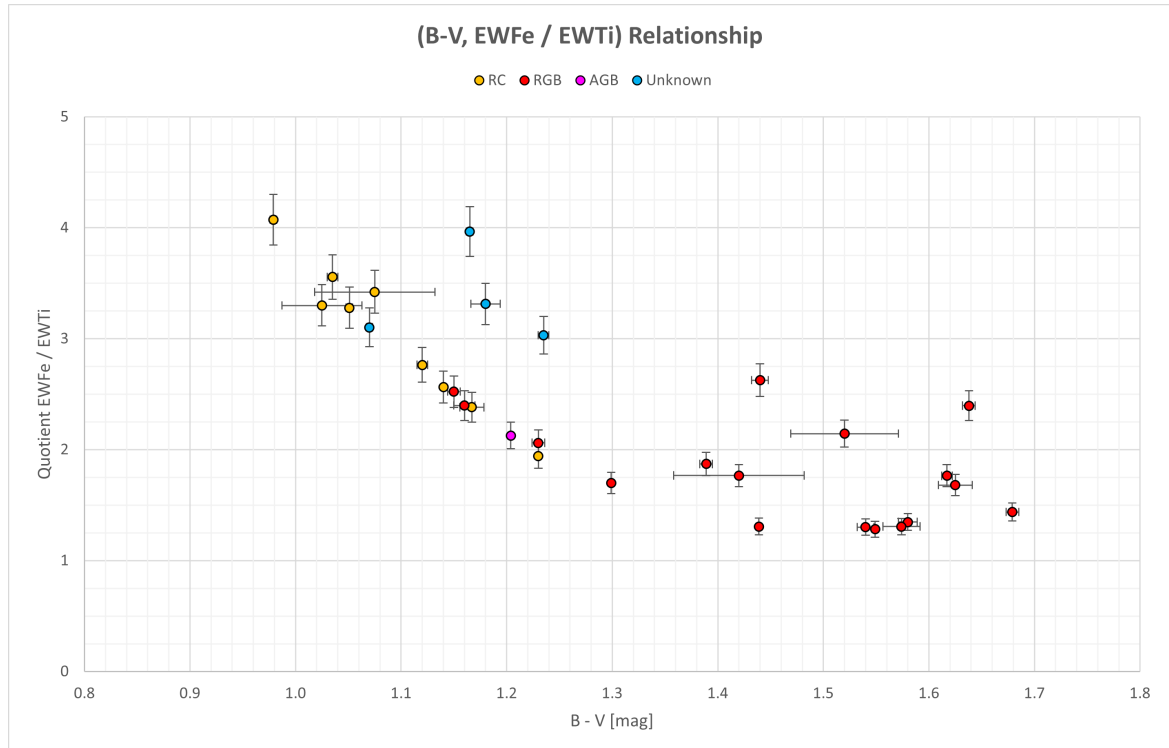


Figure 59: Quotient $\frac{\overline{EW}_{Fe}}{\overline{EW}_{Ti}}$ as a function of $B - V$ index for RC, RGB, AGB and unknown stars.

Additionally, figure 59 exhibits the stars' ($B - V$, $\frac{\overline{EW}_{Fe}}{\overline{EW}_{Ti}}$) relationship and reveals an interesting feature: all groups of stars (RC, RGB, AGB and unknown) seem to form a linear relationship with negative slope at the left part of the diagram, which is useful as a test of consistency to check the stars' evolutionary status. Nevertheless, since the main objective of this dissertation is the study of the behavior of the intensity of the CN I lines against that of the Fe I and Ti I lines, figure 59 is out of scope and thus will be left undiscussed.

Now, digging even deeper, the \overline{EW} s' quotients were plotted one against each other and the results are shown in figures 60, 61 and 62. Figure 60 does not show anything new other than the suspected $\frac{\overline{EW}_{Ti}}{\overline{EW}_{CN}} \leq 2.5$ range for RC stars already deduced from figures 55 and 57, but figures 61 and 62 both give encouraging results, for they both seem to almost completely separate the RC from the RGB, even leaving a considerable space between both groups where no star lies. As the reader might have already noted, in all figures 60, 61 and 62 all of the 4 unknown stars (3 of which have already been said to probably belong to the AGB) and HD12929 (the star that might have been misclassified) are mixed with the RC stars, hinting that some important event might happen between the end of the RGB phase and the beginning of the HB phase, an event capable of increasing the C content of the stars' photospheres a lot and thus responsible for the clear spectroscopic difference between RGB and RC stars that seems to arise in all graphs based on their \overline{EW} s' quotients.

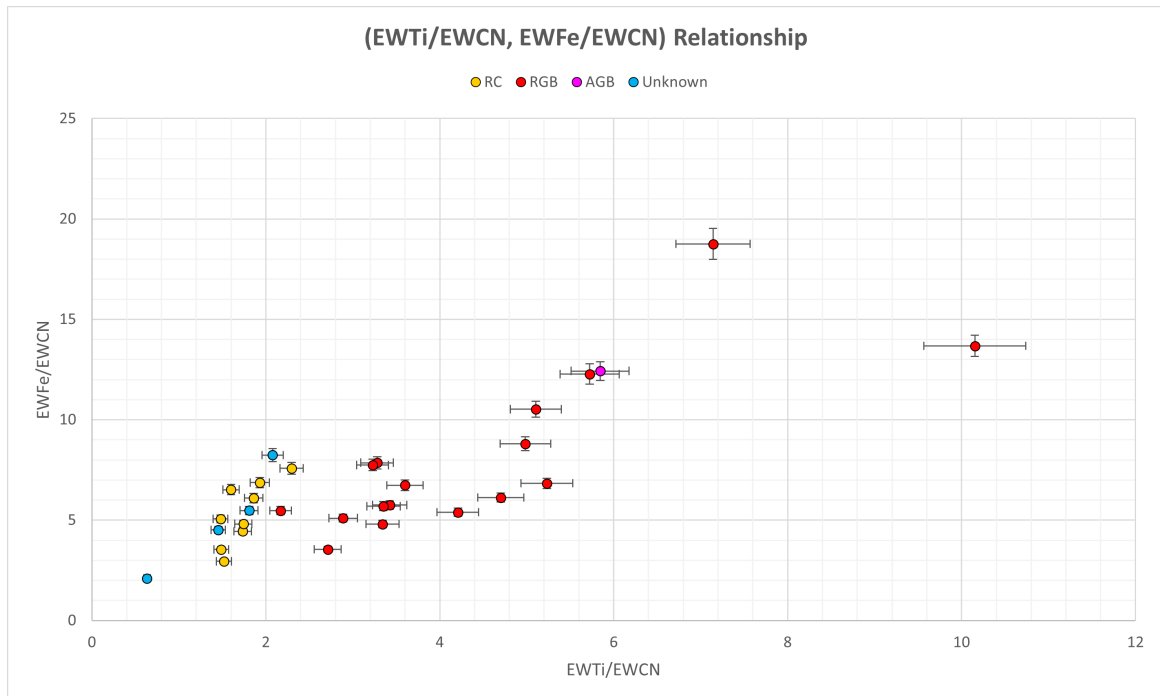


Figure 60: Quotients $\frac{\overline{EW}_{Ti}}{\overline{EW}_{CN}}$ and $\frac{\overline{EW}_{Fe}}{\overline{EW}_{CN}}$ plotted against each other for RC, RGB, AGB and unknown stars.

7.3. Relation with other stellar parameters

In search for relations between the EWs and other stellar properties, the metallicity, surface gravity and mass of the 31 studied stars were searched in SIMBAD database [19] and in VizieR's catalogue access tool [18], obtaining the values shown in table 77. Note that, since some stars' data could not be found, the figures below were obtained with the available data online only.

7.3.1. Metallicity [Fe/H]

Figures 63 and 64 show the quotients $\frac{\overline{EW}_{Ti}}{\overline{EW}_{CN}}$ and $\frac{\overline{EW}_{Fe}}{\overline{EW}_{CN}}$ as a function of metallicity [Fe/H], respectively. These two graphs are harder to read because data are more spread out and thus the limits between RC and RGB stars are not so clear as they were in graphs 60, 61 and 62. Figure 63 isolates RC stars vertically with the already suggested range $\frac{\overline{EW}_{Ti}}{\overline{EW}_{CN}} \leq 2.5$, but there does not seem to be a strong enough correlation with [Fe/H] to separate the data horizontally, as can be seen from the fact that RC and RGB stars' metallicities superimpose within the [Fe/H] range [-0.15 dex, 0.1 dex], now making 2 unknown stars look as if they were RGB stars (based on the metallicity range alone) and even making the suspicious HD12929 ([Fe/H] = -0.25 dex) look as if it were indeed a RGB star, now casting doubt on star HD225212, with [Fe/H] = 0.08 dex. In the same way, figure 64 presents the same issues but much more dramatically: the two unknown stars and HD12929 are now more mixed with RGB stars, and HD225212 is now literally surrounded by all RC stars. In view of the fact no visible trend arises, it seems like [Fe/H] and the \overline{EW} s' quotients are not enough to distinguish between the evolutionary states of red giants, but more research on the unknown stars—and on the suspicious HD12929—would be required to be able to assert this with conviction.

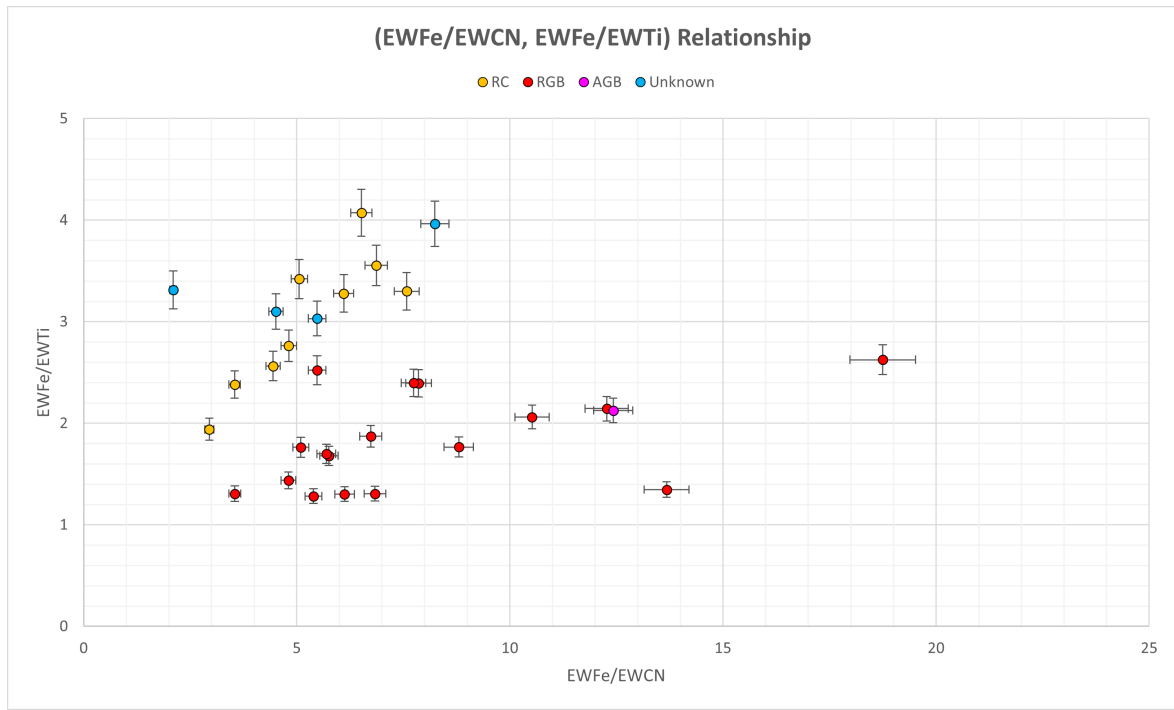


Figure 61: Quotients $\frac{\overline{EW}_{Fe}}{\overline{EW}_{CN}}$ and $\frac{\overline{EW}_{Fe}}{\overline{EW}_{Ti}}$ plotted against each other for RC, RGB, AGB and unknown stars.

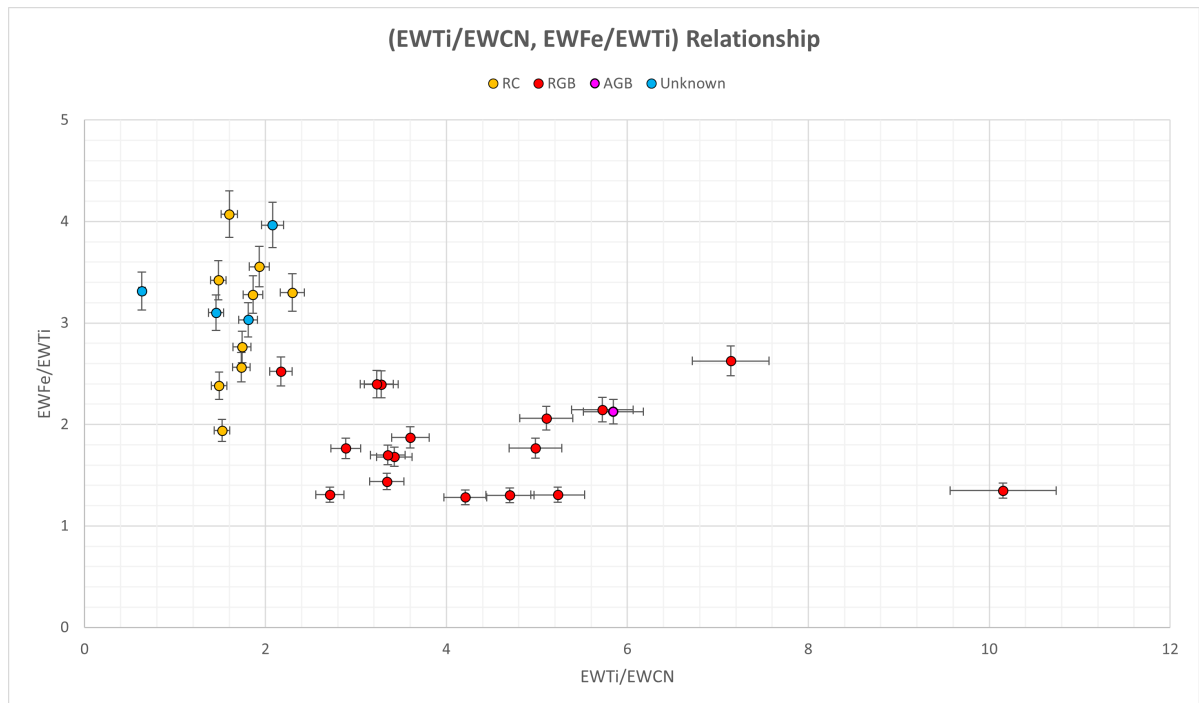


Figure 62: Quotients $\frac{\overline{EW}_{Ti}}{\overline{EW}_{CN}}$ and $\frac{\overline{EW}_{Fe}}{\overline{EW}_{Ti}}$ plotted against each other for RC, RGB, AGB and unknown stars.

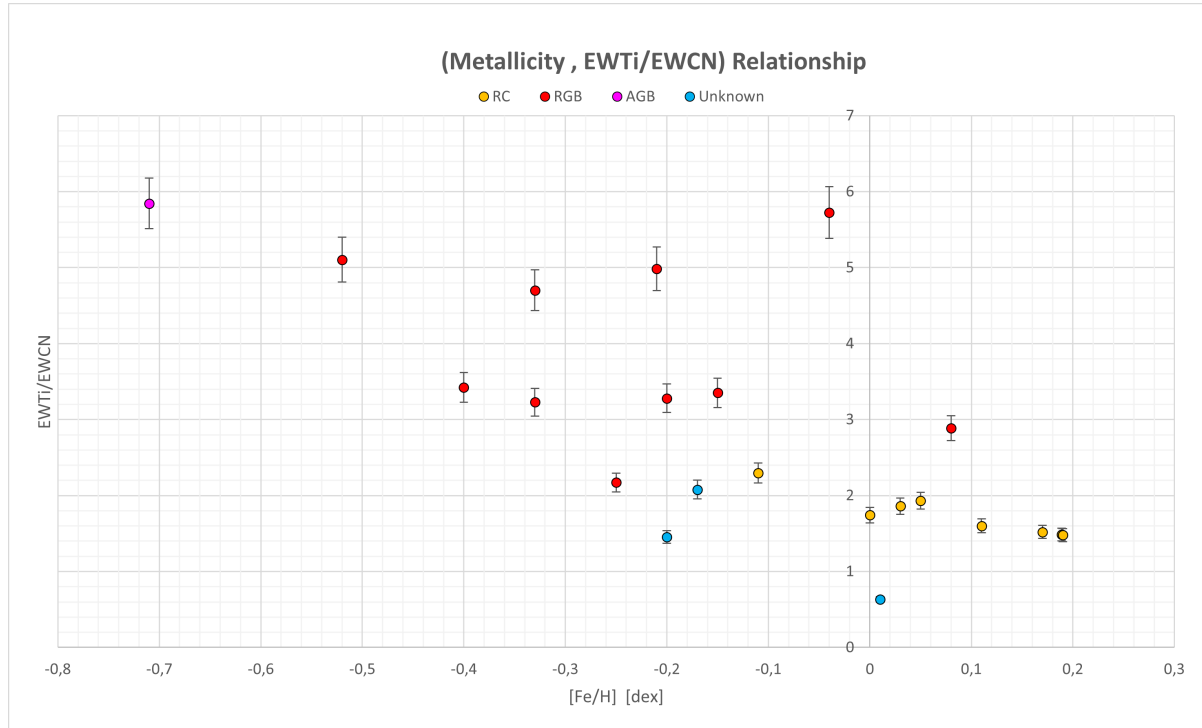


Figure 63: Quotient $\frac{\overline{EW}_{Ti}}{\overline{EW}_{CN}}$ as a function of metallicity [Fe/H] for RC, RGB, AGB and unknown stars.

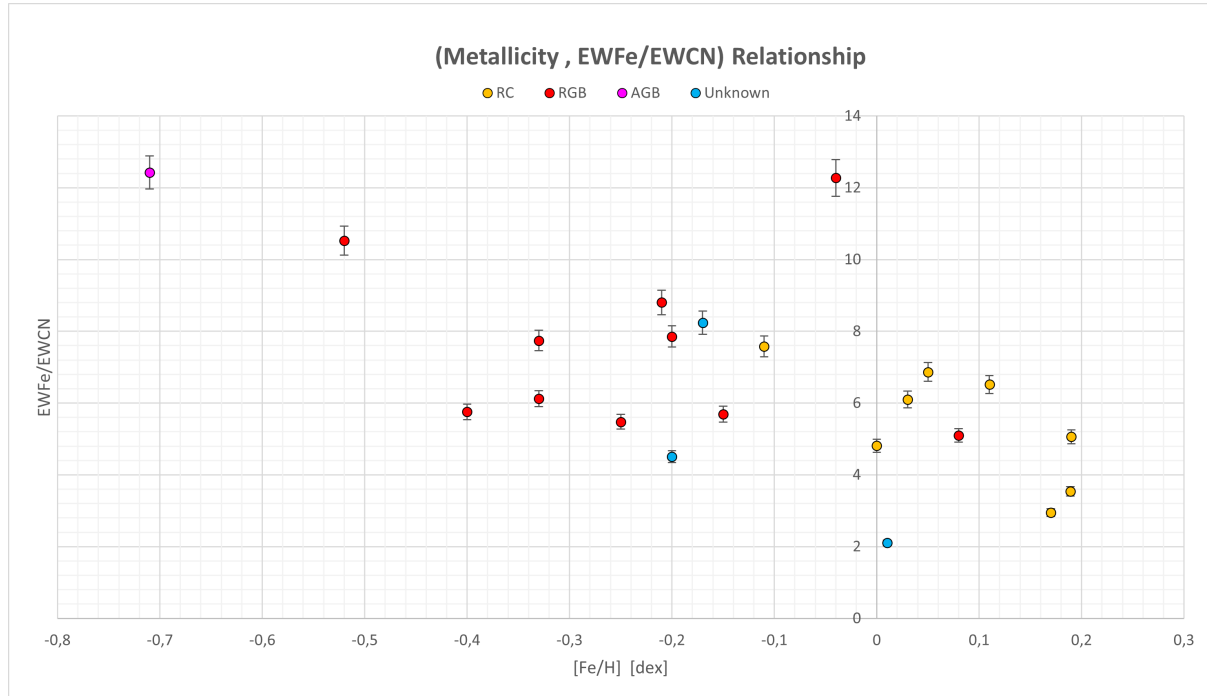


Figure 64: Quotient $\frac{\overline{EW}_{Fe}}{\overline{EW}_{CN}}$ as a function of metallicity [Fe/H] for RC, RGB, AGB and unknown stars.

7.3.2. Surface gravity $\log(g)$

Figures 65 and 66 show the quotients $\frac{\overline{EW}_{Ti}}{\overline{EW}_{CN}}$ and $\frac{\overline{EW}_{Fe}}{\overline{EW}_{CN}}$ as a function of surface gravity $\log(g)$, respectively. At first glance, the most relevant information seen in those charts is that figure 65 insists again on $\frac{\overline{EW}_{Ti}}{\overline{EW}_{CN}} = 2.5$ as an important limit that separates RGB from RC stars and also indicates that the three unknown stars are not RC stars because they lie within a different $\log(g)$ range, what makes sense since, as was stated in section 2.8.2, RC stars have similar masses due to their conditions prior to the lifting of their degenerate cores during the helium flash and thus their $\log(g)$ values should be similar to each other. Furthermore, the reduced $\log(g)$ observed in the unknown stars is consistent with the previous assumption that they might actually be post-HB stars traveling up the AGB, for these stars are known to increase their size and continuously lose mass, what ends up reducing their surface gravity.

Additionally, another interesting and frustrating fact in figures 65 and 66 is that both of them raise the doubt about HD12929's misclassification again, for it appears within the RC group but now based on its $\log(g) = 2.57$.

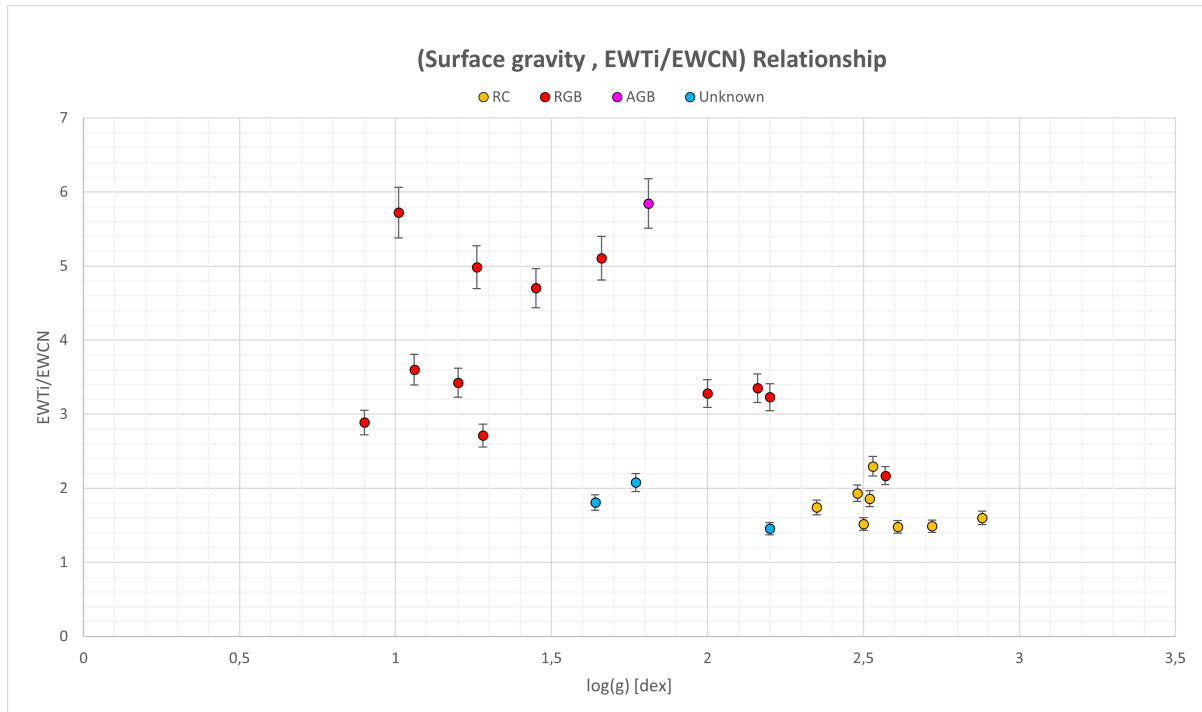


Figure 65: Quotient $\frac{\overline{EW}_{Ti}}{\overline{EW}_{CN}}$ as a function of surface gravity $\log(g)$ for RC, RGB, AGB and unknown stars.

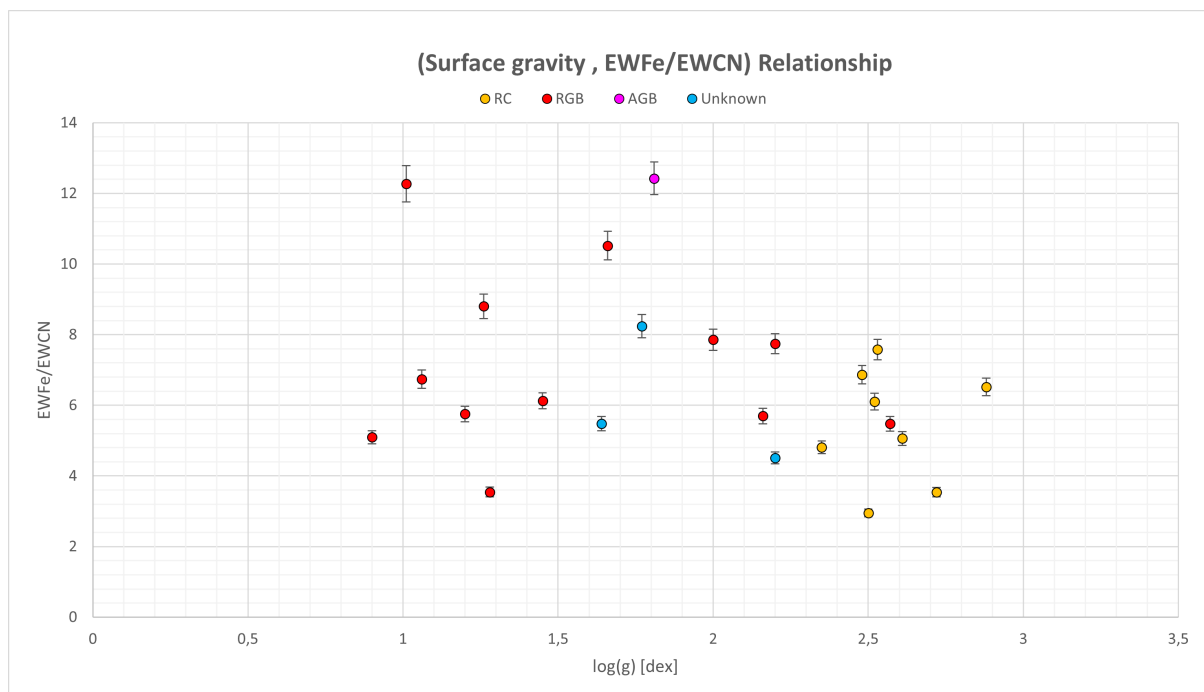


Figure 66: Quotient $\frac{\overline{EW}_{Fe}}{\overline{EW}_{CN}}$ as a function of surface gravity $\log(g)$ for RC, RGB, AGB and unknown stars.

7.3.3. Mass

Figures 67 and 68 show the quotients $\frac{\overline{EW}_{Ti}}{\overline{EW}_{CN}}$ and $\frac{\overline{EW}_{Fe}}{\overline{EW}_{CN}}$ as a function of stellar mass, respectively. Although figure 67 shows once again the already known $\frac{\overline{EW}_{Ti}}{\overline{EW}_{CN}} = 2.5$ limit, the new information that these two charts give is that, within the low-mass regime from $1 M_{\odot}$ to $3 M_{\odot}$ (where RC stars live due to their previously degenerated cores, as was said in section 2.8.2), RGB and RC stars with the same stellar mass exhibit different values for the quotients $\frac{\overline{EW}_{Ti}}{\overline{EW}_{CN}}$ and $\frac{\overline{EW}_{Fe}}{\overline{EW}_{CN}}$, being those of RC stars always less than those of RGB stars with the same mass. Moreover, in those figures the two unknown stars do not appear close to the RC stars nor to the RGB stars but lie within an intermediate mass range that suggests again that their evolutionary state is neither RC nor RGB.

What figures 67 and 68 look to be confirming is that, as [5] theorized and as was explained in section 2.9, there seems to be a clear spectroscopic difference between RC and RGB stars related to the CN content of the stars' photosphere, what is, to say the least, a perplexing result. According to classical low-mass stellar evolution theory, there should not be any spectroscopic difference between these two groups of stars since what differentiates them are the nuclear fusion processes taking place at their cores and, supposedly, there has not been enough time for the stars' photospheres to notice those changes, at least between those two evolutionary states. Given that the only process that RGB stars have—in theory—gone through is the first dredge-up (the convective process that carries the by-products of H core-burning to the surface), there is no way in which the surface's C concentration could have been increased, for their cores fuse hydrogen into helium via the CNO cycle, which uses C as a mere catalyst, thereby maintaining its concentration approximately constant. When the temperature gets high enough to "lift" the low-mass star's core's degeneracy, the triple alpha process begins in the abrupt way known as the "helium flash" and the star begins to fuse He into C, but, in theory, that does not become noticeable in the star's photosphere until the star gets to the AGB, point at which the second and third dredge-up occur and the by-products of the He core-burning rise to the surface, being N and C amongst them. In consequence, what this could mean is that there could exist some non-canonical convection mixing between the two evolutionary states, which seems to be more efficient for smaller stars (as figures 67 and 68 reveal) and provokes a noticeable spectroscopic difference that current low-mass stellar evolution theory is unable to explain. This could be due to some nucleosynthesis or convection mechanism triggered by the violent helium flash, but more research on this topic—as well as on the unknown/misclassified stars—is definitely needed to shed some light on how this spectroscopic difference between RC and RGB stars arises.

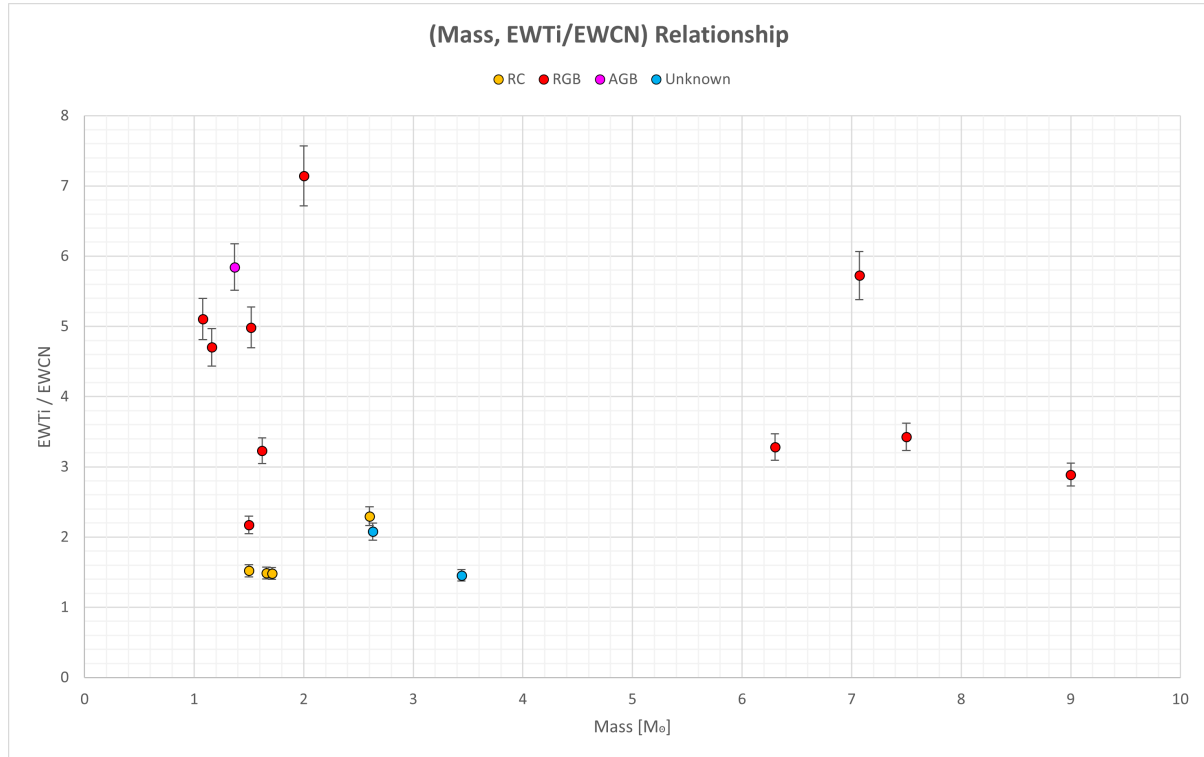


Figure 67: Quotient $\frac{\overline{EW}_{Ti}}{\overline{EW}_{CN}}$ as a function of the star's mass for RC, RGB, AGB and unknown stars.

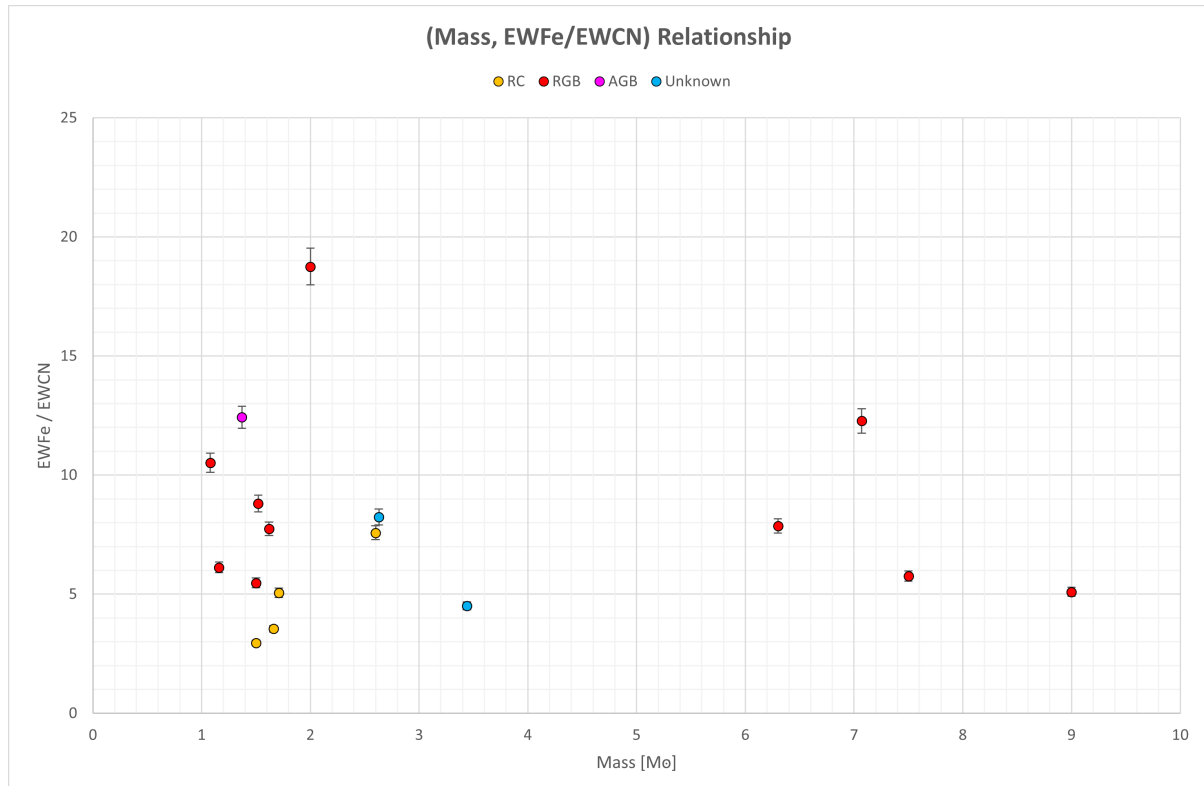


Figure 68: Quotient $\frac{\overline{EW}_{Fe}}{\overline{EW}_{CN}}$ as a function of the star's mass for RC, RGB, AGB and unknown stars.

7.4. 3D analysis

As has already been seen in sections 7.1, 7.2 and 7.3, there are some graphs in which the unknown stars appear mixed with RC stars, some graphs in which they appear mixed with RGB stars and some graphs in which they clearly seem to be a different group, what leads to think that the 2D way in which the relationships between the stellar parameters have been analysed so far is clearly not enough and that more of the stars' degrees of freedom must be studied at the same time if the difference between the evolutionary states is expected to be clarified. With this in mind, a 3D plot of the stars' $B - V$ index, M_V and $\frac{\overline{EW}_{Ti}}{\overline{EW}_{CN}}$ is shown in figure 69, whose top, lateral and bottom views are explored in greater depth in figures 70, 71 and 72, respectively. This "3D Hertzsprung-Russell space" (hereinafter "3D HR space") results from adding the dimension $\frac{\overline{EW}_{Ti}}{\overline{EW}_{CN}}$ to the classical 2D HR diagram and, at least at first glance, is a promising result that seems to be able to distinguish between RC and RGB stars by spectroscopic variables alone ($B - V$, M_V and $\frac{\overline{EW}_{Ti}}{\overline{EW}_{CN}}$), for it is possible to say that, at least within this sample of stars, the RGB seems to be the clump of stars within the zone delimited by the ranges $B - V = [1.5, 1.7]$, $M_V = [-4.5, 0.5]$ and $\frac{\overline{EW}_{Ti}}{\overline{EW}_{CN}} = [2.5, 10.5]$ in the 3D HR space, while the RC seems to be the clump of stars within the zone delimited by the ranges $B - V = [0.95, 1.25]$, $M_V = [0.5, 1.5]$ and $\frac{\overline{EW}_{Ti}}{\overline{EW}_{CN}} = [1.0, 2.5]$ in that same 3D HR space. Furthermore, if the three unknown stars above the RC really are AGB stars (as their low M_V and their low $\frac{\overline{EW}_{Ti}}{\overline{EW}_{CN}}$ quotient imply), then it is even possible to say that the 3D HR space actually allows to distinguish between RGB, RC and AGB stars all at once; nonetheless, the main problem with this is star HD220009, which was the only AGB star found in literature and undoubtedly appears far from those three unknown stars, close to RGB stars. A further research into this star (this time using Google scholar) was done, but what was found actually worsened the situation: two papers, [21] and [22], that classify HD220009 as a RC star and as a RGB star, respectively; considering this, it is then impossible to assign a trustworthy evolutionary state to HD220009, but, at least based on the 3D HR space of figure 69, it is plausible that this star is in fact a RGB star.

On top of what has been previously said, it must also be noted that another great feature of the 3D HR space is the fact that all RC stars seem to pile into a very small zone in the $(\frac{\overline{EW}_{Ti}}{\overline{EW}_{CN}}, M_V)$ plane, defined by the ranges $M_V = [0.6, 1.2]$ and $\frac{\overline{EW}_{Ti}}{\overline{EW}_{CN}} = [1.0, 2.5]$, as can be appreciated in subfigure 3 of figure 71 (or in figure 57, which is the same but more detailed). There are, however, two main stars that must be investigated further in order to be able to affirm this with confidence: the aforementioned HD12929 and the unknown star below the RC, HD95405. Although HD12929's location in the 2D graphs was very confusing given that it always seemed to lie within the ranges of RC stars, in the 3D HR space this confusion is not so dramatic since HD12929 now can be separated thanks to

its M_V , thus appearing to belong to the 3D RGB, but still lying very close to the 3D RC. In the case of HD95405, a first impression may lead to think that it is a RC star because it appears just below the RC of the classical 2D HR diagram (figure 23 or subfigure 1 of figure 69) and just a little away from the RC as viewed from the $(\frac{\overline{EW}_{Ti}}{\overline{EW}_{CN}}, M_V)$ plane (figure 57 or subfigure 3 of figure 69), but this is hard to believe blindly since HD95405 is actually the only studied star with $\frac{\overline{EW}_{Ti}}{\overline{EW}_{CN}} < 1$ (actually 0.63), meaning it has a lot of C content compared to RC stars, which do not go below $\frac{\overline{EW}_{Ti}}{\overline{EW}_{CN}} = 1.45$. As was said in section 2.8.2, RC stars' properties do not vary much since their initial masses prior to the helium flash were alike, thus rising the question of what the evolutionary status of HD95405 might be, for it cannot be an AGB star —like the other three unknown stars were assumed to be— given its big M_V . A possible explanation to this could be that, unlike the other three unknown stars, HD95405 is actually a non-classical carbon star, which are believed to be binary stars composed of a white dwarf and a red giant star that accreted carbon-rich material when it was still a MS star from the planetary nebula left behind by its companion, yet a detailed analysis of this star is definitely required to properly understand why it has such mixed properties. In any case, however, the 3D HR space clearly gives hope with regards to the possibility of differentiating RC and RGB stars with spectroscopic methods alone, what rises the big question of what kind of events related to the CN-cycle of stars could be leading to this difference, for classical stellar evolution theory seems not to be addressing this problem at all.

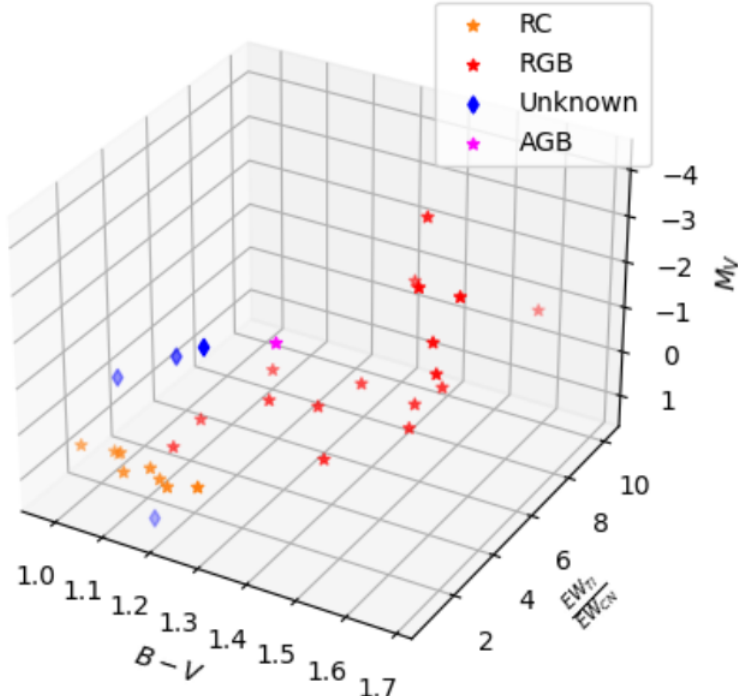


Figure 69: 3D Hertzsprung-Russell space constructed by adding the $\frac{\overline{EW}_{Ti}}{\overline{EW}_{CN}}$ dimension to the classical 2D Hertzsprung-Russell diagram.

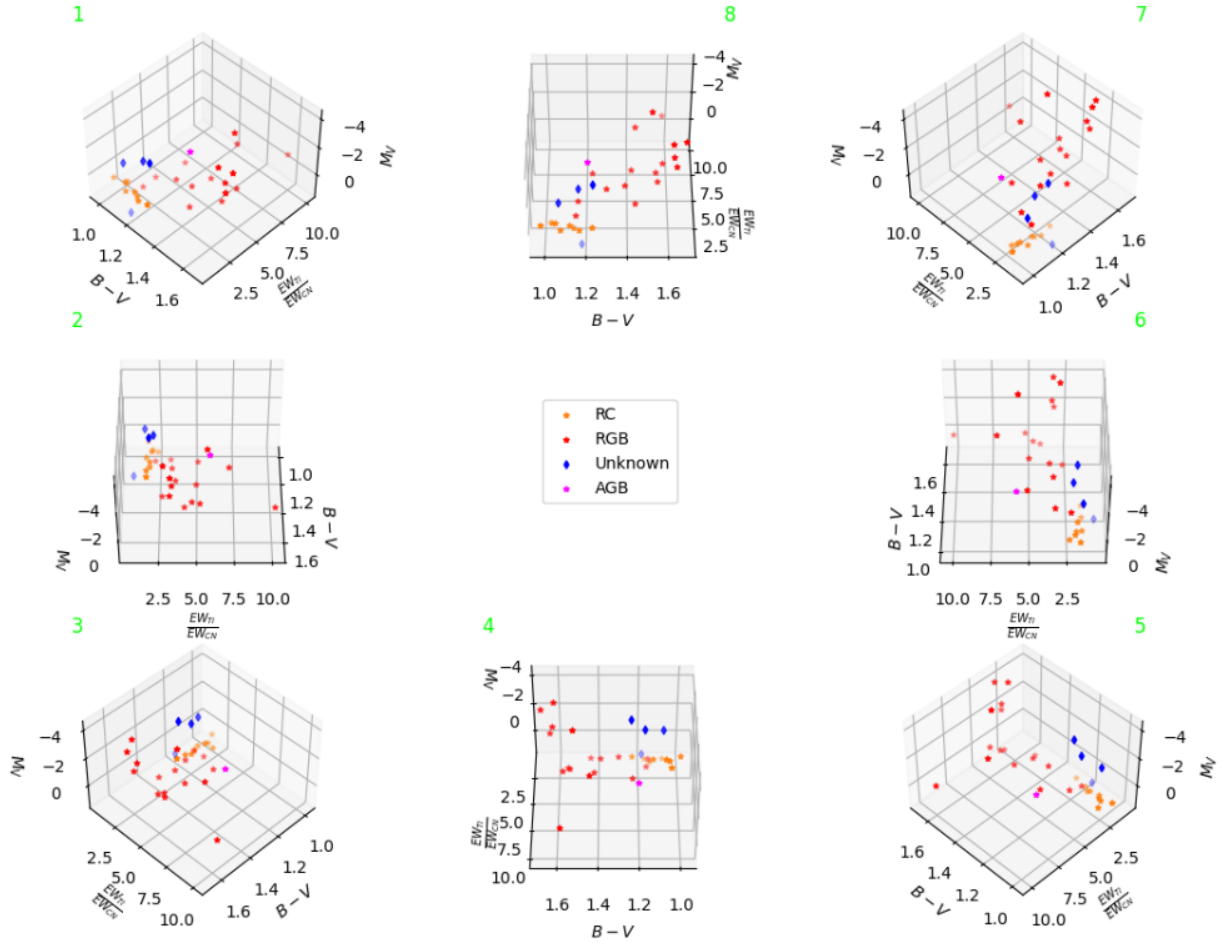


Figure 70: Rotation of the top view of the 3D Hertzsprung-Russell space of figure 69 from a point of view with a $+45^\circ$ angle with respect to the $(B - V, \frac{EW_{Ti}}{EW_{CN}})$ plane. The sequence of subfigures (from 1 to 8) follows the clockwise rotation of the space around the M_V axis (i.e., the rotation vector goes in the $-\hat{M}_V$ direction) with intervals of $+45^\circ$.

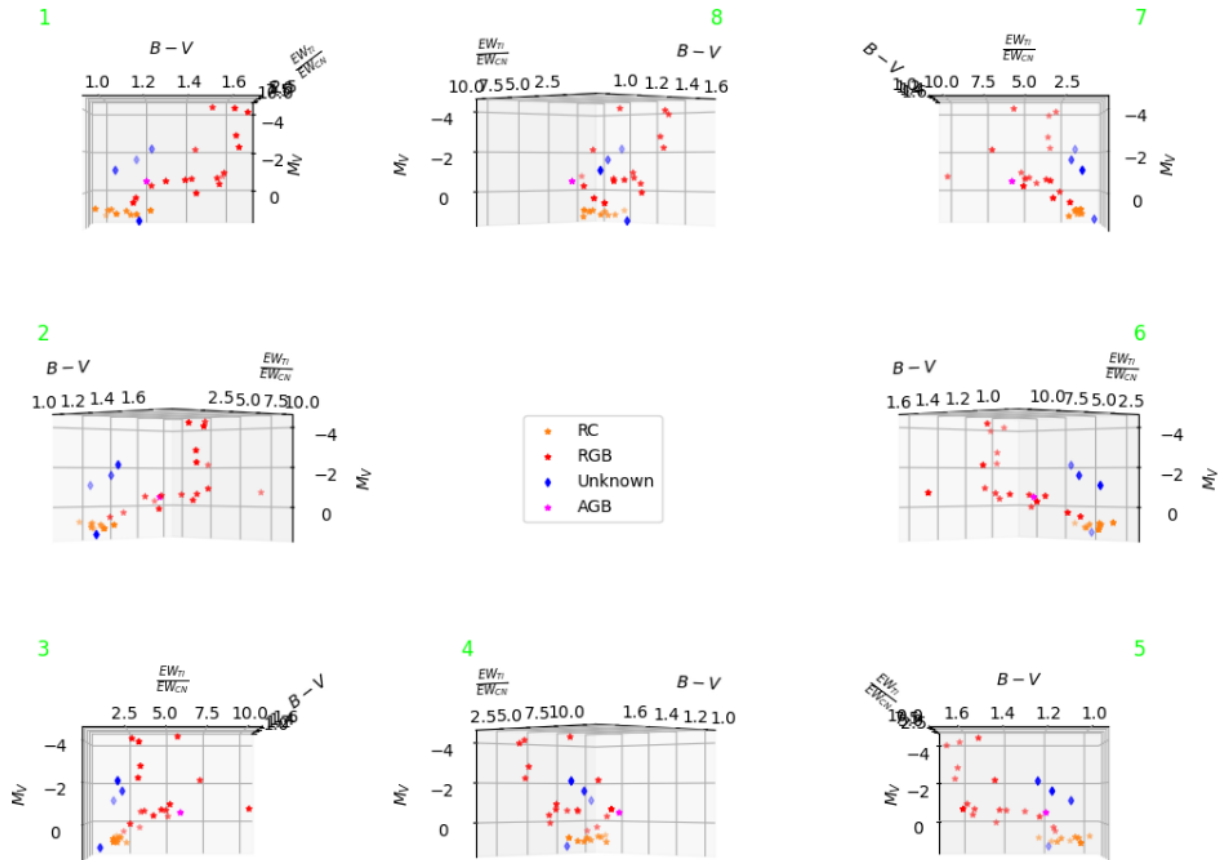


Figure 71: Rotation of the lateral views of the 3D Hertzsprung-Russell space of figure 69 from a point of view parallel to the $(B - V, \frac{EW_{Ti}}{EW_{CN}})$ plane. The sequence of subfigures (from 1 to 8) follows the clockwise rotation of the space around the M_V axis (i.e., the rotation vector goes in the $-\hat{M}_V$ direction) with intervals of $+45^\circ$.

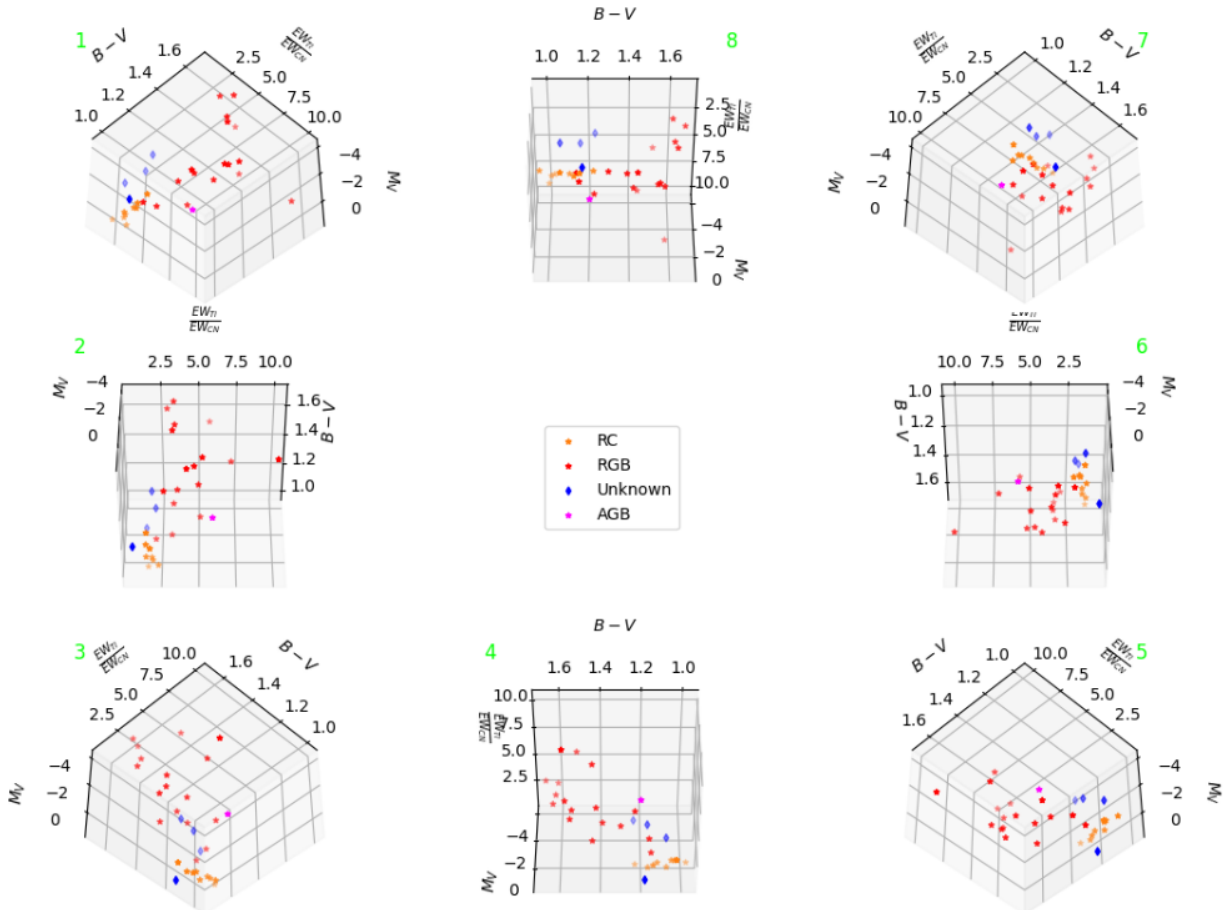


Figure 72: *Rotation of the bottom view of the 3D Hertzsprung-Russell space of figure 69 from a point of view with a -45° angle with respect to the $(B - V, \frac{EWT_i}{EWC_N})$ plane. The sequence of subfigures (from 1 to 8) follows the clockwise rotation of the space around the M_V axis (i.e., the rotation vector goes in the $-\hat{M}_V$ direction) with intervals of $+45^\circ$.*

8. Conclusion

After having measured the EW s of 4 Fe I, 1 Ti I and 4 CN I spectral lines of 9 RC, 17 RGB, 1 AGB and 4 unknown-evolutionary-state stars within the [7400 Å, 7500 Å] wavelength range, it was possible to collect evidence that supports the theory that the \overline{EW} of the CN I molecule could be the spectroscopic parameter that allows to distinguish the spectra of RC stars from those of RGB stars without the need to resort to chemical or asteroseismological methods. In all of the plots obtained, the limit $\frac{\overline{EW}_{Ti}}{\overline{EW}_{CN}} = 2.5$ proved to be a powerful tool to differentiate the evolutionary states, for all stars that are confirmed to belong to the RC fell within the range $\frac{\overline{EW}_{Ti}}{\overline{EW}_{CN}} < 2.5$ and all confirmed RGB stars but one (HD12929) fell within the range $\frac{\overline{EW}_{Ti}}{\overline{EW}_{CN}} > 2.5$; in addition, when this powerful quotient is combined with another quotient of EW s, the result is an amazing chart that differentiates the two evolutionary states so clearly that even a wide space forms between them, as figures 60, 61 and 62 show. This must, however, be taken with caution, for it must not be forgotten that the sample of stars was too small to completely "prove" the proposal (although it is possible to say that no counterexamples could be found) and that there are still 4 unknown stars, a possibly misclassified star (HD220009) and a dubious boundary star (HD12929) that need to be studied and properly classified in order to give validity to the spectroscopic differentiation method proposed in this dissertation, which consists of a 3D Hertzsprung-Russell space (figure 69) obtained by adding the $\frac{\overline{EW}_{Ti}}{\overline{EW}_{CN}}$ dimension to the classical 2D Hertzsprung-Russell diagram. Three of the four unknown stars could be classical AGB carbon stars that produce C in their cores based on their low M_V and their low $\frac{\overline{EW}_{Ti}}{\overline{EW}_{CN}}$ quotient, and the other unknown star (HD95405) could be a non-classical carbon star that obtained its C from a binary companion, but, in any case, the greater problem of explaining the greater intensity of CN I spectral lines in confirmed RC stars still remains. Classical low-mass stellar evolution theory's first dredge-up cannot be responsible for the increase in C concentration in RC stars since the by-products of the CNO cycle (which has been thought to be the dominant energy-production process before the helium flash) do not include C, and the second and third dredge-ups cannot be the reason either since they happen after the star has already gone through the HB and is traveling up the AGB. The triple alpha process triggered by the lifting of the core's degeneracy during the helium flash does produce C, but that C has always been thought to not get to the star's photosphere, thus leaving no explanation for how RC stars might have obtained that extra C concentration. The answer could reside in some still not-well-understood or not-yet-formulated non-canonical convection mixing between the two evolutionary states caused by the explosive helium flash, but more research on the subject is definitely required.

9. Future work

Although this dissertation gives hope with regards to the possibility of being able to differentiate between stars that fuse helium in their cores (RC stars) and those that do not (RGB stars) with spectroscopic methods alone, it has many limitations that must be surpassed in order give the method strength and credibility. The first of them is, of course, the need to clarify the evolutionary status of HD12929, HD220009 and the 4 unknown stars, what could be achieved by recurring to the classical asteroseismological and chemical methods. Nevertheless, even if the evolutionary status of all 6 stars is clarified, much more stars need to be included in the study because an observed behavior within a sample of only 31 stars is definitely not enough evidence to give a general conclusion, for 31 stars is nothing compared to the ridiculous amount of stars out there.

Another thing to improve is the efficiency of the whole process, since the manual calculation of the EWs with Microsoft Excel was extremely slow. With regards to this problem, equation 6.20 offers a much easier way that, if automated using Python or another programming language, could compute EWs incredibly fast, hence allowing to study other CN I spectral lines at shorter wavelengths faster and thus reaching more general conclusions (although a problem that might arise is that shorter wavelengths contain less useful CN I lines, as [7] already suggested). If this is coupled with the use of more accurate data such as GAIA DR3's and with the use of machine learning techniques such as DBSCAN [23], then this study could achieve the accuracy and range required to really produce an impact in astronomy, since it became clear that the proposed 3D Hertzsprung-Russell space seems to be a much clearer way to visualize the different stellar evolution stages than the classical 2D Hertzsprung-Russell diagram. If $B-V$, M_V and $\frac{EW_{Ti}}{EW_{CN}}$ are coupled with other stellar parameters (such as $\log(g)$, $[Fe/H]$ and mass), then it could be possible to use the DBSCAN algorithm to detect clusterings in a multi-parameter "Hertzsprung-Russell hyperspace", thus allowing to unequivocally distinguish between the different stellar stages.

And lastly, it is absolutely necessary to do an in-depth research into the latest advances in low-mass stellar evolution theory, for the results of this dissertation have clearly shown that classical stellar evolution theory is not being able to provide appropriate answers to the problem of the stronger CN I lines in RC stars, what could mean that perhaps the most important thing to do is to ask ourselves the appropriate questions.

References

- [1] Hansen, C., Kawaler, S., & Trimble, V. 2004, *Stellar interiors: physical principles, structure and evolution*, (2nd ed.), Springer-Verlag, 340.
- [2] Bastien, F., Stassun, K., Basri, G., & Pepper, J. 2015, *A granulation "flicker"-based measure of stellar surface gravity*, The Astrophysical Journal Letters, **818**, 43. <https://doi.org/10.3847/0004-637X/818/1/43>
- [3] Nataf, D., Udalski, A., Gould, A., Fouqué, P., & Stanek, K. 2010, *The Split Red Clump of the Galactic Bulge from OGLE-III*, The Astrophysical Journal Letters, **721**, L28–L32. <https://doi.org/10.1088/2041-8205/721/1/L28>
- [4] Ree, C., Yoon, S., Rey, S., & Lee, Y. 2002, *Omega Centauri, A Unique Window into Astrophysics*, (1st ed. Astronomical Society of the Pacific), **265**, 101.
- [5] Masseron, T., & Hawkins, K. 2017, *The spectroscopic indistinguishability of red giant branch and red clump stars*, Astronomy & Astrophysics, **597**, L3. <https://doi.org/10.1051/0004-6361/201629938>
- [6] Powell, R. 2011, *The Hertzsprung Russel Diagram*, <http://www.atlasoftheuniverse.com/hr.html>
- [7] Oostra, B., & Vargas, P. 2021, *The differential redshift of titanium lines in K stars*, (under review).
- [8] Lithopsian. 2016, *The evolutionary track of a solar mass, solar metallicity, star from main sequence to post-AGB*, https://en.wikipedia.org/wiki/Horizontal_branch#/media/File:Evolutionary_track_1m.svg
- [9] Perryman, M. 2021, *Hipparcos satellite: testing in the Large Solar Simulator*, ESTEC, <https://commons.wikimedia.org/wiki/File:Hipparcos-testing-estec.jpg>
- [10] University of Iowa. 2017, *Imaging the Universe: Stellar Parallax*, <http://astro.physics.uiowa.edu/ITU/glossary/stellar-parallax/>
- [11] Carroll, B. & Ostlie, D. 2017, *An Introduction to Modern Astrophysics*, (2nd ed.), Cambridge University Press.

- [12] Dintsiros, N., & Artemi, S., & Polatoglou, H. 2018, *Evaluating Stars Temperature Through the B-V Index Using a Virtual Real Experiment from Distance: A Case Scenario for Secondary Education*. International Journal of Online and Biomedical Engineering (iJOE), **14(01)**, pp. 162–178. <https://doi.org/10.3991/ijoe.v14i01.7842>
- [13] Zombeck, M. 1990, *CHandbook of Space Astronomy and Astrophysics*, (2nd ed.), Cambridge University Press, 105.
- [14] Girardi, L. 2016, *Red Clump Stars*, The Annual Review of Astronomy and Astrophysics, **54**, 95 - 133. <https://doi.org/10.1146/annurev-astro-081915-023354>
- [15] van Leeuwen, F. 2007, *Validation of the new Hipparcos reduction*, Astronomy & Astrophysics, **474**, 2, 653-664. <https://doi.org/10.1051/0004-6361:20078357>
- [16] Bagnulo, S., Jehin, E., Ledoux, C., Cabanac, R., Melo, C., Gilmozzi, R. & ESO Paranal Science Operations Team. 2003, *The UVES Paranal Observatory Project: A Library of High- Resolution Spectra of Stars across the Hertzsprung-Russell Diagram*, The Messenger, **114**, 10-14.
- [17] Strassmeier, K., Ilyin, I., Järvinen, A., Weber, M., Woche, M., Barnes, S. I., Bauer, S. -M., Beckert, E., Bittner, W., Bredthauer, R., Carroll, T. A., Denker, C., Dionies, F., DiVarano, I., Döscher, D., Fechner, T., Feuerstein, D., Granzer, T., Hahn, T., Harnisch, G., Hofmann, A., Lesser, M., Paschke, J., Pankratow, S., Plank, V., Plüsckhe, D., Popow, E. & Sablowski, D. 2015, *PEPSI: The high-resolution échelle spectrograph and polarimeter for the Large Binocular Telescope*, Astronomische Nachrichten, **336**, 4. <https://doi.org/10.1002/asna.201512172>
- [18] Ochsenbein F. et. al. 2000, *The VizieR database of astronomical catalogues*, Astronomy & Astrophysics, **143**, 23. <https://doi.org/10.1051/aas:2000169>

This research has made use of the VizieR catalogue access tool, CDS, Strasbourg, France (DOI : 10.26093/cds/vizier). The original description of the VizieR service was published in 2000, A&AS 143, 23.

- [19] Wenger, M., Ochsenbein, F., Egret, D., Dubois, P. Bonnarel, F., Borde, S., Genova, F., Jasniewicz, G., Laloë, S., Lesteven, S. & Monier R. 2000, *The SIMBAD astronomical database. The CDS reference database for astronomical objects*, Astronomy & Astrophysics, **143**, 9-22. <https://doi.org/10.1051/aas:2000332>

This research has made use of the SIMBAD database, operated at CDS, Strasbourg, France.

- [20] Ryabchikova, T., Piskunov, N., Kurucz, R., Stempels, H., Heiter, U., Pakhomov, Yu. & Barklem, P. 2015, *A major upgrade of the VALD database*, The Royal Swedish Academy of Sciences, **90**, 5. <https://doi.org/10.1088/0031-8949/90/5/054005>

This work has made use of the VALD database, operated at Uppsala University, the Institute of Astronomy RAS in Moscow, and the University of Vienna.

- [21] Alves, D. 2000, *K-Band Calibration of the Red Clump Luminosity*, The Astrophysical Journal, **539**, 732. <https://doi.org/10.1086/309278>
- [22] Brown, J. & Sneden, C. & Lambert, D. & Dutchover, E. 1989, *A Search for Lithium-rich Giant Stars*, The Astrophysical Journal Supplement Series, **71**, 293. <https://doi.org/10.1086/191375>
- [23] Ester, M. & Kriegel, H. & Sander, J. & Xu, X. 1996, *A density-based algorithm for discovering clusters in large spatial databases with noise*, AAAI Press, 226-231.
- [24] Laney, C. & Joner, M. v Pietrzyński, G. 2012 *A new Large Magellanic Cloud K-band distance from precision measurements of nearby red clump stars*, Monthly Notices of the Royal Astronomical Society, **419**, 1637-1641. <https://doi.org/10.1111/j.1365-2966.2011.19826.x>
- [25] Valentini, M. & Munari, U. 2010, *A spectroscopic survey of faint, high-Galactic-latitude red clump stars. I. The high resolution sample*, Astronomy & Astrophysics, **522**, A79. <https://doi.org/10.1051/0004-6361/201014870>
- [26] Gontcharov, G. 2008, *Red giant clump in the Tycho-2 catalogue*, Astronomy Letters, **34**, 785-796. <https://doi.org/10.1134/S1063773708110078>
- [27] Gontcharov, G. 2011, *The Red Giant Branch in the Tycho-2 Catalogue*, Astronomy Letters, **37**, 707-710. <https://doi.org/10.1134/S1063773711090040>
- [28] Abia, C., Palmerini, S., Busso, M. & Cristallo, S. 2012, *Carbon and oxygen isotopic ratios in Arcturus and Aldebaran*, Astronomy & Astrophysics, **548**, 12. <https://doi.org/10.1051/0004-6361/201220148>
- [29] Rebull, L., Carlberg, J. & Gibbs, J. 2015, *On infrared excesses associated with Li-rich K giants*, The Astronomical Journal, **150**, 123. <https://doi.org/10.1088/0004-6256/150/4/123>
- [30] Cardiel, N., Zamorano, J., Bará, S., Cabello, C. & Gallego, J. 2021, *Synthetic RGB photometry of bright stars: definition of the standard photometric system and UCM library of spectrophotometric spectra*, Monthly Notices of the Royal Astronomical Society, **504**, 3730-3748. <https://doi.org/10.1093/mnras/stab997>

- [31] Lagadec, E., Verhoelst, T., Mékarnia, D., Suárez, O., Bendjoya, P. & Szczerba, R. 2011, *A mid-infrared imaging catalogue of post-asymptotic giant branch stars*, Monthly Notices of the Royal Astronomical Society **417**, 32-92. <https://doi.org/10.1111/j.1365-2966.2011.18557.x>
- [32] Gray, D. & Kaur, T. 2019, *A Recipe for Finding Stellar Radii, Temperatures, Surface Gravities, Metallicities, and Masses Using Spectral Lines*, The Astrophysical Journal, **882**, 148. <https://doi.org/10.3847/1538-4357/ab2fce>
- [33] Edvardsson, B. 1988, *Spectroscopic surface gravities and chemical compositions for 8 nearby single sub-giants*, Astronomy and Astrophysics, **190**, 148-166.
- [34] Lee, B., Han, I., Park, M., Mkrtichian, D., Hatzes, A. & Kim, K. 2014, *Planetary companions in K giants Cancri, Leonis, and Ursae Minoris*, Astronomy & Astrophysics, **566**, 7. <https://doi.org/10.1051/0004-6361/201322608>
- [35] Massarotti, A., Latham, D., Stefanik, R. & Fogel, J. 2007, *Rotational and radial velocities for a sample of 761 Hipparcos giants and the role of binarity*, The Astronomical Journal, **135**, 209. <https://doi.org/10.1088/0004-6256/135/1/209>
- [36] Luck, R. 2015, *Abundances in the local region. I, G and K giants*, The Astronomical Journal, **150**, 88. <https://doi.org/10.1088/0004-6256/150/3/88>
- [37] Park, S., Kang, W., Lee, J. & Lee, S. 2013, *Wilson-Bappu effect: extended to surface gravity*, The Astronomical Journal, **146**, 73. <https://doi.org/10.1088/0004-6256/146/4/73>
- [38] Dominy, J. 1984, *The chemical composition and evolutionary state of the early stars*, Astrophysical Journal Supplement Series, **55**, 27-43.
- [39] Guenther, D. 2000, *Evolutionary Model and Oscillation Frequencies for α Ursae Majoris: A Comparison with Observations*, The Astrophysical Journal, **530**, L45. <https://doi.org/10.1086/312473>
- [40] Ramírez, I. & Allende, C. 2011, *Fundamental parameters and chemical composition of Arcturus*, The Astrophysical Journal, **743**, 135. <https://doi.org/10.1088/0004-637X/743/2/135>
- [41] Farr, W., Pope, B., Davies, G., North, T., White, T., Barret, J., Miglio, A., Lund, M., Antoci, V. & Andersen, M. 2018, *Aldebaran b's Temperate Past Uncovered in Planet Search Data*, The Astrophysical Journal Letters, **865**, L20. <https://doi.org/10.3847/2041-8213/aadfde>

- [42] Strassmeier, K., Ilyin, I. & Weber, M. 2018, *Gaia benchmark stars and other M-K standards*, *Astronomy & Astrophysics*, **612**, A45. <https://doi.org/10.1051/0004-6361/201731633>
- [43] Jofré, E., Petrucci, R., Saffe, C., Saker, L., Artur de la Villarmois, E., Chavero, C., Gómez, M. & Mauas P. 2015, *Stellar parameters and chemical abundances of 223 evolved stars with and without planets*, *Astronomy & Astrophysics*, **574**, A50. <https://doi.org/10.1051/0004-6361/201424474>
- [44] Cruzalèbes, P., Jorissen, A., Rabbia, Y., Sacuto, S., Chiavassa, A., Pasquato, E., Plez, B., Eriksson, K., Spang, A. & Chesneau, O. 2013, *Fundamental parameters of 16 late-type stars derived from their angular diameter measured with VLTI/AMBER*, *Monthly Notices of the Royal Astronomical Society*, **434**, 437-450. <https://doi.org/10.1093/mnras/stt1037>
- [45] Jones, K. & Robinson, R. 1992, *Spectroscopic investigation of cool giants and the authenticity of their reported microwave emission*, *Monthly Notices of the Royal Astronomical Society*, **256**, 535-544. <https://doi.org/10.1093/mnras/256.3.535>
- [46] McWilliam, A. 1990, *High-Resolution Spectroscopic Survey of 671 GK Giants. I. Stellar Atmosphere Parameters and Abundances*, *Astrophysical Journal Supplement*, **74**, 1075. <https://doi.org/10.1086/191527>
- [47] Tetzlaff, N., Neuhäuser, R. & Hohle, M. 2010, *A catalogue of young runaway Hipparcos stars within 3 kpc from the Sun*, *Monthly Notices of the Royal Astronomical Society*, **410**, 190-200. <https://doi.org/10.1111/j.1365-2966.2010.17434.x>
- [48] Soubiran, C., Le Campion, J., Brouillet, N. & Chemin, L. 2016, *The PASTEL catalogue: 2016 version*, *Astronomy & Astrophysics*, **591**, A118. <https://doi.org/10.1051/0004-6361/201628497>
- [49] Anderson, E. & Francis, Ch. 2012, *XHIP: An extended hipparcos compilation*, *Astronomy Letters*, **38**, 331-346. <https://doi.org/10.1134/S1063773712050015>
- [50] Stock, S., Reffert, S. & Quirrenbach, A. 2018, *VizieR Online Data Catalog: Stellar parameters of 372 giant stars*, *VizieR Online Data Catalog*. <https://ui.adsabs.harvard.edu/abs/2018yCat..3616003S>

A. How to calculate the uncertainties

Some of the astrometrical quantities ($B - V$ index, parallax plx , visual magnitude V) taken into account for this dissertation had their uncertainties given directly by the online libraries, whereas, in the case of the distance to the star D , the absolute visual magnitude M_V , the partition error of table 20, the average EWs of tables 50, 51 and 52 and the quotients of the EWs, the error (whose numerical values are not explicitly shown in the tables but were plotted as error bars in all graphs) can be calculated as will be shown below:

A.1. The distance to the star (D)

As is the case with many other variables, the error σ_D can be found by means of **the propagation formula**, which states that, for a given function $F = F_{(x,y,z,\dots)}$, the total propagated uncertainty σ_F due to the uncertainties of the independent variables $(\sigma_x, \sigma_y, \sigma_z, \dots)$ is given by

$$\sigma_F^2 \approx \left(\frac{\partial F}{\partial x}\right)^2 \sigma_x^2 + \left(\frac{\partial F}{\partial y}\right)^2 \sigma_y^2 + \left(\frac{\partial F}{\partial z}\right)^2 \sigma_z^2 + \dots \quad (\text{A.1})$$

Since the distance to the star is calculated with equation 2.2, the application of this formula gives

$$\sigma_D = \left(\frac{\partial D}{\partial (plx)}\right) \sigma_{plx} \quad (\text{A.2})$$

$$= \left(\frac{1000}{(plx)^2}\right) \sigma_{plx}, \quad (\text{A.3})$$

where σ_{plx} is the error in the parallax measurement, which was already given by the stellar catalogues.

A.2. The absolute visual magnitude (M_V)

In this case, equation A.1 was also applied to equation 2.5 to find that

$$\sigma_{M_V} = \left[\left(\frac{\partial M_V}{\partial V} \sigma_V \right)^2 + \left(\frac{\partial M_V}{\partial D} \sigma_D \right)^2 \right]^{\frac{1}{2}} \quad (\text{A.4})$$

$$= \left[\sigma_V^2 + \left(\frac{-5\sigma_D}{D \ln(10)} \right)^2 \right]^{\frac{1}{2}}, \quad (\text{A.5})$$

where σ_m is the visual magnitude's error and D and σ_D are the distance to the star and its error, respectively.

A.3. The partition error

The errors in table 20 were calculated as simply the percentage of the distance that its error represents. Thus, if the error in the distance is σ_D and the distance is D , its partition error is given by

$$\sigma_{\text{partition}} = \frac{\sigma_D}{D} * 100\% \quad (\text{A.6})$$

A.4. The Equivalent Width (EW)

As was explained in section 6, almost all of the EWs were calculated by means of a parabolic regression with the maximum number of data points that gave the highest R^2 . If that number of points is labeled "X", then the EW's error can be found by means of plotting 2 parabolas, one with X-8 data points (-4 at the lower end and -4 at the upper end) and one with X+8 data points (+4 at the lower end and +4 at the upper end), as is shown in figure 73 for the specific case of Unukalhai's line Fe I 7411,1544 Å. This results in two gaussian regressions that enclose the best-fit regression shown in cyan in figure 74 and whose EWs are considered the lower and upper errors of the EW. After doing that calculation for 30 spectral lines (the calculation for Unukalhai's line Fe I 7411,1544 Å is shown in figure 75), it was found that in no case the boundary regressions surpassed the best regression by more than 5% and hence it was decided to consider all EWs' errors as ±5%.

A.5. The average EW (\overline{EW})

Since the average EW of a given species is given by equation $\overline{EW} = \frac{1}{N} \sum_{i=1}^N EW_i$ (where N is the total number of the chemical species' lines, being 4 for Fe I and CN I, and 1 for

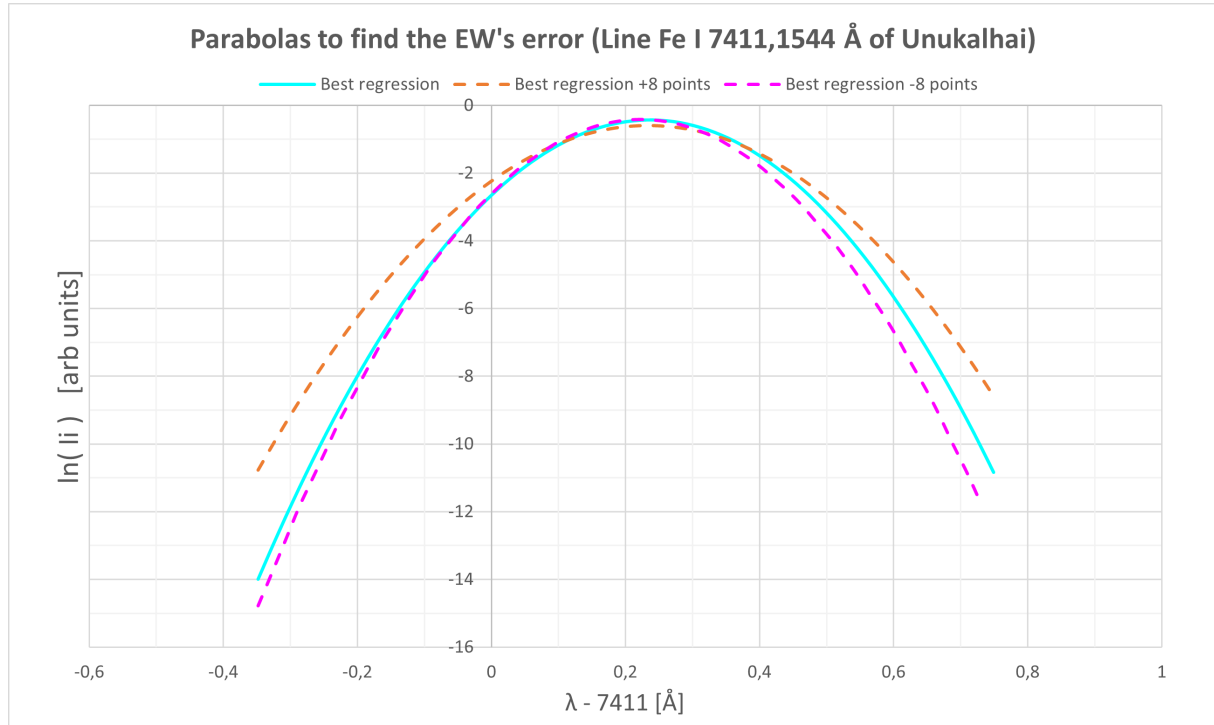


Figure 73: Boundary parabolas to estimate the EW's error. The cyan parabola is the best-fit regression with X points, while the orange one has $X+8$ points and the pink one $X-8$.

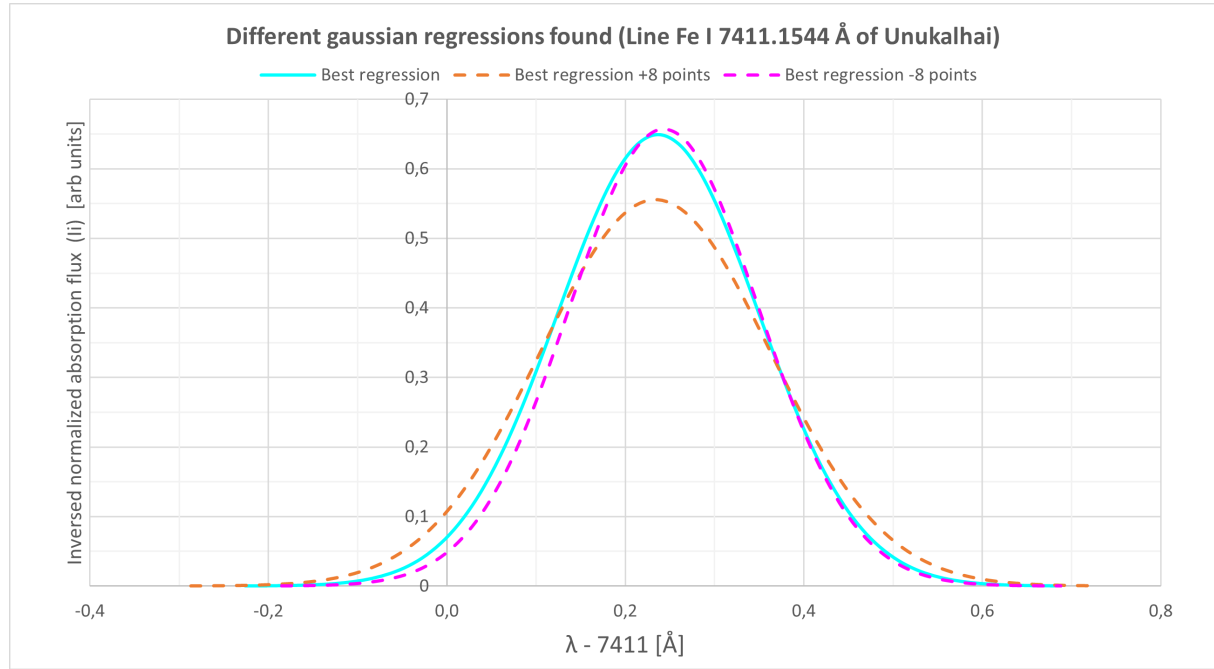


Figure 74: Boundary gaussian regressions used to find the EW's lower and upper limits. The pink parabola gives the upper limit, while the orange one gives the lower limit.

Ti I), then equation A.1 leads to

Gaussian regression	# of points	$\sigma [\text{\AA}]$	$\mu [\text{\AA}]$	EW [m\AA]	Percentage from best regression [%]
Pink	15	0,1065	0,2434	171,223	-4,18
Cyan	23	0,1123	0,2368	178,701	0
Orange	31	0,1288	0,2335	181,323	1,47

Figure 75: Example of the error found for Unukalhai's line Fe I 7411,1544 \AA from figures 73 and 74.

$$\sigma_{\overline{EW}} = \frac{1}{N} \left[\sum_{i=1}^N (\sigma_{EW_i})^2 \right]^{\frac{1}{2}}, \quad (\text{A.7})$$

but, since the uncertainty of the EW was assumed to be 5% (i.e., $\sigma_{EW_i} = \pm \frac{5}{100} EW_i = \pm \frac{1}{20} EW_i$, the error turns into

$$\sigma_{\overline{EW}} = \frac{1}{20N} \left[\sum_{i=1}^N (EW_i)^2 \right]^{\frac{1}{2}}. \quad (\text{A.8})$$

The error $\sigma_{\overline{EW}}$ for each chemical species for each star is thus

$$\sigma_{\overline{EW}_{\text{Fe}}} = \frac{1}{80} \left[\sum_{i=1}^4 (EW_{\text{Fe}_i})^2 \right]^{\frac{1}{2}} \quad (\text{A.9})$$

$$\sigma_{\overline{EW}_{\text{Ti}}} = \frac{1}{20} EW_{\text{Ti}_i} \quad (\text{A.10})$$

$$\sigma_{\overline{EW}_{\text{CN}}} = \frac{1}{80} \left[\sum_{i=1}^4 (EW_{\text{CN}_i})^2 \right]^{\frac{1}{2}} \quad (\text{A.11})$$

A.6. The quotients of EWs $\left(\frac{\overline{EW}_x}{\overline{EW}_y} \right)$

The error of the quotient of the average EW of two chemical species x and y, $\frac{\overline{EW}_x}{\overline{EW}_y}$, was also calculated by means of equation A.1, obtaining

$$\sigma \left(\frac{\overline{EW}_x}{\overline{EW}_y} \right) = \left[\left(\frac{\sigma_{\overline{EW}_x}}{\overline{EW}_y} \right)^2 + \left(\frac{\overline{EW}_x}{\overline{EW}_y^2} \sigma_{\overline{EW}_y} \right)^2 \right]^{\frac{1}{2}}, \quad (\text{A.12})$$

which, taking into account equation A.8, turns into

$$\sigma \left(\frac{\overline{EW}_x}{\overline{EW}_y} \right) = \frac{1}{20 \overline{EW}_y} \left[\frac{1}{N_x^2} \left(\sum_{i=1}^{N_x} EW_{x_i}^2 \right) + \frac{\overline{EW}_x^2}{N_y^2 \overline{EW}_y^2} \left(\sum_{i=1}^{N_y} EW_{y_i}^2 \right) \right]^{\frac{1}{2}}. \quad (\text{A.13})$$

Thus, the errors associated with the quotients in section 7.2 are:

$$\sigma \left(\frac{\overline{EW}_{Ti}}{\overline{EW}_{CN}} \right) = \frac{\overline{EW}_{Ti}}{80\overline{EW}_{CN}^2} \left[16\overline{EW}_{CN}^2 + \left(\sum_{i=1}^4 EW_{CN_i}^2 \right) \right]^{\frac{1}{2}} \quad (A.14)$$

$$\sigma \left(\frac{\overline{EW}_{Fe}}{\overline{EW}_{CN}} \right) = \frac{1}{80\overline{EW}_{CN}} \left[\left(\sum_{i=1}^4 EW_{Fe_i}^2 \right) + \frac{\overline{EW}_{Fe}^2}{\overline{EW}_{CN}^2} \left(\sum_{i=1}^4 EW_{CN_i}^2 \right) \right]^{\frac{1}{2}} \quad (A.15)$$

$$\sigma \left(\frac{\overline{EW}_{Fe}}{\overline{EW}_{Ti}} \right) = \frac{1}{80\overline{EW}_{Ti}} \left[16\overline{EW}_{Fe}^2 + \left(\sum_{i=1}^4 EW_{Fe_i}^2 \right) \right]^{\frac{1}{2}} \quad (A.16)$$

B. About the stars used in this work

B.1. Classification and basic quantities

Below is shown a table displaying all the stars used throughout the dissertation, with their Henry-Draper Catalogue identifier, stellar class, distance, $B - V$ index, absolute visual magnitude and wavelength shift $\Delta\lambda$. Their evolutionary status (RC, RGB or AGB) is also shown and the column "Reference" refers to the scientific paper from which the evolutionary status was obtained (note that the evolutionary status of only 4 stars could not be found).

Group	#	HD Identifier	Class	D [pc]	B-V [mag]	Mv [mag]	$\Delta\lambda$ [Å]	Reference
RC	1	140573	K2 IIIb CN1	22.7	1.167	1.02	0.101	[24]
	2	169916	K1 IIIb	24.0	1.025	1.09	-1.069	[24]
	3	85503	K2 III	38.1	1.230	0.83	-0.007	[24]
	4	110458	K0 III	58.4	1.075	0.99	-0.205	[24]
	5	83240	K1 III	75.3	1.051	0.79	0.524	[24]
	6	99322	K0 III	84.0	0.979	0.75	0.185	[24]
	7	45415	G9 III	94.4	1.035	0.84	1.320	[24]
	8	121416	K1 III	97.6	1.140	1.04	0.011	[26]
	9	11643	K1 II	111.1	1.120	0.86	0.618	[24]
Unknown	10	95405	K0 III CN	254.6	1.180	1.30	0.253	
	11	202320	K0II/III	223.9	1.165	-1.60	-0.098	
	12	148291	K0II/III	288.4	1.235	-2.12	0.204	
	13	95689	K0 III	37.7	1.070	-1.10	-0.006	
RGB	14	124897	K1.5 III	11.3	1.230	-0.31	-0.108	[28]
	15	29139	K5 III	20.4	1.540	-0.69	1.360	[28]
	16	107446	K3.5III	70.5	1.420	-0.65	-0.101	[27]
	17	152786	K3III	149.0	1.625	-2.79	-0.139	[27]
	18	138688	K4III	137.7	1.299	-0.56	0.559	[29]
	19	145206	K4III	117.9	1.439	0.02	-1.290	[30]
	20	167818	K5III	233.6	1.638	-2.22	-0.362	[27]
	21	206778	K2Ib	211.4	1.520	-4.24	0.118	[27]
	22	225212	K3Iab	641.0	1.617	-4.11	-1.042	[27]
	23	198357	K3III	166.6	1.389	-0.61	0.489	[27]
	24	199642	K5/M0III	250.9	1.580	-0.74	0.529	[27]
	25	12642	K5Iab	158.9	1.549	-0.40	0.647	[27]
	26	119090	K6II	430.1	1.440	-2.12	0.804	[27]
	27	149447	K6III	105.0	1.574	-0.95	-0.002	[27]
	28	89736	K7III	809.8	1.679	-3.93	0.511	[27]
	29	12929	K1 IIIb	20.2	1.150	0.47	-0.006	[21]
	30	107328	K0 IIIb	103.4	1.160	0.26	0.004	[30]
AGB	31	220009	K2 III	110.0	1.204	-0.56	0.001	[31]

Figure 76: Table with the $B - V$ color index, distance, absolute visual magnitude, wavelength shift, stellar class and evolutionary status of the studied stars. All the data were obtained from [21], [24], [25], [26], [27], [28], [29], [30] and [31].

B.2. Additional quantities

Below is shown a table displaying the metallicities, masses and surface gravities of the stars of this dissertation, which were used in section 7. Once again, the column "References" refers to the scientific papers from which the data were obtained.

Group	#	HD Identifier	M [M _⊕]	log(g) [dex]	[Fe/H] [dex]	References
RC	1	140573	1.66	2.72	0.189	[32]
	2	169916	2.6	2.53	-0.11	[33]
	3	85503	1.5	2.5	0.17	[34], [35]
	4	110458	1.71	2.61	0.19	[36], [37]
	5	83240		2.52	0.03	[37]
	6	99322		2.88	0.11	[37]
	7	45415	2.2	2.48	0.05	[37]
	8	121416				
	9	11643		2.35	0.14	[37]
Unknown	10	95405			0.01	[38]
	11	202320	2.63	1.77	-0.17	[36], [37]
	12	148291		1.64		[34]
	13	95689	3.44	2.2	-0.2	[39]
RGB	14	124897	1.08	1.66	-0.52	[40]
	15	29139	1.16	1.45	-0.33	[41], [42]
	16	107446	1.52	1.26	-0.21	[43]
	17	152786	7.5	1.2	-0.4	[44], [45]
	18	138688		2.16	-0.15	[46]
	19	145206		1.28		[34]
	20	167818	6.3	2	-0.2	[47], [48], [49]
	21	206778	7.07	1.01	-0.04	[50], [48]
	22	225212	9	0.9	0.08	[47], [36]
	23	198357		1.06		[34]
	24	199642				
	25	12642				
	26	119090	2			[36]
	27	149447				
	28	89736				
	29	12929	1.5	2.57	-0.25	[34]
	30	107328	1.62	2.2	-0.33	[36], [43]
AGB	31	220009	1.37	1.81	-0.71	[36]

Figure 77: Table with the mass, surface gravity and metallicity of the studied stars. All the data were obtained from [32], [33], [34], [35], [36], [37], [38], [39], [40], [41], [42], [43], [44], [45], [46], [47], [48], [49] and [50].

